Measurements of the Beam Normal Asymmetry using Polarized Elastic Electron Scattering off Various Spin-0 Nuclei at 1 GeV

A Dissertation Presented

by

Ryan Richards

to

The Graduate School

in Partial Fulfillment of the Requirements

for the Degree of

Doctor of Philosophy

in

Physics

Stony Brook University

December 2021

Stony Brook University

The Graduate School

Ryan Richards

We, the dissertation committee for the above candidate for the
Doctor of Philosophy degree, hereby recommend
acceptance of this dissertation.

Krishna Kumar – Dissertation Advisor
Professor, Department of Physics and Astronomy

Abhay Deshpande – Chairperson of Defense
Professor, Department of Physics and Astronomy

Rosalba Perna - Committee Member
Professor, Department of Physics and Astronomy

Kent Paschke - External Member
Professor,Department of Physics,University of Virginia

This dissertation is accepted by the Graduate School.

Eric Wertheimer
Dean of the Graduate School

Abstract of the Dissertation

Measurements of the Beam Normal Asymmetry using Polarized Elastic Electron Scattering off Various Spin-0 Nuclei at 1 GeV

by

Ryan Richards

Doctor of Philosophy

in

Physics

Stony Brook University

2021

In this first part of this thesis, I report on the 1 GeV beam normal asymmetry measurements (A_T) on various spin-0 nuclei during PREX-II. In a QED framework, this P-even, T-odd observable is a direct probe of the imaginary part of the two-photon exchange amplitude, since time reversal symmetry dictates A_T must vanish in the one-photon approximation. At ultrarelativistic energies, the beam normal asymmetry is sensitive to the hadronic structure of the target nucleus. Calculations of the two-photon exchange amplitude are challenging since one has to consider all intermediate hadronic states in the calculation. The treatment of the states are both model and kinematics dependent. Therefore direct measurements of the beam normal asymmetry can test theory models.

For experiments which measure the parity-violating asymmetry A_{PV}, the beam normal asymmetry can enter as a false asymmetry for A_{PV} when the beam is not 100% longitudinally polarized. For

fixed target experiments, A_{PV}, which is sensitive to the ratio of weak neutral current amplitude and electromagnetic amplitude is on the order of $10^{-7} - 10^{-4}$. Under the same experimental conditions A_T is on the order $10^{-6} - 10^{-4}$, often bigger than A_{PV}. Therefore, we must correct for a nonzero A_T to extract an accurate A_{PV}. In the second part of the thesis, I address how we make the A_T corrections.

Finally in the third part of this thesis, I addresses the PREX-II acceptance function, which represents the probability as a function of kinematic parameters that an electron that reached the detector, scattered from ^{208}Pb. The acceptance function is critical input not only to interpret A_{PV} measurement, but also to accurate evaluate A_T corrections.

Contents

List of Figures

Chapter 1

Introduction

1.1 Elastic Electron Scattering

1.1.1 Elastic Electron Scattering through Photon Exchange

Protons and neutrons are the building blocks of atomic nuclei. The internal structure of the nucleons determine their fundamental properties which directly affects the properties of nuclei. Understanding how the nucleus is built in terms of its constituents, quarks and gluons, remain both an important and challenging question in nuclear physics. One of the first nuclear properties was discovered by Rutherford: that the size of the nucleus is on the order of a few femtometers. With a wide range of nuclei with different mass numbers A(sum of protons Z and neutrons N), one can use electron scattering to probe novel properties of the nucleus such as the nuclear charge distribution ρ_p of protons.

The nuclear charge distributions are measured by electron scattering through electromagnetic probes (one-photon exchange). The underlying theory is described by Quantum Electrodynamics (QED) which describes how light interacts with charged particles. Measuring nuclear charge distributions using elastic electron scattering off nuclei was a technique mastered by Hofstadter in 1950s. In elastic electron scattering, the final state nucleus remains the same, but with finite recoil. Electron scattering can be represented pictorially using a Feynman diagram. The incident and outgoing electrons have 4-momenta k

= (E,$\boldsymbol{k}$) and k' = (E',$\boldsymbol{k'}$). The incident and final state nucleus 4-momenta are P and P' respectively. The 4-momentum of the exchanged photon is

$$q = k - k' = P - P'. \tag{1.1}$$

The lowest order Feynman diagram corresponding the electron scattering is shown in Figure 1.1.

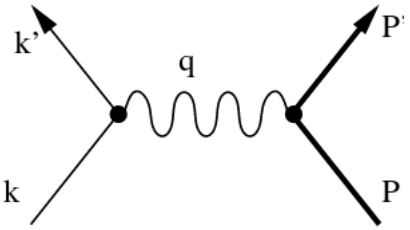

Figure 1.1: Lowest order Feynman diagram for elastic electron scattering off nucleus

For a fixed target experiment, one can measure the scattered electron's scattering angle θ momentum E' such that the 4-momentum of the photon is fixed. The Lorentz invariant of the photon is $q^2 = -4EE' \sin^2\theta$ which is negative. From the uncertainty principle, the virtual photon's wavelength is inversely proportional to q. This means that the scattering can be thought of as point-like scattering off a Coulomb potential. The distribution of the scattered electrons defines the cross-section, which is the probability of interaction between the electron and nucleus.

The cross-section depends on the kinematics, which of course fixes the Q^2. Calculating the cross section involves calculating the amplitude since the cross section $d\sigma$ is given by [1]

$$d\sigma = \frac{\mathcal{M}^2}{F} dQ, \tag{1.2}$$

where F is the incident flux, dQ is the integration factor which enforces energy conservation, and $\mathcal{M}$ is the invariant amplitude. The invariant amplitude $\mathcal{M}$ for electron-nucleus scattering is given pictorally by Figure 1.1. All scattering processes amount to calculating $\mathcal{M}$.

In QED, the incoming and outgoing electrons are described by four component Dirac spinors (spin up and spin down)

$$u(k)e^{ikx}. \tag{1.3}$$

For the photon-electron vertex, the interaction is given by $-ie\gamma^\mu$ where γ^μ is the Dirac matrix which satisfies the following anticommutation relation $\{\gamma^\mu, \gamma^\nu\} = 2\eta^{\mu\nu}$. Using the Feynman rules for QED, the overlap between the initial and final state electrons is expressed by

$$-ie[\bar{u}(k')\gamma^\mu u(k)]. \tag{1.4}$$

so that scattering off a point-like nucleus of charge Ze, the amplitude is given by

$$\mathcal{M} = Ze^2[\bar{u}(k')\gamma^\mu u(k)]\frac{g^{\mu\nu}}{q^2}[\bar{u}(p)\gamma^\nu u(p')] \tag{1.5}$$

where $\frac{g^{\mu\nu}}{q^2}$ is the photon propagator. For relativistic electron energies, equation 1.5 can be can evaluated explicitly [2] leading to the differential Mott cross section,

$$(\frac{d\sigma}{d\Omega})_{Mott} = \frac{Z^2\alpha^2}{4E^2\sin^4\theta}\cos^2\theta, \quad \alpha = \frac{e^2}{4\pi\epsilon_o}. \tag{1.6}$$

Equation 1.6 is only valid if the nucleus was point-like and spinless. For an extended object, the Mott cross section is modified by introducing a form factor which accounts for the phase differences between different contributions to the scattered wave from different points in the charge distribution which can be derived within the first Born approximation using plane waves [2]. The scattering amplitude $\mathcal{M}$ is given by the matrix element $< \psi_f|V(r)|\psi_i >$ with

$$V(\boldsymbol{r}) = Ze\int \frac{\rho(\boldsymbol{r'})}{4\pi|\boldsymbol{r} - \boldsymbol{r'}|}d^3\boldsymbol{r'}. \tag{1.7}$$

and $\psi_{i,f}$ are the initial and final state wavefunctions. Within this framework, the scattering amplitude can be separated into a point-like amplitude modified by an extended object

$$\mathcal{M} = \mathcal{M}^{pt}\int \rho(\boldsymbol{r'})e^{iq\cdot r'}d^3r' = \mathcal{M}^{pt}F(q). \tag{1.8}$$

The integral in equation 1.8 defines the form factor as the Fourier transform of the charge distribution so that the differential cross section is given by

$$\frac{d\sigma}{d\Omega} = \frac{d\sigma}{d\Omega}_{Mott}|F(q^2)|^2. \tag{1.9}$$

One can also note that since the wavelength goes as 1/q, if the wavelength

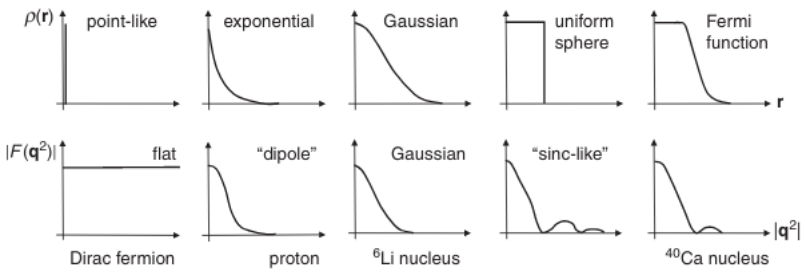

Figure 1.2: Three dimensional charge distributions and their corresponding form factors. Figure from [2]

is larger that the size of the charge distribution, r, F(0) is equal to one. This means that the scattering is point-like. In the opposite limit, the elastic cross section tends to 0. That's because in the large q limit, the virtual photon's wavelength is short enough to resolve the internal structure of the nucleus. This is the deep inelastic regime. The exact form factor depends on the details of the charge distribution. Typical charge distributions and form factors are shown in Figure 1.2.

1.1.2 Elastic Electron Scattering through Z^o Exchange

In addition to elastic scattering through electromagnetic interactions, the electrons and nucleus can interact via the weak force. The weak force is responsible for the radioactive decay of subatomic particles by changing quark flavor. It was initially proposed by Enrico Fermi to explain β decay, in which a neutron in the nucleus decays into a proton, emitting an electron-neutrino pair. Motivated by QED, Fermi treated the interaction as a contact interaction with no mediating particle. Just as in QED, the weak force was believed to obey the parity or spatial inversion symmetry where (x,y,z)→(-x,-y,-z). It wasn't until 1956 that the parity-violation in weak interactions was proposed a solution to the $\tau^+ - \Theta^+$ puzzle. The $\tau^+ - \Theta^+$ puzzle was a paradox where identical particles of the same mass and decay lifetime, which we now know are positively charged kaons, decayed into two decay modes, the τ^+ mode and Θ^+ mode. The τ^+ mode decayed into two pions while Θ^+ mode decayed into three pions. Yang and Lee remedied this paradox by proposing that parity was violated. Yang and Lee proposed that the particles were indeed the same but underwent decay modes where parity wasn't conserved [1, 3]. It was in 1956 that parity-violation in weak interactions was experimentally confirmed in Wu et. al's cobalt-60 experiment.

Studies beyond the evidence of Wu describe the weak force being mediated by massive charged $W^{\pm}$ ($M_W = 80.397 \pm 0.012$ GeV/c) bosons and an uncharged Z^o boson ($M_{Z^o} = 91.1876 \pm 0.0021$ GeV). The weak force is weaker ($G_F \sim 10^-5$) than the electromagnetic (coupling $\alpha = 1/137$) but occurs between all particles [1]. The weak and electromagnetic interactions are unified through the electroweak interaction where the weak Z boson and photon arise through a mixing of the interactions through θ_W, the weak mixing angle, which has been measured as $\sin^2\theta_W \approx 0.23$[1]. Interactions via Z^o exchange between the electron and the nucleus can be represented as a Feynman diagram similar to Figure 1.1 by replacing γ with Z^o. However, the weak interaction between the electron and proton interaction is suppressed relative to the same interaction between the electron and neutron. That's because the weak charge of the neutron ($Q_{W,n}$ = -1) is larger than the weak charge of the proton ($Q_{W,p}$ = 1-$\sin^2\theta_W \approx 0.076$). This fact makes accessing neutron information through weak probes an interesting option.

Following the similar prescription in the electromagnetic case, one can define an equivalent weak form factor in the same formalism with the appropriate modifications. Before going through the steps, one must first define the concept of helicity. The helicity of a particle refers to its spin projection onto its momentum direction i.e.,

$$H = \frac{\boldsymbol{S} \cdot \hat{p}}{|S||p|} \tag{1.10}$$

for a particle of spin S . If the spin of the particle is aligned along its momentum direction,the particle is said to have positive helicity. If the spin and momentum are anti-aligned, the particle has negative helicity. Generally speaking, the helicity of a particle is not an instrinsic property since one can always move to a frame where the helicity changes. However, for massless particles or relativistic particles, this is an instrinsic property and can be associated with chirality or handedness. In this limit, particles with positive helicity are right-handed while negative helicity particles are left-handed.

As mentioned previously, chirality is associated with the handedness of the particle. In more abstract terms, chirality refers to how a particle (expressed as spinor) transforms under the left/right chiral projection operator defined as

$$P_L = \frac{1}{2}(1 - \gamma^5), \quad P_R = \frac{1}{2}(1 + \gamma^5), \tag{1.11}$$

where the chiral operator γ^5 is given by $\gamma^0\gamma^1\gamma^2\gamma^3$ [1]. While charged W bosons

[1] $\sin^2\theta_W = 1 - (\frac{M_W}{M_{Z^o}})^2$

only couple to left handed particles, the Z^o boson couple to both left-and right-handed particles with different strengths. For left-handed fermions, the couplings $c_L = T_3 - q_f \sin^2\theta_W$, and for right $c_R = -q_f \sin^2\theta_W$. Here q_f is electric charge and T_3 is third component of the weak isospin. For left-handed electrons T_3 is -1/2 while for right-handed electrons it's zero [2]. As done for the electromagnetic case (equations 1.4,1.5), the weak neutral current amplitude is given by

$$j^\mu = \bar{u}(k')[-ig\gamma^\mu \frac{1}{2}(c_v - \gamma^5 c_A)]u(k) \tag{1.12}$$

with $c_v = c_L + c_R$ and $c_A = c_L - c_R$. The interaction vertex consists of a vector like interaction and helicity dependent axial interaction(γ^5). The neutral current amplitude is

$$\mathcal{M}_\mathcal{W} = \frac{G_F}{2} j_N^\mu \frac{g^{\mu\nu}}{q^2 + M_Z^2} j_e^\nu. \tag{1.13}$$

The middle expression is the Z^o propagator[2] and j_N^μ is the weak current for the nucleus.

We can also compute the scattering amplitude in the first-Born approximation with potential

$$V_\pm(r) = V_C(r) \pm \gamma^5 A(r) \tag{1.14}$$

where the $\pm$ accounts for the scattering potential seen by the differential helicity states. As done in the electromagnetic case, we can define a weak form factor F_W (like equation 1.8) by introducing an analogous weak charge density ρ_W normalized to 1 as

$$Q_W = \int (1 - 4\sin^2\theta_W) Z\rho_p(r') - N\rho_N(r') d^3r'. \tag{1.15}$$

From Equation 1.16, measurements of the weak form factor gives access to neutron density information.

1.2 Parity-Violating Electron Scattering

Starting from Equation 1.15, elastic electron scattering through Z^o exchange with the nucleus can give access to neutron density information. Our existing

[2]In general, the propagator for a massive particle X goes as $\frac{1}{q^2+M_X^2}$

knowledge came from using hadronic probes in experiments such as elastic electron-proton scattering [4–6], pion photon production [7] and anti-proton scattering [8, 9]. At low Q^2, the interpretation of these measurements suffer from theoretical uncertainties from strong interactions. That is because in theory of strong interactions, the coupling constant is large where perturbation theory is not valid and a model dependent interpretation is needed. By using parity violation electron scattering (PVES), one can access the neutron information in a model-independent way. Two experiments PREX-II and CREX measured the parity-violating asymmetry using the electroweak interaction to extract the neutron distribution at low Q^2.

To extract the neutron information involves measuring an observable that isolates the weak amplitude which is suppressed relative to the photon amplitude. This can be done by measuring the parity-violating asymmetry A_{PV} using longitudinally polarized electrons. A_{PV} is defined as the fractional difference in cross sections

$$A_{PV} = \frac{\frac{d\sigma_+}{d\Omega} - \frac{d\sigma_-}{d\Omega}}{\frac{d\sigma_+}{d\Omega} + \frac{d\sigma_-}{d\Omega}} = \frac{|\mathcal{M}_+|^2 - |\mathcal{M}_-|^2}{|\mathcal{M}_+|^2 + |\mathcal{M}_-|^2}, \quad M_\pm = M_\gamma \pm M_{Z,\pm}. \tag{1.16}$$

which reduces to

$$A_{PV} = \frac{M_+ - M_-}{M_\gamma} \approx \frac{Q^2}{\alpha M_Z^2}. \tag{1.17}$$

in the low Q^2 limit and scales as the ratio of propagators. For fixed target experiments such as PREX-II/CREX, $A_{PV} \sim 10^{-7} - 10^{-6}$. In terms of the form factors(see equations 1.8 and 1.17), A_{PV} in the Born approximation is

$$A_{PV} \approx \frac{Q^2}{4\pi\alpha\sqrt{2}M_Z^2} \frac{F_n(Q^2)}{F_p(Q^2)}. \tag{1.18}$$

Parity-violating asymmetry is schematically shown in Figure 1.3. A longitudinally polarized beam is incident on an unpolarized target. Figure 1.3, shows the interaction in the COM off a proton target. The only changing parameter is the sign of the longitudinal polarization. We measure the fractional difference between two states.

Parity-violating electron scattering has become a precision tool over the years since the first experiment of its type, E122 in 1978. A broad program of experiments use PVES as method of studying nuclear structure and studying for physics beyond the Standard Model highlighting the interplay between

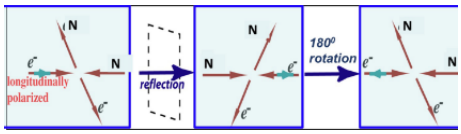

Figure 1.3: Parity Violating Experiment. Figure from [10]

probing hadron structure and electroweak physics. Figure 1.4 shows the precision of such experiments where the x-axis is the predicted asymmetry A_{PV} while the uncertainty on A_{PV} is on the y-axis. Two such experiments as mentioned are PREX-II and CREX, which measure the A_{PV} off ^{208}Pb and ^{48}Ca nuclei respectively. Achieving such precision, however, requires very good control over systematic errors. One of which is the is the beam normal asymmetry or transverse asymmetry which arises due to residual transverse polarization. The beam normal asymmetry is the subject of this thesis.

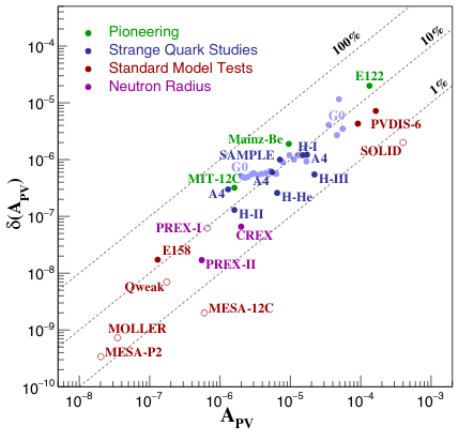

Figure 1.4: History of precision parity-violating electron scattering experiments. Figure from [3]

1.3 Introduction to the Vector Analyzing Power

A transverse component of the beam polarization couples to what is known as the vector analyzing power A_n. When scattering from nuclei using transversely polarized electrons, the scattering amplitude develops an azimuthal dependence due to the interaction between the electron's spin with the effective magnetic field produced by the target nucleus in the electron's rest frame. The azimuthal dependence is quantified by measuring the beam nor-

mal asymmetry A_T, defined as the fractional difference in scattering cross sections between transversely polarized electrons parallel and anti-parallel to the normal scattering plane:

$$A_T \equiv \frac{d\sigma_\uparrow - d\sigma_\downarrow}{d\sigma_\uparrow + d\sigma_\downarrow} = A_n \boldsymbol{S_e} \cdot \frac{\boldsymbol{k_e} \times \boldsymbol{k'_e}}{|\boldsymbol{k_e} \times \boldsymbol{k'_e}|}. \tag{1.19}$$

The physics of A_n is described by quantum electrodynamics (QED). Under symmetry considerations, A_T is parity-conserving but T-odd. Under time reversal, the amplitude picks up a phase but also becomes complex conjugated. As a result, A_n vanishes in the 1γ exchange approximation and is a direct probes of 2γ exchange amplitudes[3]. Because of the complex conjugation of the amplitude, the vector analyzing power is sensitive to the imaginary part of the 2γ exchange amplitude (see Figure 1.5). The analyzing power is sensitive to the interference between the 1 and 2γ exchange amplitudes as

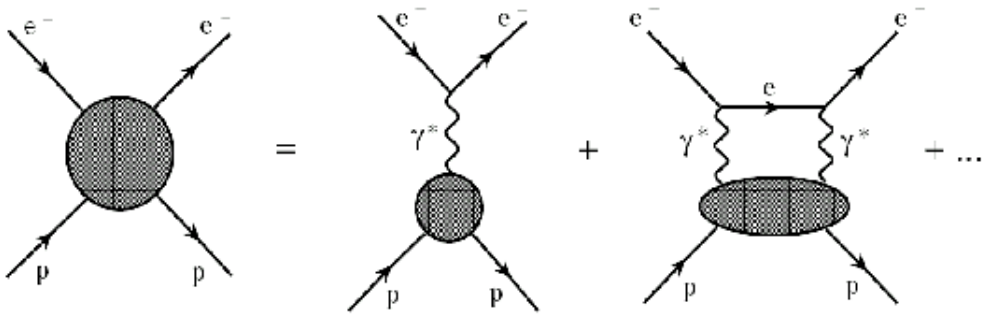

Figure 1.5: Feynman Diagrams for A_T. The Figure from [11].

$$A_n = \frac{M_\gamma \operatorname{Im} M_{\gamma\gamma}}{|M_\gamma|^2}. \tag{1.20}$$

The leading order contribution to order α is given by Equation 1.20. In addition, the size of the analyzing power depends on both the nuclear charge Z and is Lorentz suppressed due to the fact that relativistic electrons are polarized transverse to the scattering plane. This means that A_n scales naively as $Z\alpha\frac{m}{E}$ where E is the beam energy. For fixed target experiments, this observable is on the order of $\sim 10^{-6} - 10^{-5}$ thus making it comparable to or larger

[3]The 1γ exchange amplitude is purely real and doesn't have an imaginary part

that A_{PV}. Therefore direct A_T measurements are important to quantify to size of the asymmetry as it is a potential systematic error to parity-violating asymmetry measurements.

1.3.1 Experimental Motivations

1.3.1.1 Experimental Evidence for Two Photon Exchange

Unlike the analyzing power which deals with the imaginary part of 2γ exchange, the first experimental evidence was sensitive to the real part. In 2000, the first measurement of the proton's electric to magnetic form factor (G_E/G_M) using the polarization transfer technique [12] deviated from the measurements using Rosenbluth separation at Q^2 above $(1GeV/c)^2$ (see Figure 1.6)[13, 14].

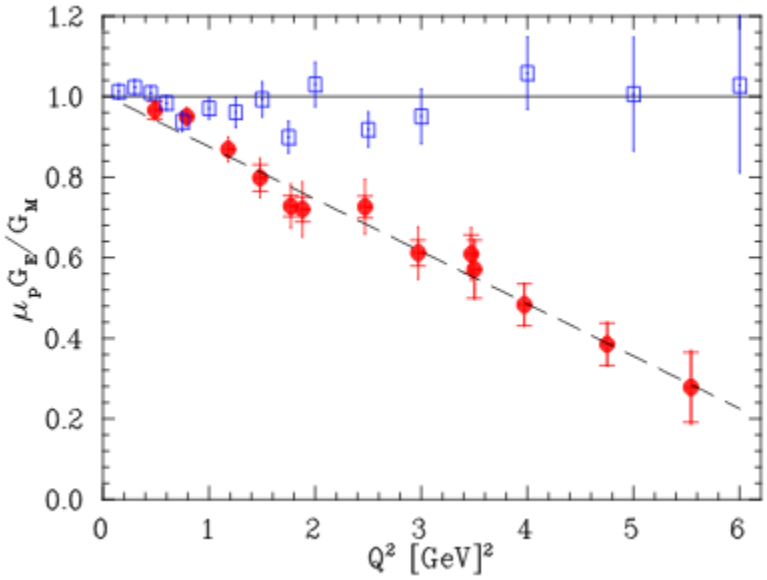

Figure 1.6: Measurements of the electric to magnetic form factor ratio on the proton. The Rosenbluth measurements are given by the hollow blue squares while the polarization measurements are given by the solid red circles. Figure from [14]

Within the Born approximation, the Rosenbluth cross section is measured as a function of the photon polarization ϵ at fixed Q^2 as

$$d\sigma_B = \frac{\epsilon}{\tau}G_E^2 + G_M^2, \quad \tau = \frac{Q^2}{M_p^2}, \quad \epsilon = 1 + 2(1+\tau)\tan^2(\theta/2)$$

while the polarization measurements extract the ratio by taking the ratio of the transverse and longitudinal polarization of recoiling proton via[4]

$$\frac{P_t}{P_l} = -\sqrt{\frac{2\epsilon}{\tau(1+\epsilon)}}\frac{G_E}{G_M}.$$

This discrepancy between the two techniques have forced physicists to go beyond the Born approximation into the world of two photon exchange physics. Normally, within the Born approximation, diagrams including more than one photon are treated as radiative corrections developed by Mo and Tsai [15]. Within this scheme, corrections to the cross section account for particles exchanging a second virtual photon (self-energy,vertex-energy and two-photon exchange) and for real photon emission (Bremsstrahlung). The dominant correction is the virtual photon correction which can be as large as 30% of the uncorrected cross section [16].

The problem with the Mo and Tsai treatment of radiative corrections is that it ignores the effect of hadron structure from the second exchanged photon i.e., the photon emission is soft. Figure 1.7 shows the difference between the two-photon exchange (real part) correction within the hard photon limit and the soft-photon limit.

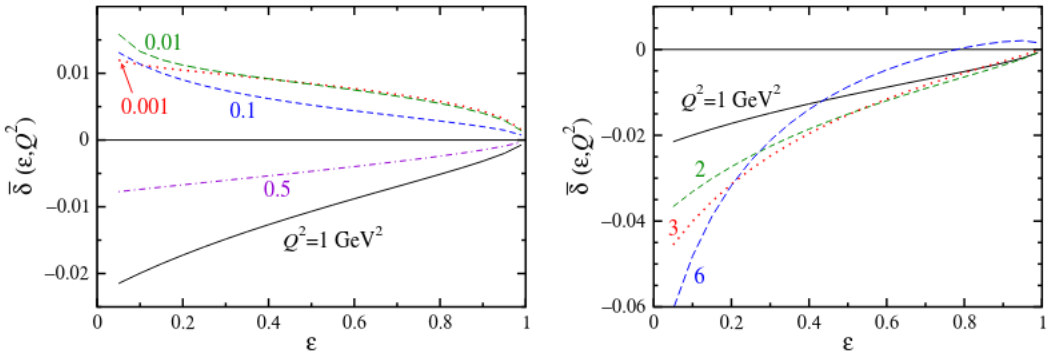

Figure 1.7: Difference between the size of the radiative corrections calculated using different treatment of the two-exchange exchange. The calculations involving two-photon exchange not neglecting hadron structure was done by Blunden et. al. The figure shows the ϵ dependence of the difference for fixed Q^2. The disagreement by as much as 6%. The differences are largest for backward angle scattering. The figure is from [17]

To resolve the Rosenbluth discrepancy involves a correction linear in ϵ that decreased in the backward angle limit. The correction, sensitive to real part of

[4]The limit where $\epsilon \to 0$ is backward angle scattering.

the two-photon exchange amplitude has been shown to have this dependence [17, 19, 20] is given by

$$\delta_{\gamma\gamma} = \frac{2\,\mathrm{Re}(M_\gamma M_{\gamma\gamma})}{|M_\gamma|^2} \tag{1.21}$$

The Rosenbluth data was corrected for the two-photon exchange since the Rosenbluth cross section not measured as a ratio as in the polarization technique and seems to be in good agreement with the polarization transfer measurements (see Figure 1.8). However, the two-photon calculations are not complete and haven't been tested over a large kinematic range. Even though the discrepancy has been resolved at high Q^2, two-photon exchange described within the hard-photon exchange treatment hasn't been investigated at low Q^2.

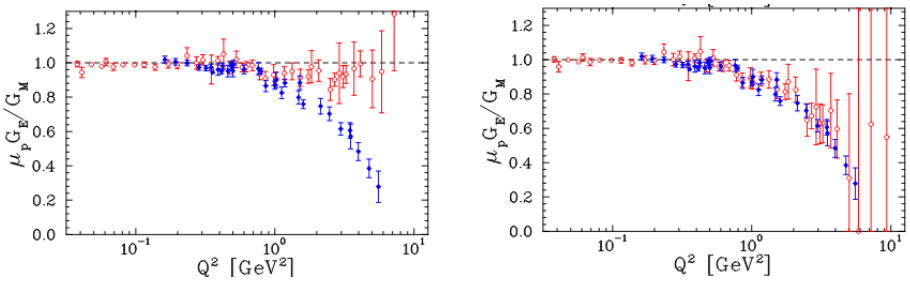

(a) Form factor ratio without $\delta_{\gamma\gamma}$ (b) Form factor ratio with $\delta_{\gamma\gamma}$

Figure 1.8: The proton electric to magnetic form factor ratio as a function of Q^2. The two-photon exchange correction brings the Rosenbluth measurements (red circles) closer to the polarization transfer (blue diamonds) measurements. The uncertainties in the two-photon exchange correction is determined by how the correction is known at large Q^2 and the measurement's extraction. The figures and analysis is found in [20].

1.3.1.2 Experimental Inputs of Two-Photon Exchange

To properly benchmark theoretical models of two-photon exchange requires measuring observables that provide direct access to the two-photon exchange process one of which includes the vector analyzing power, the subject of this thesis.

The transverse asymmetry belongs to a more general group of observables called single spin asymmetries. When measuring single spin asymmetries one

can also have scattering of an unpolarized beam on a polarized target. In this case, the target is polarized parallel or anti-parallel to the polarization vector and is also known as the target spin asymmetry. Compared to their counterparts i.e., the transverse asymmetry, theory has predicted target spin asymmetries to be larger ($\sim 10^{-3}$) than the transverse asymmetry at similar kinematics [21]. However, there has been only one reported measurement of a target spin asymmetry [22].

In addition to the single spin asymmetries, the real part of the two-photon exchange amplitude is accessible through cross section measurements involving positrons. Under charge conjugation, the electron-photon vertex in equation 1.4 undergoes a sign change. That way by measuring the ratio of the positron-proton and electron-proton cross section is given by

$$\frac{\sigma^{e+p}}{\sigma^{e-p}} = 1 - 2[\delta_{\gamma\gamma} - \delta_{MT}] \tag{1.22}$$

where $\delta_{\gamma\gamma}$ is given by equation 1.21 and δ_{MT} is the Mo-Tsai treatment of two-photon exchange. This observable is a direct measure of the hadronic structure dependent correction to form factor measurements. Initial measurements of the ratio provided experimental constraints on the two-photon exchange to the Rosenbluth separation technique. The data showed that the two-photon exchange correction was then a 1% for Q^2 between 0.01 GeV^{-2} and 5 GeV^{-2} [23–26]. This is shown in Figure 1.9(a).

The data was reexamined once the form factor measurement discrepancy was found. A reanalysis of the data without the low-precision high Q^2 data shows an ϵ dependence of the ratio $\frac{\sigma^{e+p}}{\sigma^{e-p}}$ which gives a 3% ϵ dependence on the electron-proton data for low Q^2 (Figure 1.9b) [23]. However, since the average Q^2 of the data is 0.5 GeV^{-2}, one cannot make a full correction to explain the Rosenbluth discrepancy at Q^2 larger than 2 GeV^{-2}. One percent precision measurements of $\frac{\sigma^{e+p}}{\sigma^{e-p}}$ were proposed at Jefferson Lab [27] and by the OLYMPUS collaboration [28].

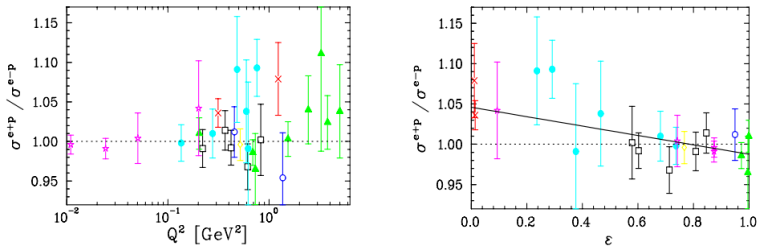

(a) $\frac{\sigma^{e+p}}{\sigma^{e-p}}$ vs Q^2 (b) $\frac{\sigma^{e+p}}{\sigma^{e-p}}$ vs ϵ, $Q^2 < 2\ GeV^{-2}$

Figure 1.9: Measurements of the ratio of positron-proton to electron-proton cross section. (a) Measurements vs Q^2. The different colors indicate different measurements. The data was fit was a constant (dashed line). The fact the constant is roughly about 1 indicates a very correction implies a weak ϵ dependent correction (b) The ϵ dependence of the ratio from later analysis. The low Q^2 data shows the ϵ dependence. The slope of the fit is on the order of 6%. The figures are from [29]

1.3.2 Theoretical Modeling

As discussed in section 3.1, the physics of the analyzing power is sensitive to the imaginary part of the two-photon exchange amplitude. One can write the amplitude M_T for electrons scattering off a spin 0 nucleus as [31]

$$M_T = \frac{e^2}{Q^2}\bar{u}(k')m_e A_1 + A_2\gamma_\mu P^\mu u(k) \tag{1.23}$$

where the amplitudes A_1 and A_2 are the helicity-flip and non-flip amplitudes respectively. In the 1γ approximation, A_1 vanishes and consists of the sum of the 1γ and 2γ exchange amplitudes. The non-flip amplitude A_2 is related to the form factor as $A_2 = 2ZF_N(Q^2)$. The vector analyzing power defined by Equation 1.23 is given by

$$A_n = \frac{m_e}{\sqrt{s}}\tan(\frac{\theta_{CM}}{2})\frac{\mathrm{Im}\, A_1}{ZF_N(Q^2)} \tag{1.24}$$

with $\sqrt{s}$ being the center of mass energy. Since the amplitude A_1 consists of the sum of 1 and 2γ exchange, the imaginary part of A_1 consists of only the imaginary part of $M_{\gamma\gamma}$.

The imaginary part of the two-photon exchange amplitude is modeled by treating the interaction as Doubly Virtual Compton Scattering (VVCS) [32].

In this case, the two photon exchange is treated as Compton scattering off the nucleus with two virtual photons within using the hard photon treatment (see Figure 1.10). Using the formalism described in [32], the imaginary part of the $M_{\gamma\gamma}$ can be expressed as integral over the intermediate electron states

$$\mathrm{Im}\, M_{\gamma\gamma} = e^4 \int \frac{|\boldsymbol{k_1}|^2 d|\boldsymbol{k_1}| d\Omega_{k1}}{2E_{k1}(2\pi)^3} u(\bar{k'})\gamma_\mu(\gamma \cdot k_1 + m_e)\gamma_\nu(k)\frac{1}{Q_1^2 Q_2^2} W_{\mu\nu}(w, Q_1^2, Q_2^2) \tag{1.25}$$

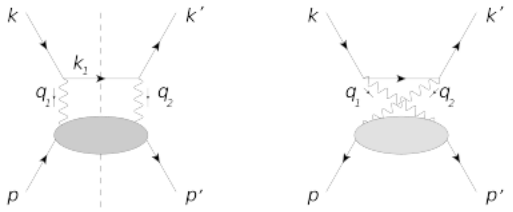

Figure 1.10: Compton-like Feynman diagrams for the two-photon exchange process. The blob represents all the intermediate states both elastic (ground) and inelastic (excited) states of the nucleus. k_1 is the momentum of the intermediate state electrons and $q_1 = k - k_1$ and $q_2 = k_1 - k'$ are the four-momentum carried by the virtual photon. Figure from [12].

where k_1 is the four-momentum of the intermediate state electron, $d\Omega_{k1}$ is the solid angle, $W_{\mu\nu}$ is the hadronic tensor and w is the invariant mass of the intermediate hadronic state. Theoretical predictions of the analyzing power are challenging due to the fact that one must sum over all states kinematically allowed by the virtual photons. In practice, calculations depend on how one calculates $W_{\mu\nu}$ within a kinematic range. The hadronic tensor $W_{\mu\nu}$ is the absorptive part of the VVCS tensor for all possible on-shell intermediate states X.

For the ground state, X = N where N is the nucleon or nucleus. In this case, exact calculations are done using on-shell electromagnetic form factors. However, for the excited states such as X = πN and $\pi\pi$N, theory calculations rely on experimental inputs from Compton scattering. These calculations are both model and kinematics dependent. Model calculations for the proton case are summarized as in Table 1.1 as done in [12] as an example. As evident from Table 1.1, one can have different models for the same kinematics. Therefore the analyzing power suffers from large model dependent uncertainties.

Model	Q^2 or E	Input
Dianescu & Musolf [34]	< 1 GeV	Effective Field Calculation
Pasquini & Vanderhaeghan [21]	< 3 GeV	MAID electroproduction amplitudes
Afanasev & Merenkov [35]	$Q^2 \to 0$, E > 1 GeV	Photoproduction cross scections
Gorcthein [32]	$Q^2 < 0.5$ $(GeV/c)^2$, E = 6-45 GeV	Photoproduction cross sections
Gorchtein & Guichon & Vanderhaeghan [36]	$Q^2 > 1$ GeV^{-2}	Generalized Parton Distributions

Table 1.1: Model calculations of the vector analyzing power

1.3.3 Measuring the Vector Analyzing Power

As evident from Table 1.1, measuring observables that are sensitive to two-photon exchange physics is crucial for benchmarking theoretical models. To measure A_n involves setting the beam polarization transverse to the scattering plane and measuring the fractional difference in cross sections between with spins parallel and anti-parallel normal to the scattering plane (see Figure 1.11). The beam normal asymmetry is then given by [33]

$$A_T = A_n S_e \sin(\phi - \phi_s) \tag{1.26}$$

where ϕ is the azimuthal angle of the scattering plane (defined relative to the horizontal) and ϕ_s is the azimuthal angle of the spin vector. Equation 1.28 contains two contributions from both the vertical and horizontal transverse polarization

$$A_T = A_n(P_V \cos\phi + P_H \sin\phi), \quad P_V = S_e \sin\phi_s, \quad P_H = S_e \cos\phi_s. \tag{1.27}$$

We see that $\phi_s = 0$ corresponds to horizontal polarization while $\phi_s = 90$ is vertically.

A table of existing A_n measurements given at different kinematics on various nuclei are given in Table 1.2. The measurements and their associated model calculations will be discussed in section 1.34.

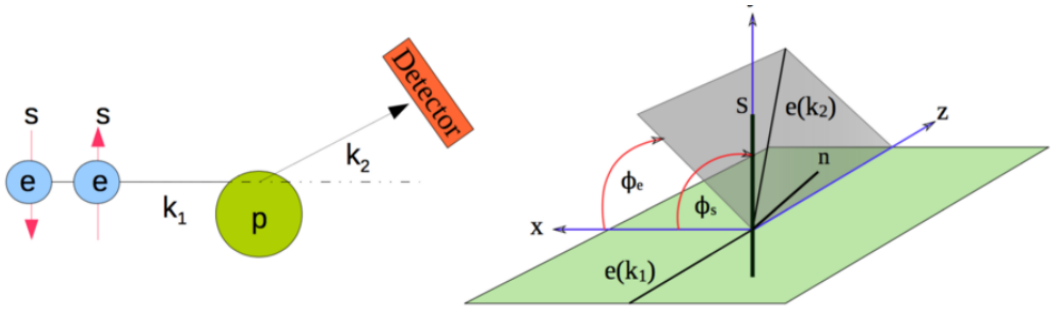

Figure 1.11: A_T schematic, here $\phi = \phi_e$. Figure from [33]

Expt	Tgt	E_b (GeV)	θ_e	Q^2 $(GeV/c)^2$	A_n(ppm)
SAMPLE	^{1}H	0.192	146^o	0.10	-15.4±5.4
A4	^{1}H	0.569	35^o	0.11	-8.59 ±1.16
A4	^{1}H	0.855	35^o	0.23	-8.52 ±2.47
HAPPEX	^{1}H	3.03	6^o	0.009	-6.80 ±1.54
HAPPEX	^{4}He	3.03	6^o	0.077	-13.97 ±1.45
G0	^{1}He	3.03	20.2^o	0.15	-4.06 ±1.17
G0	^{1}He	3.03	25.9^o	0.25	-4.82 ±2.11
G0	^{1}He	0.362	108^o	0.22	-176.5 ±9.4
G0	^{1}H	0.687	108^o	0.63	-21.0 ±24
PREX	^{12}C	1.06	5^o	0.0098	-6.49 ±0.38
PREX	^{208}Pb	1.06	5^o	0.0088	0.28 ±0.25
Qweak	^{1}H	1.06	7.9^o	0.02480	-5.19 ±0.11
Qweak	^{12}C	1.158	7.7^o	0.02437	-10.68 ±1.07
Qweak	^{27}Al	1.158	7.7^o	0.02437	-12.16 ±0.85

Table 1.2: Existing A_n measurements given in units of 10^{-6} (ppm)

1.3.4 Model Calculations

1.3.4.1 Elastic Scattering off the Proton

Table 1.1 provided a list of model calculations for the vector analyzing power at various kinematics. As previously stated, depending on which kinematic regime you are in, there may be more than one calculation. As a result, direct measurements provide useful inputs to these models. The first published calculation came from Afanasev and Merenkov (A&M) [39] at high momentum transfers for a proton target. They related the intermediate states to the proton's form factors ($F_{1,2}$), while the inelastic states were modeled with the proton's structures functions $W_{1,2}$ with an additional Compton form factor dependence. Their model predicted a few ppm negative vector analyzing power. The analyzing power was large at backward angle and were dominated by inelastic states at higher energies. The analyzing power decreases at higher energies decreases due to Lorentz suppression. However, this model failed to predict the first measurement of the analyzing power on the proton was done by the SAMPLE collaboration [38] (see Figure 1.12a).

A different calculation done by Dianescu and Musolf (D&M) [34] was able to reproduce the SAMPLE results within an effective field theory framework (pionic degrees of freedom are integrated out) where they computed the analyzing power up to second order in E/M, where E is the beam energy and M is the proton mass (Figure 1.12b). The kinematics of the SAMPLE experiment are carried out near pion threshold (E = 280 MeV). As a result, model calculations should involve pionic degrees of freedom such as the Afanasev and Merenkov model [39]. However, no model using intermediate pion states has been able to explain the SAMPLE result.

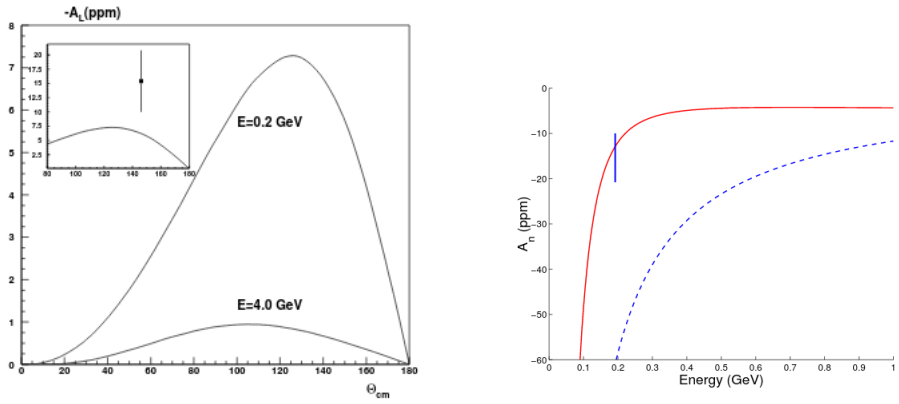

(a) Afanasev and Merenkov (b) Dianescu and Musolf

Figure 1.12: Comparison of the SAMPLE result and model predictions from A&M [39] and D&M [34]. (a) Plots the dependence of A_n as a function of lab scattering angle θ_{cm} at fixed beam energies. The figure considers the only the nucleon intermediate state. (b) A_n vs beam energy for scattering angle 146.1^o. The pionic states are integrated out. The dashed line is the lead order result while the red line is the full calculation. The data point is from the SAMPLE experiment with E = 192 MeV and $\theta_{CM} = 146.1^o$. Figures a is taken from [39] and b is taken from [34]

Additional calculations of A_n were done by Pasquini and Vanderhaeghan (P&V) at energies below 2 GeV [21]. In their model, they use unitarity to relate express the hadronic tensor to pion electroproduction amplitudes from MAID [37], considering the elastic and single pion intermediate states. This model wasn't able to predict the SAMPLE result but was able to partially explain the forward angle A4 measurement and the backward angle G0 and A4 measurements shown in Figure 1.13.

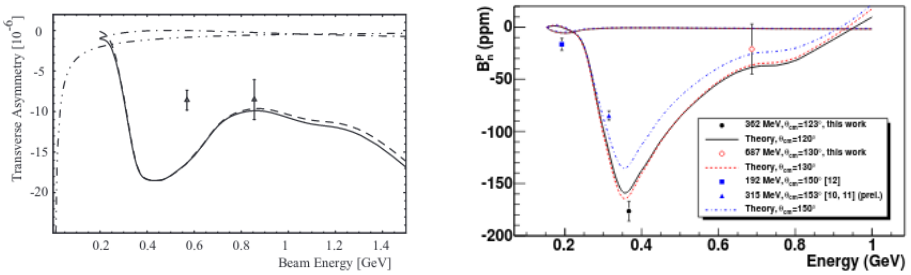

(a) A4 forward angle (b) A_n at backward angles

Figure 1.13: Model predictions compared to the experimental results. (a) A4 forward angle A_n measurements. The dash double dotted line is the D&M calculation. The other lines are from the calculations from P&V. The dotted dashed line is the ground state contribution while the dashed line is the inelastic contribution. The sum of those two lines are shown by the solid line. The P&V model can describe the higher energy data point. At these kinematics, the amplitude is dominated by inelastic states [21]. (b) A_n backward angle measurements. The blue square is from SAMPLE. The black and red circle are from G0 experiment. The blue triangle is from A4. The theory predictions are from P&V and dominated by inelastic states. The lines reflect the different θ_{CM}.

1.3.4.2 Elastic Scattering off A > 1 Nuclei

Theoretical calculations of A_n for complex nuclei (A > 1) are less developed. The first A_n measurements on nuclear targets ^4He, ^{12}C and ^{208}Pb were reported by the HAPPEX/PREX collaborations [40] at very forward angle ($\approx 6^o$) and beam energies of 1-3 GeV. The QWeak collaboration has recently reported on A_n measurements on ^{12}C and ^{27}Al [41].

From the theory side, two different approaches have been applied to extend A_n calculations beyond nucleon scattering. The first approach taken by Cooper and Horowitz addresses Coulomb distortions in the case of scattering from a heavy nucleus of charge Z [30]. Their calculation involves numerically solving the Dirac equation for an electron moving in the Coulomb field of a heavy nucleus to all orders in photon exchange. However, they only consider the ground state of the nucleus while neglecting intermediate excited states. The other approach uses the optical theorem considering only inelastic intermediate states in the integral (equation 1.25). The framework developed by Afanasev and Merenkov [35] in the case of the proton has been extended to complex

nuclei by Howoritz and Gorchtein [31]. Afanasev and Merenkov relate the imaginary part of $M_{\gamma\gamma}$ to the virtual photoabsorption cross section $\sigma_{\gamma^* N}(w, Q^2)$ for nucleon scattering, which in the very forward limit ($Q^2 \to 0$), can be approximated with the real photoabsorption cross section $\sigma_{\gamma N}(w)$. Horowitz and Gorchtein approximate the photoabsorption cross section for nuclei by scaling the real photoabsorption cross section for a single nucleon by the atomic number A. The Q^2 dependence was taken into account by including the charge form factor for the nucleus and assuming the Q^2 dependence of the Compton cross section has the same exponential falloff for nuclei as it is for the proton. The rate of the falloff is given by the Compton slope parameter B, which was taken as 8 GeV^{-2} for all nuclei.

This model lead to simple scaling for the analyzing power at low Q^2 and very forward angle given by

$$A_n = \frac{A}{Z} \hat{A}_n \sqrt{Q^2} \tag{1.28}$$

with $\hat{A}_n$ being a constant. The reported results from the HAPPEX/PREX collaborations show that this model works light nuclei but disagrees for ^{208}Pb (see Figure 1.14a). The disagreement between data and theory led to the belief that Coulomb distortions play a role in heavy nuclei such as lead because of the large Z. Additional measurements at intermediate Z would shine light on this speculation. This is shown in Figure 1.14b. Only recently have theory calculations treated both Coulomb distortions and the integral over the inelastics within the same framework. In Koshchii et. al [42], they numerically solve the Dirac equation, including the contribution from the inelastics in the form of an optical potential. Also in this new model, the A dependence of the Compton slope is made explicit using experimental data.

Dedicated A_n measurements took place during PREX-II (1 GeV) and CREX (2 GeV) highlighted by the first measurement on a intermediate Z nuclei ^{40}Ca during PREX-II. The ^{40}Ca measurement would provide insight on the Z dependence. Additional A_n measurements were done on ^{12}C and ^{208}Pb. CREX measurements on the same targets provide additional insight to the energy dependence. In addition, CREX measured A_n on ^{48}Ca which together with the (CREX) ^{40}Ca measurement gives insight on A/Z dependence.

The analysis of PREX-II measurements are the subject of Chapter 4. In chapter 6, I compare the PREX-II measurements with the Horowitz and Gorchtein model and Koshchii et.al model.

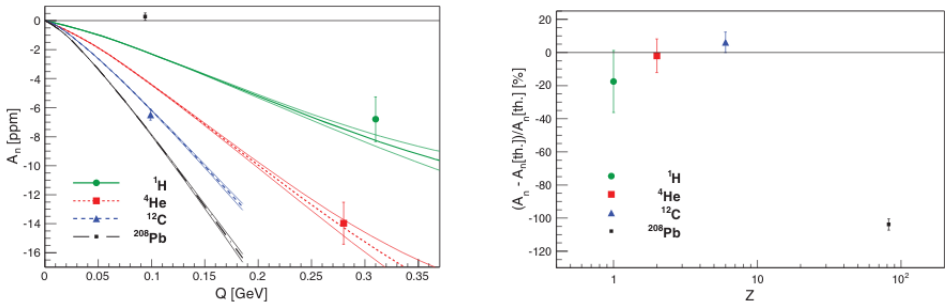

(a) HAPPEX/PREX A_n Measurements (b) Percent Deviation A_n

Figure 1.14: A_n measurements of ^{1}H, ^{4}He, ^{12}C and ^{208}Pb vs theory predictions as a function of Q. (a) shows that light Z nuclei agree with model predictions fairly well but ^{208}Pb doesn't. (b) shows the percent deviation between theory and data normalized to theory as function of Z. The figure implies some Z dependent effect may not be considered in the calculation.

1.3.5 A_n as a false asymmetry to PVES

The analyzing power becomes a false asymmetry in parity violating electron scattering measurements if the electron beam has residual transverse polarization and if the apparatus is not perfectly symmetric in the azimuthal acceptance. This means that the measured asymmetry is given by

$$A_m(\phi) = P_L A_{PV} + P_T A_n \sin(\phi - \phi_S). \tag{1.29}$$

Here P_L and P_T are the longitudinal and transverse beam polarization respectively. If the measured A_n are non-zero, then one must correct for this by adding a systematic correction and/or assigning an uncertainty. As an example, for PREX-II if the ^{208}Pb measurement is consistent with the model prediction (equation 1.30), i.e., A_n = -5 ppm, for a 5% residual transverse beam polarization, the false asymmetry is modulated by

$$A_n P_T = (-5\text{ppm}) \times 0.05 = -0.25\text{ppm}. \tag{1.30}$$

Then equation 1.30 would need to be added to the LHS of equation 1.31 to correct for it. In the case of perfect azimuthal symmetry in the detector plane then this contribution would be zero since the scattering left/right symmetric leading to cancellation. This is shown in equation 1.31

$$\int_0^{2\pi} \sin(\phi - \phi_S) d\phi = 0. \tag{1.31}$$

Realistically, we don't have perfect azimuthal symmetry. In the case were equation 1.31 is non-zero e.g., 0.01, then the false asymmetry is given by the product of equations 1.30 and 1.31

$$A_n P_T \times 0.01 = -0.0025\text{ppm}. \tag{1.32}$$

Equation 1.27 are the A_T contributions needed to correct Equation 1.29 for. Equation 1.29 serves as the starting point of Chapter 5 of this thesis.

Chapter 2

Experimental Overview

PREX-II measured the parity-violating asymmetry in the elastic scattering of longitudinally polarized electrons off a ^{208}Pb nucleus. Its sister experiment CREX also measured the parity-violating asymmetry off a ^{48}Ca nucleus. Both experiments took place at a central angle of about 5^o. The beam energy and current for PREX-II (CREX) were 950 MeV (2.2 GeV) and 70 (150) μA respectively. PREX-II and CREX both took place in Hall A at the Thomas Jefferson National Accelerator Facility (Jefferson Lab). Due to the setup of the experiments, both PREX-II and CREX took dedicated runs to measure the transverse asymmetry using 100% transversely polarized electrons to quantify a potential source of systematic error. The transverse asymmetries were measured on various targets highlighted by the first measurements on intermediate Z nuclei, ^{40}Ca at PREX-II and CREX kinematics and $48Ca$ for CREX. I will report on the 1 GeV measurements in this thesis. This chapter addresses the experimental setup.

2.1 Accelerator

At the heart of both experiments is Jefferson Lab's Continuous Electron Beam Accelerator Facility (CEBAF). Before 2012, CEBAF ran what was the 6 GeV configuration. In the 6 GeV era, the CEBAF accelerator was able to deliver continuous wave (cw) beam up to 200 μA and 6 GeV energy to three experimental halls (A,B and C). Within the last few years, CEBAF has since been upgraded to accommodate the 12 GeV era, highlighted by the building of a

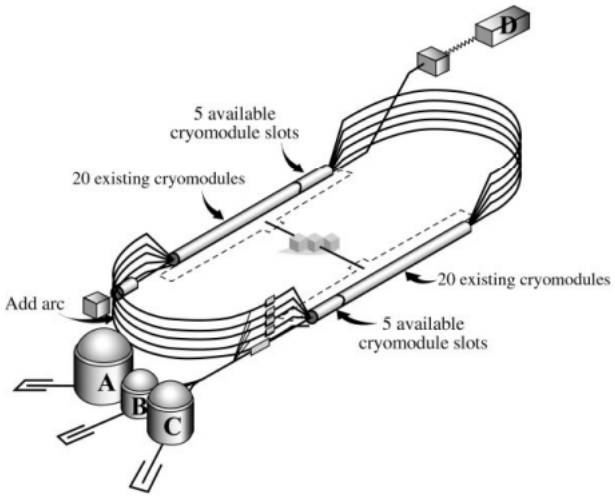

Figure 2.1: CEBAF schematic for 12 GeV upgrade [43]

new experimental hall (Hall D) as shown in Figure 2.1.

The CEBAF accelerator consists of two linear accelerators (linacs) linked by recirculation arcs. The electrons are generated in the injector by illuminating a strained gallium arsenide (GaAs) photocathode with laser light. Once the beam is generated, it is injected in the north linac where it enters recirculating beam lines. As the beam passes through the beam lines, the electrons gain about 1.1 GeV per linac. The beam then gets injected into the south linac where it gains an additional 1.1 GeV in energy. From there, the beam can be sent into the experimental halls (Hall A, B, C) or fed back to the north linac through additional recirculation arcs. The accelerator can provide up to five pass meaning the beam recirculates five times to achieve a total beam energy of 11 GeV.

2.2 Injector at Jefferson Lab

2.2.1 Polarized Source

The electron beam is generated in the injector which consists of a laser table and a GaAs photocathode. By strained, we mean a thin layer ($\sim$ 100 nm) of GaAs is grown on GaAsP(gallium arsenide phosphide). The electrons are ejected from a strained GaAs photocathode when hit with circularly polarized laser light. The electron's spin orientation depends on the polarization of

the incident photon which means the beam helicity is defined by the laser's polarization. Each hall has its own laser setup so that the electron beam going into each hall can be independently controlled. The laser table is schematically shown in Figure 2.2.

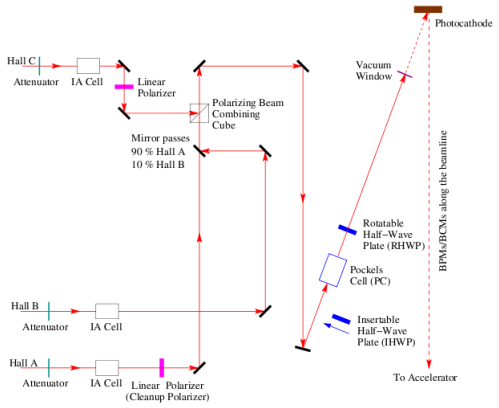

Figure 2.2: Schematic of the laser setup in the injector. The circularly polarizaed light was prepared by the Pockels cell which then illumates a strained GaAs photocathode. Figure is from [44].

On the laser table were 780 nm wavelength lasers that passed through different optical elements to acquire circular polarization. The circularly polarized light was created by using a Pockels cell which acts a voltage-controlled $\frac{\lambda}{4}$ waveplate. The Pockels cell is fed a randomized helicity signal which applies either a positive or negative high voltage, the sign of which causes either a $\pm\frac{\lambda}{4}$ retardation to the photon polarization therefore producing left- or right circularly polarized light.

The circularly light when incident on the GaAs photocathode produces left or right handed electrons. Gallium arsenide has a degenerate $P_{3/2}$ valence band. In an unstrained GaAs crystal when left-handed circularly polarized light (-1 helicity) is incident upon it, the electrons in the $P_{3/2}$ m = -1/2 and -3/2 levels are promoted to the conduction band $S_{1/2}$ m = 1/2 and -1/2 levels respectively. This promotion happens with equal probability resulting in about a polarized electron beam of $\sim$ 50 %. However, in strained GaAs, the degeneracy between the m = $\pm$ 3/2 and $\pm$ 1/2 levels is lifted by inducing an energy gap (3/2 states have larger energy than 1/2 states). In this case, the electrons at $P_{3/2}$ level are promoted to the conduction rather than the $P_{1/2}$ electrons which would theoretically produce 100% polarized left-handed electrons (see Figure 2.3). In practice, the beam polarization is $\sim$ 80-90 %. If we consider right-handed circularly polarized light, the promotion is from the $P_{3/2}$ m = -3/2 to the $S_{1/2}$ m = -1/2.

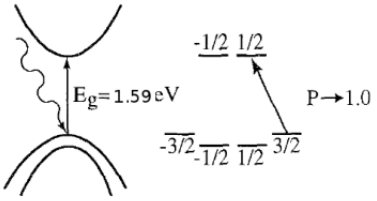

Figure 2.3: Diagram of the band structure and energy gap for strained GaAs. The arrow represents the allowed transition for left-handed photons. Figure taken from Ref [45]

2.2.2 Helicity Controls

At the heart of PREX-II/CREX is helicity control. Experimentally, one would like to be able to reverse the beam helicity without changing any other beam parameters. There are different ways to reverse the beam helicity. These methods include both fast helicity reversal (Pockels cell) and slow helicity reversal (insertable half-wave plate).

As stated in Section 2.2.1, the helicity of the electron beam is correlated with the polarization of the laser light. The laser polarization is prepared by Pockels cell which is fed a helicity signal in which positve and negative high voltages are applied producing left-handed or right-handed circularly polarized light. When the light is incident on the photocathode produces consecutive windows of left- or right-handed electrons. The rate at which the laser polarization is changed is known as the helicity flip rate which is 240 Hz (4.17 msec) for PREX-II transverse running and 120 Hz (8.33 msec) for CREX transverse running. Each period of constant helicity is known as a helicity window with the helicity For 120 (240) Hz running, the helicity patterns are organized in a quartet (octet) pattern as +−+(+−++−+) or -++-(-++−++-). These patterns are formed at multiples of 60Hz to suppress 60Hz electronics noise. The signal is integrated over the multiplet at 30Hz (see Figure 2.4). The first window of multiplet pattern was chosen pseudorandomly. The consecutive window is chosen to have opposite helicity.

The helicity flipping was controlled by the Pockels cell. As shown in Figure 2.4, there is a 100 us delay to allow the Pockels cell to settle thus allowing the helicity window to stabilize. This stabilization period was not included in the parity DAQ. For each multiplet, the detector signal was integrated thus allowing us to compute the asymmetry at the multiplet level.

In addition to the fast helicity reversal by the Pockels cell, an insertable half-wave plate (IHWP) was periodically inserted upstream of the Pockels

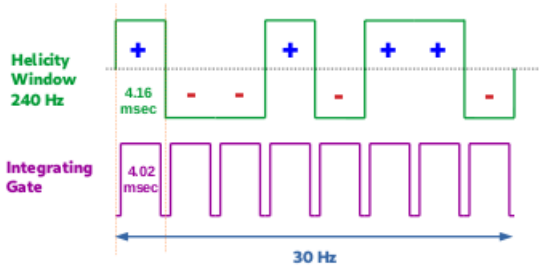

Figure 2.4: Octet pattern structure for 240 Hz running. The integrating gate is 30 Hz [46]

cell as shown in Figure 2.2. The IHWP was intended to rotate the linear polarization state incident on the Pockels cell by 90^o, reversing the circular polarization created by the Pockels cell, therefore changing the helicity of the electron beam. The insertion and retraction of the IHWP was done on a longer time on the order of once or twice a day. The IHWP changes the sign of the measured asymmetry relative to the high voltage applied to the Pockels cell and the polarity signal sent to each data acquisition system. This can provide some systematic cancellation of helicity correlated beam asymmetries (HBCAs). HBCAs refer to any difference in beam between left and right handed polarization states. For example, the charge asymmetry A_I can arise from the difference in the beam charge between the two helicity states. Another example is the beam false asymmetries A_{beam} which arise from position, angle and energies differences incident on target for different helicity states.

2.3 Hall A Beamline

2.3.1 Beam Monitors

To account for HCBAs, requires monitoring the beam parameters during the run. The measured asymmetry requires us to know the total number of electrons in each helicity state. This is defined as

$$A = \frac{D^+ - D^-}{D^+ - D^-} = \frac{\delta D}{2D} \tag{2.1}$$

where D is the integrated detector signal. The detector signal, however, depends on the beam parameters which fluctuate therefore affecting the amount of the electrons that make the main detector. One example is through the

charge asymmetry A_I which arises when the total charge on target differs between helicity windows. The integrated flux is proportional to the total charge on target so careful calibrations between the detector signal and the beam current are performed such that the calibrated detector signal D is normalized to the beam current. To first order, we can separate out the part that sensitive to charge differences i.e.,

$$A = \frac{\delta D}{2D} - \frac{\delta I}{2I}. \tag{2.2}$$

The second term in Equation 2.2 is the charge asymmetry. During the run, the charge asymmetry was minimized using a feedback loop. The charge asymmetry is computed every 7.5 seconds, which is then fed back to the Pockels cell. The high voltages on the Pockels cell are adjusted to minimize the charge asymmetry. The beam charge was measured using beam current monitors (see Section 2.3.1.1).

The measured asymmetry also depends on the beam energy E and scattering angle θ which creates a false asymmetry if the beam fluctuates in a helicity correlated way. To account for this, we modify equation 2.2 by subtracting out the beam false asymmetry A_{beam}

$$A = \frac{\delta D}{2D} - \frac{\delta I}{I} - \sum_i c_i \Delta x_i \tag{2.3}$$

where $\Delta x_i = (E, x, y, \theta_x, \theta_y)$ and c_i are the detector responses due to changes in the beam parameters. In practice, the beam parameters are monitored using beam position monitors which are located at different points along the beamline in Hall A (see section 3.2.2.2).

2.3.1.1 Beam Current Monitors (BCMs)

The experiment used two beam current monitors (BCMs) located about 25 m upstream the target. In the data stream, they are referred to as upstream and downstream. The BCMs are resonant radio-frequency (RF) cavities. These cavities are cyclindrical waveguides, tuned to the frequency of the beam (1497 MHz). This implies that the output voltages are proportional to the beam current [47].

The BCMs are calibrated using an additional monitor called the Unser monitor. The Unser monitor is designed to provide an absolute reference for beam current since its calibration is known. Despite its known calibration, the output signal from the Unser drifts ($\sim \mu$A) due to changes in temperature and

the surrounding magnetic environment. Therefore, the Unser cannot be used to continuously monitor beam current. However, calibrating the main BCMs against the Unser removes this drift. As a result, the main BCMs can be used as continuous current monitors [47].

2.3.1.2 Beam Position Monitors (BPMs)

The position and angle of the beam are measured by two beam position monitors (BPMs) located 7.524m and 1.286m upstream of the target. The energy fluctuations are monitored by three BPMs including BPM12 which is located in the most dispersive point in the arc. As the beam is bent along the arc, the position difference along the dispersive bend, parallel to horizontal plane is measured which in turn is a measurement of the energy difference.

BPMs consist of four wire antennas denoted as X+, X-, Y+ and Y-. The antennas are symmetrically placed $\pm$ 45^o with respect to the horizontal axis. The wire signal is proportional to the intensity and inversely proportional to the distance from the beam to wire. The signals are read out in the data stream. The beam position is calculated as

$$x' = \kappa \frac{X+ - X-}{X+ + X-}, \quad y' = \kappa \frac{Y+ - Y-}{Y+ + Y-}. \tag{2.4}$$

The constant κ is the wire calibration constant, which is distance between the center of the stripline axis to the base of the antennas, $\kappa = 18.76$ mm. The x' and y' positions are rotated such that x is the horizontal beam position and y is vertical in the Hall. The x and y positions in the Hall is given by [48].

$$x = \sin(45^o)x' + \cos(45^o)y', \quad y = \cos(45^o)x - \sin(45^o) \tag{2.5}$$

2.3.2 Raster

The beam size for JLab is on the order of a few hundred microns. This can cause target damage at high currents. To accommodate the heat load on the target, the beam gets rastered to deposit power over a large area. The raster consists of a pair of horizontal and vertical dipoles driven by $\sim$ 25 kHz frequency (X and Y) triangular wave which sweeps the beam over a rectangular area on the target [49]. For the lead and carbon targets, the raster was 4 mm x 6 mm. While for the calcium targets, the raster was 2 mm x 2 mm. The raster size was confirmed using spot++, a program that allows us to check the spot size at the target.

2.3.3 Beam Modulation

Beam modulation or "dithering" is a technique used which measures the detector response due to changes in beam parameters (energy, position and angle) by steering the beam.

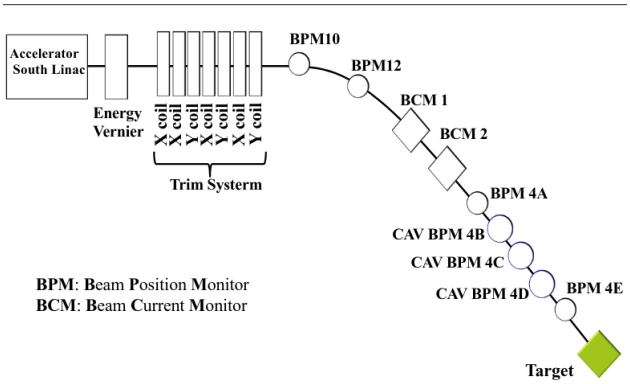

Figure 2.5: Full picture of the Hall A Beam including the BCMs. Figure from [48]

The beam modulation system consists of six air-core coils upstream (three in X and 3 in Y) of the dispersive arc which was were used for both the position and angle modulation. The energy modulation was done by using the energy vernier in the accelerator's south linac. The beam is modulated in 15 Hz cycles with $\sim$ 100 micron amplitude. The 15 Hz was chosen to suppress 60 Hz electronics noise while the modulation amplitude is larger than natural beam fluctuations ($\sim$ 10 microns) which ensures the modulation covers the phase space of the jitter. The sine wave was generated with a VM1-4145 function generator. The VM1-4145 is connected to trim cards which are read out by the parity DAQ. The waveform phase represents each integrating period. There are 8(16) phases per period for 120 (240) Hz running.

In one dithering cycle, each coil is activated in sequence for about 3.3 seconds. There are 10 minute pauses between dithering cycles. During a cycle, the coils displace the beam by about less than 600 microns [50].

2.4 Polarimetry

Both PREX-II and CREX required polarimetry measurements at 1% accuracy. In Hall A, the beam polarization is measured independently by two polarimeters, the Compton and the Møller.

2.4.1 Compton Polarimetry

The Compton polarimeter measures the beam polarization by use of Compton scattering. The beam polarization is extracted by the measuring the asymmetry for different beam helicities scattering off a circularly polarized photon beam. The asymmetry is defined as the fractional difference between scattering photon signals S between positive and negative helicity electrons.

$$A_{exp} = \frac{S_+ - S_-}{S_+ + S_-} = P_e P_\gamma A_{th} \tag{2.6}$$

Here P_γ is the photon polarization and A_{th} is the theoretical Compton asymmetry for 100% photon and electron polarization. A_{th} is a well known function of the photon energy. It is negative at lower photon energies including a zero crossing point at the nominal photon energy. It is positive for higher photon energies up to a point called the Compton edge. The Compton edge is defined as the maximally allowed photon energy given the kinematics. The photon energy corresponds to energy lost by electron in the scattering, allowing one to measure the polarization either by using the photon energy and/or by measuring the detected electron position after a dispersive magnetic element [3].

The Compton apparatus is shown in Figure 2.6. At the entrance of the Hall, the electron beam is bent by two magnetic dipoles of the Compton chichane to a parallel path where the electrons scatter off of circularly polarized laser photons in the Fabry-Perot cavity. The initial photon polarization is linear so a quarter wave plate was placed outside the cavity. The backscattered photons are measured by a photon detector. The signals from the photon detector are used to extract the beam polarization. A third dipole separates the scattered electrons (about 1 in every 10^9) from the unscattered electrons. The scattered electrons can detected with an electron detector. A fourth dipole diverts the remaining part of the beam to the target [51].

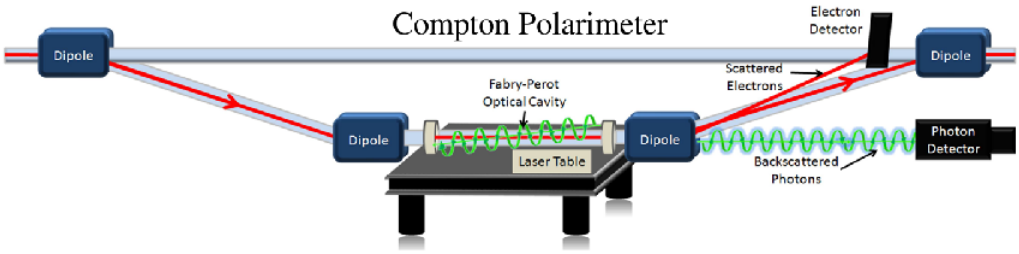

Figure 2.6: A drawing of the Compton polarimeter. One can directly see the electron beam path as it goes through the Compton chicane [52].

2.4.2 Møller Polarimetry

Downstream of the Compton polarimeter is the Møller polarimeter. The Møller polarimeter measures the beam polarization making used of Møller scattering off of polarized electrons in a ferromagnetic foil. Unlike the Compton, Møller measurements are invasive and can not be done concurrent with production running. Dedicated Møller measurements were taken at various points throughout the run. Similarly to the Compton, one can measure Møller asymmetry defined as the fractional difference in the number of electrons between positive and negative helicity states is given by

$$A_{Moll} = \frac{N^+ - N^-}{N^+ + N^-} = P_t P_b \langle A_{zz} \rangle. \tag{2.7}$$

Here $_{zz}\rangle$ is the longitudinal analyzing power average over the detector acceptance. The analyzing power is a function of center of mass (CM) scattering angle θ_{CM} and is maximal $\frac{7}{9}$ at $\theta_{CM} = 90^o$ for a beam traveling in the z-direction. The target and beam polarization is given by P_t and P_b respectively.

The Møller polarimeter is schematically shown in Figure 2.7. The Møller target is an iron foil target which acts as a polarized electron target when fully magnetized out of plane by a 4T superconducting magnet. The spectrometer consists of four quadrupoles (of which only three were used) to focus and select the Møller electrons and a dipole to bend the electrons. The fourth quadrupole was added for the 12 GeV upgrade. Twin detectors are located downstream the dipole which are symmetrically placed on both sides of the beamline [53].

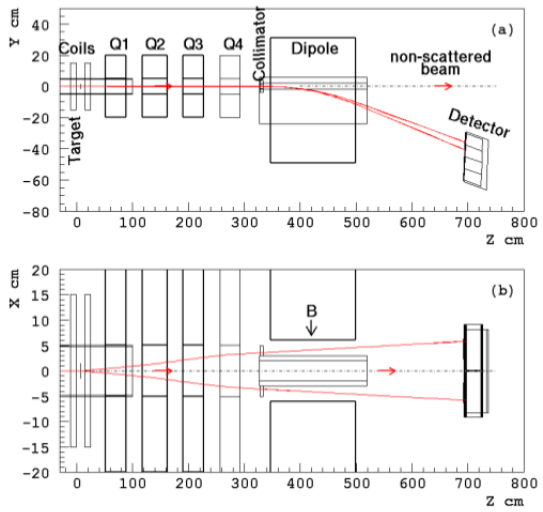

Figure 2.7: (a) Side View of the Møller Polarimeter (b) Top View of Møller Polarimeter [53].

2.5 Targets

The PREX-II and CREX experiments used two target ladders that moved independently of each other. One was the optics ladder, which had targets to commission to the spectrometer, while the other was the production ladder, containing the main production targets. The optics ladder was positioned 45^o above the horizontal and was water cooled. The production ladder was positioned horizontally and moved linearly with the direction of perpendicular to beam line. Unlike the optics ladder, the production ladder was cooled with circulating 14 K He gas. Both ladders were designed to move within the same xy plane and aim at the same z location in the beamline [54]. The ladders were housed in an aluminum chamber. The main part was 33 cm long and about 61 cm in diameter [55]. 10^{-5} Torr vacuum was maintained inside the chamber which was secured by radiation hard metal seals [56]. The target chamber is shown in Figure 2.8.

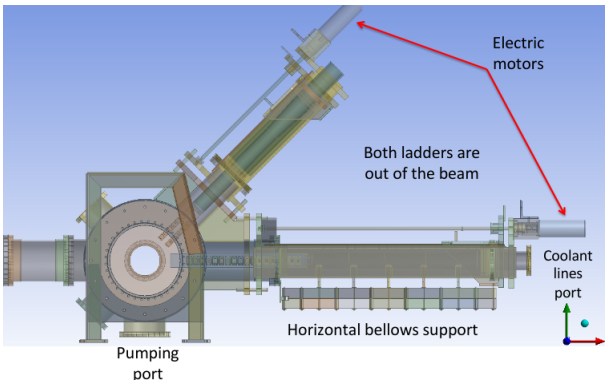

Figure 2.8: Beam view of the Target chamber that houses the target ladders. Figure from [55]

The optics ladder was designed to have five positions in the beam, four of which housed the different targets in the optics ladder. The production ladder was designed to have 18 positions in the beam for each target in the production ladder. The targets on each ladder is given in Table 2.1.

Optics Ladder	
Carbon Hole	$\sim 0.1\ g/cm^2$
Watercell	
thin C foil	$0.1 \pm 0.05\ g/cm^2$
thin natural Pb	$0.05 \pm 0.01\ g/cm^2$
thin ^{40}Ca	$0.05 \pm 0.01\ g/cm^2$

Production Ladder	
Carbon Hole	$\sim 0.1\ g/cm^2$
(9X) ^{208}Pb/Diamond	0.5 mm
^{208}Pb/Graphite	0.5 mm
^{48}Ca (tilted)	$1 \pm 0.1\ g/cm^2$
^{40}Ca	$1 \pm 0.1\ g/cm^2$
thick C	$0.5 \pm 0.1\ g/cm^2$
Pb/Diamond	0.5 mm
Pb/Graphite	0.5 mm

Table 2.1: Targets required for PREX/CREX physics and optics calibrations. Tables reproduced from [56]

2.5.1 Production Ladder

The production ladder as shown in Figure 2.9 consists of targets used the transverse asymmetry measurements. The main production targets for PREX-II were the ^{208}Pb targets which were based of the design of PREX-I. Each ^{208}Pb target was about half a millimeter thick, one inch square sandwiched between two diamond foils of a quarter millimeter thickness. A thin layer of Apiezon L vacuum grease was applied between the diamond and lead to improve contact. The compound target was clamped with spring-like washers to further ensure contact to account for changes in beam temperature [56].

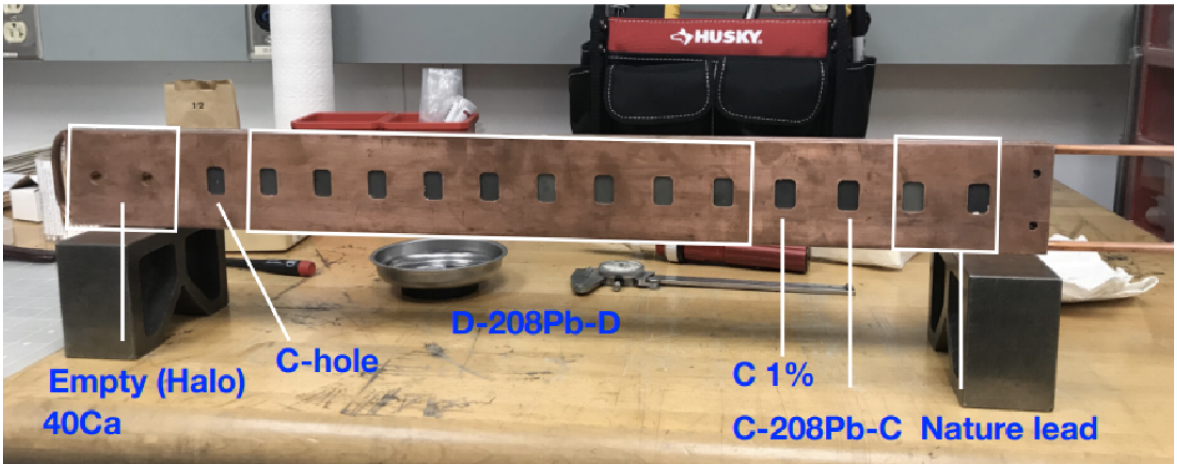

Figure 2.9: Targets on Production Ladder. The Ca48 target which is not shown was located where the halo (empty target) slot for CREX. Figure from [57]

Because the lead target was sandwiched by diamond foils, it was important to measure the transverse asymmetry on carbon. The diamond foils diluted the measured asymmetry on the lead targets. For the A_T measurement, the carbon target was a 1% radiator. In addition, a carbon hole target was used to check the raster size and center the beam on target.

The ^{40}Ca target was a 1.1 g/cm^2 thick target of 99.93% isotopic purity. The ^{48}Ca target used during CREX, consisted of a stack of three ^{48}Ca foils, whose total thickness was about 1.1 g/cm^2. The ^{48}Ca target had about an 8% contamination due to ^{40}Ca.

2.5.2 Optics Ladder

The main targets of interest on the optics ladder were the thin carbon target (0.2% radiator) and the water cell target. The thin carbon target was used to calibrate the spectrometer so that we can accurately reconstruct the interaction at the target (angle and momentum). The water cell target consisted of 5 mm of water surrounded by 0.05 mm thick stainless steel walls. The purpose of this target was to measure the relative difference in momentum between the hydrogen and oxygen to get an absolute spectrometer angle calibration.

2.6 Septum Magnet

PREX-II and CREX were designed at a 5^o scattering angle with the same fixed target position. The Hall A High Resolution Spectrometers only have a minimum opening angle of 12.5^o. This motivated the use of an additional magnet, the septum, to horizontally (in-plane) bend the scattered electrons into the aperture of the spectrometers. The septum magnet was located between the target chamber and the first quadrupole of the spectrometer. The septum is shown Figure 2.10.

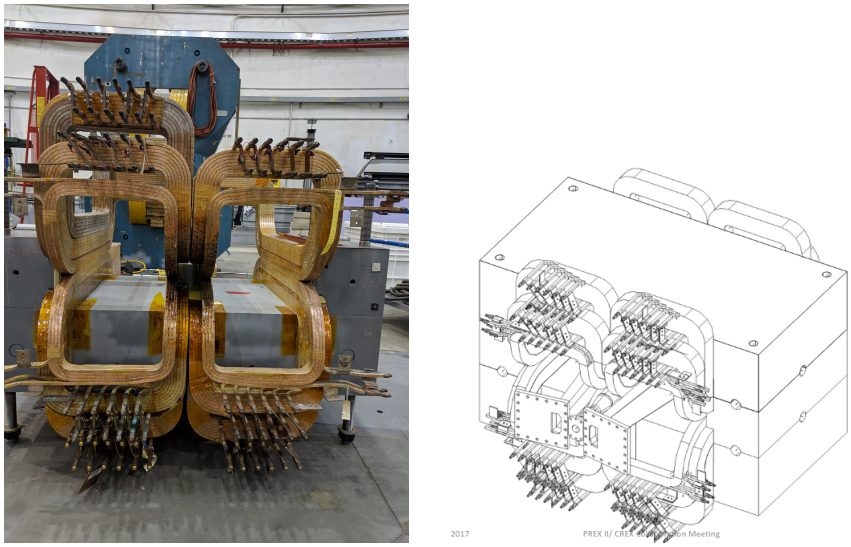

(a) Septum Coils (b) Septum Diagram

Figure 2.10: (a) Septum coils. The coils are symmetrical placed left/right with respect to the beamline. Photo credit to Dr. C. Gal. (b) Septum Magnet [3]

2.7 Acceptance Defining Collimator

At the entrance of the Q1 of the HRS, an acceptance defining collimator was placed in the aperture of the Q1. The collimator which was made of 8 cm thick tungsten defined the angular acceptance of the experiment [58]. The collimator was 9 cm in height and was designed to accept the scattered electrons with scattering angles of roughly about 3^o to 8^o [58]. The Q1 collimator is shown in Figure 2.11.

For PREX-II/CREX, the symmetry of the apparatus is very important. The collimators were surveyed and designed to be installed within ± 1 mm in both the horizontal and transverse directions to be preserve left/right and up/down symmetry [56].

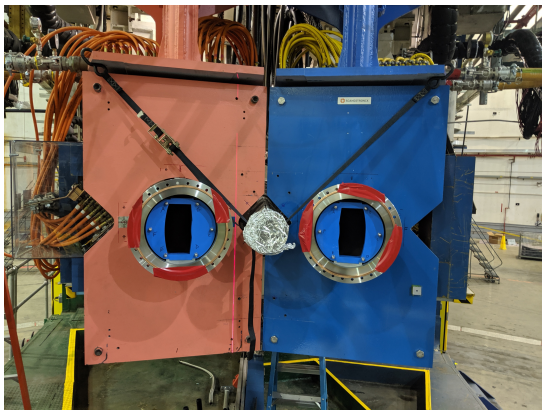

Figure 2.11: Beam's eye view of the Q1 collimators. Photo credit by Dr.C Gal

2.8 High Resolution Spectrometers (HRSs)

To focus the scattered electrons, a pair of High Resolution Spectrometers (HRSs) were used. The spectrometers were designed to have 10^{-4} momentum resolution for particles between 0.8-4.0 GeV/c with angular acceptance of ±30 and ± 60 mrad in the horizontal and vertical planes respectively. The HRSs have a QQDQ magnet configuration as shown in Figure 2.12. The dipole has a 45^o bend which defines the dispersive direction. The first quadrupole serves the purpose of focusing the electrons in the dispersive direction, while the second quadrupole focuses in the transverse (non-dispersive) direction. The third quadrupole also focuses the electrons in the transverse direction onto the detectors [49]. For PREX-II and CREX, the magnets were set in such a way

to focus the elastically scattered electrons onto the main detectors (see section 2.9.2). More about the optics will be discussed in Chapter 3 of this thesis.

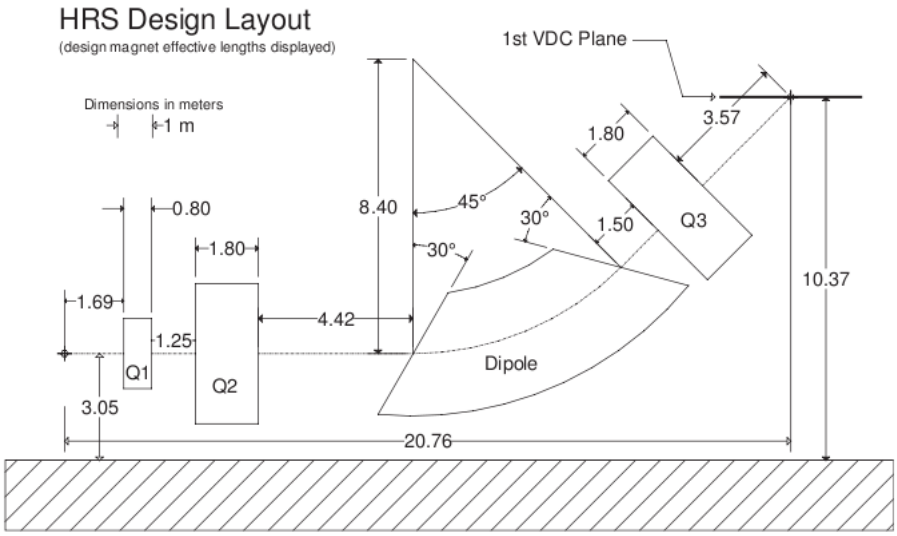

Figure 2.12: Design Layout of the HRSs. Figure from [49]

2.9 Detector Package

2.9.1 Vertical Drift Chamber

Particle tracking is done by using a pair of vertical drift chambers (VDCs) located about 3.5 m downstream of the Q3 exit which lay along the lab's horizontal plane. Each VDC chamber consists of two 2118x288 mm^2 wire planes, and the two chambers are separated by 335 mm (see Figure 2.14). A wire plane consists of sense wires which are grounded and horizontally placed between two high voltage planes (see Figure 2.13). The high voltage planes are held at -4 kV high voltage thus resulting a uniform electric field pointing vertically away from the wires (solid lines in Figure 2.12). Near the wire, the field transitions from uniform to quasiradial and in (ellipses in Figure 2.12). The chamber is filled with a mix of argon and ethane gas such that when a charged particle traverses the gas, it ionizes along the track. The ionized electrons are accelerated by the electric field toward the sense wires, away from the trajectory along the path of least time. The accelerated electrons produce an electron avalanche, which produces a signal which is collected by

the time to digital converters (TDCs). The time that the TDC measures can be converted into a perpendicular distance between the trajectory and the sense wire plane. Fitting these distances, one can define local cross over point Q_i and local trajectory angle θ_{Q_i} for a given track for a given plane i. With four wire planes on each arm, the 3D position and angle of the track can be reconstructed.

The wire planes are oriented in a UV configuration which has their wires perpendicular to each other. The wires are inclined at 45^o with respect to dispersive and non-dispersive directions. A nominal particle track traverses the VDC at a 45^o angle (Figure 2.14) [49, 59].

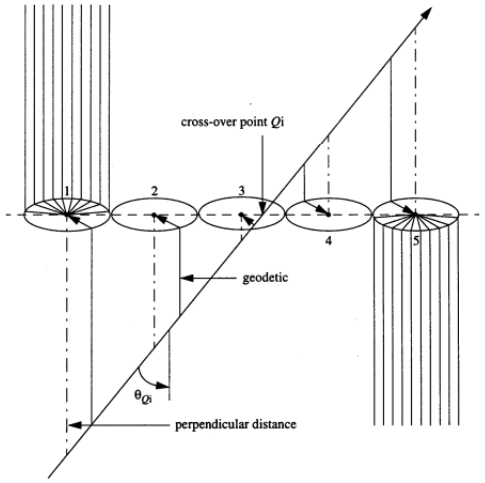

Figure 2.13: Particle trajectory going through a VDC wire plane. The solid lines are electric field lines which are uniform away from the sense wires and quasiradial toward the sense wiress. The measured drift time gives information of the perpendicular distance between a trajectory and sense wires. Figure from [59].

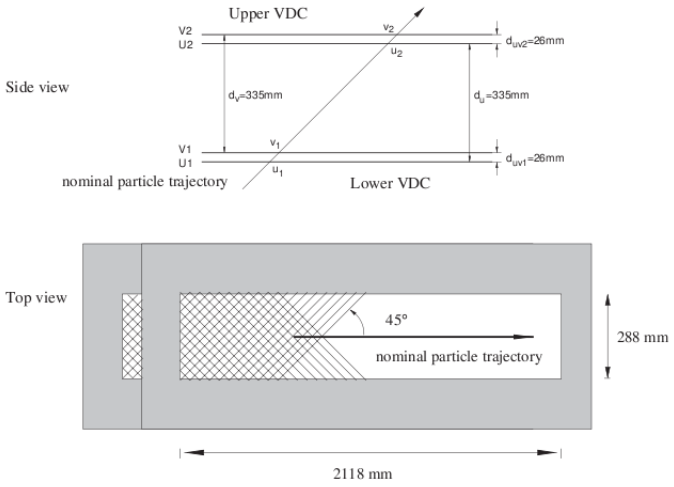

Figure 2.14: Schematic of the VDCs [59]

2.9.2 Integrating Detector System

Downstream of the VDCs inside of the detector huts, contains the integrating detector system. The integrating detector system consisted of the tandem pair main detectors which measured the transverse asymmetry. Downstream of the main detectors were the A_T detectors which were used to monitor any residual transverse horizontal polarization (discussed in Chapter 5) during production running. Independent of the integrating detector system, were two Gaseous Electron Multiplier (GEM) systems for high rate tracking. This is shown in Figure 2.15.

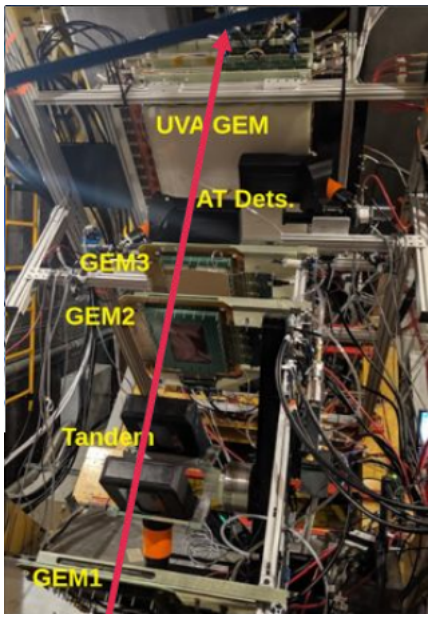

Figure 2.15: Integrating Detector System. The tandem detectors were mounted on a stand in between GEM planes 1 and 2 of the small 3 GEM detector array. The A_T detectors were downstream the main detectors but upstream the large 3 GEM detector array.

The PREX and CREX measurements use thin quartz detectors connected to photomultiplier tubes (PMTs). The design made use of total internal reflection inside the quartz to collect Cherenkov light from the passage of electrons. The roughly 5 mm detectors were 3.5x16 cm^2 with an active region 10 cm and a "stubby" region of 6 cm. The "stubby" region consisted of two regions, a 4 cm "light guide" and 2 cm buffer for alignment purposes. The stubby piece served as a spacer while the elastically scattered electrons traversed the active region of the detector. The quartz pieces were mounted onto rails and had a 3D printed ABS-plastic enclosure with Kapton windows [60–62]. The tandem detector system is shown in Figure 2.16.

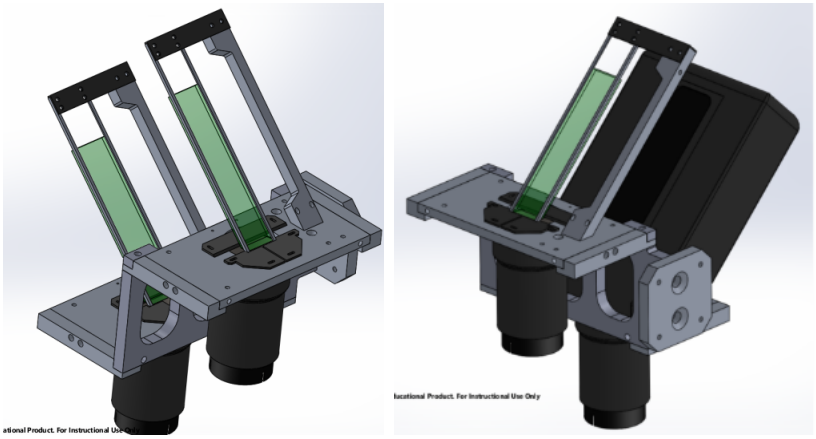

Figure 2.16: Tandem Detector shown with and without plastic enclosure

Two additional quartz detectors were in each arm were placed downstream of the main detectors in order to monitor any residual transverse polarization. The detectors were built using the same design as the main detector. The A_T detectors were also 5 mm thick, with an active area of 3.5 x 10.0 cm^2. Similarly to the main detectors, the A_T detectors were mounted on Bi-slides (2" and 4" for x and y motion respectively) [60–62]. The A_T detectors are shown in Figure 2.17.

Figure 2.17: A_T detectors. Photo taken by Dr. D. McNulty

2.9.3 Gaseous Electron Multiplier (GEM) Detector Systems

Separate from the integrating detector system were two independent GEM systems. The smaller system consists of three 10x20 cm^2 mounted on a stand with the main detectors while the larger three GEM system (50x60 mm^2) were located downstream of the main detectors. GEM detectors consist of a drift electrode, readout plane and three GEM foils in between. Each foil is held at a potential voltage thus creating an electric field. A traversing particle ionizes the gas medium. The ionized electrons are accelerated to foils which have a large field. This further allows more electrons to be ionized thus creating an electron avalanche. See Figure 2.18.

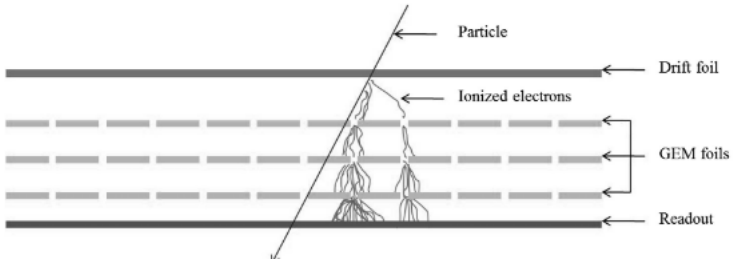

Figure 2.18: Schematic layout of the Gaseous Electron Multiplier (GEM) detector [63]

The GEM detectors provide additional tracking for the experiment. The advantage of using GEMs over the VDCs is that they can handle a higher rate ($\sim$ MHz) compared to VDCs, which can handle up to about 250 kHz rate.

2.10 Data Acquisition Systems (DAQ)

The experiments required to be able to operate in both integrating mode and counting mode. There was a counting DAQ for low current calibrations and an integrating DAQ for production running. Our detector setup allowed us to freely switch between counting and integrating mode by swapping cables.

2.10.1 Counting DAQ

The main triggers for the low current counting runs were scintillator triggers. The first scintillator called S0 (185x25x1 cm^3) laid horizontally above the

second VDC chamber was the main trigger. S0 had two PMTs, one on each end called S0A and S0B and the trigger of the logical and of S0A and S0B was called T1. Another scintillator, S3 (71x9x1 cm^3) was downstream of UVA GEM array and its trigger was called T3. However, the S3 scintillator for PREX-II had a much smaller acceptance than S0 so it was only used for sysmtematic studies. PREX-II also had additional triggers T2 (logical or of S0A and S0B), T4 (upper quartz) and T5 (downstream quartz) and T6 (and of T1 and T3), however, T4-T6 were not used for most of the run [64]. For CREX, the quartz triggers were removed and the T3 trigger consisted of a digital OR signal of three S3-sized scintillators to closely mimic the acceptance of S0. T1 (S0A and S0B) remained the main trigger for all Q^2 analysis.

The counting DAQ read out the ADC spectra for the quartz detectors and scintillators. The trigger rates were read and tracking information from the VDcs were read out. The raster current and beam monitor was read out in the data stream to ensure that the spot size on target (see section 2.3.2).

2.10.2 Integrating (Parity) DAQ

The integrating DAQ is used to accumulate the data during the main and transverse measurements. It consists of four VME crates: counting house (CH), left HRS (LHRS), right HRS (RHRS) and injector. The crates were located throughout the accelerator, both inside in the Hall and along the beamline to minimize noise and signal attenuations.

The parity DAQ used 18-bit analog-to-digital converters (ADCs) based on the QWeak design. The ADCs were designed to accommodate a faster data acquisition rate while suppressing pedestal drifts and non-linearity. They also allowed for further subsegmentation of the integration window which allows to systematically check the integration gate timing. The signals for the beam monitors and detectors were read out through the ADCs [65].

The parity DAQ was also able to read out the scaler information from the beam modulation system. The scaler read out the frequency of the beam modulation through a voltage-to-frequency (V2F).

Chapter 3

Optics

Optics is a crucial aspect of the PREX-II and CREX experiments. Optics refers to the transformation required to reconstruct the interaction at the target given what we measure at the focal plane. The tracks at the VDCs are our snapshots of the interaction at the target. An accurate reconstruction of the interaction point requires calibrating the spectrometer. After calibration, the tracks at the target are reconstructed using the optics matrix. The optics matrix reconstructs tracks from the focal plane to the target region. We use the target variables to reconstruct our kinematics which will ultimately be compared to simulation.

In addition to spectrometer calibration, we use the VDC tracks to align our detectors. Because the detectors are downstream the focal plane, the VDC tracks are extrapolated to the quartz detectors. The upstream main detector was about 1.3 meters downstream the focal plane while the A_T detectors were about 1 meter downstream of the upstream main detector. The tracks that intersect the quartz detectors define the acceptance of the experiment.

3.1 Optics Formalism

3.1.1 TRANSPORT Formalism

The beam transport of charged particles through a magnetic spectrometer can be described in the TRANSPORT formalism [66]. A trajectory of a charged

particle relative to the optic axis is described by a vector

$$\boldsymbol{x} = \begin{bmatrix} x \\ \theta \\ y \\ \phi \\ \delta \end{bmatrix} \tag{3.1}$$

where x is the displacement along the dispersive axis, θ is the tangent of the angle in the dispersive plane with respect to the reference trajectory ($\theta = \mathrm{dx/dz}$, where z is along the direction of the optic axis), y and ϕ are the equivalents in the transverse plane, and δ is the fractional deviation of the momentum of the trajectory from the the central momentum. Transport through a series of magnetic elements up to the focal plane can be represented as a matrix equation to first order and tensor equation to arbitrary order. Any particle trajectory can be expressed as a Taylor expansion about the central trajectory i.e.,

$$x_i = \sum_{j=1}^{5} R_{ij} x_j(0) + \sum_{j=1}^{5} \sum_{k=1}^{5} T_{ijk} x_j(0) x_k(0). \tag{3.2}$$

Here R_{ij} and T_{ijk} are the first and second order forward transport matrices. R_{ij} is a 5x5 matrix while T_{ijk} is a 20x20 tensor. In reality, we measure the charged particles at the focal plane and reconstruct the interaction point. This involves the inverse of these matrices. A more detailed description of the optics calibration is given in section 3.3.

3.1.2 PREX/CREX Optics

To first order the matrix R is given by

$$\begin{bmatrix} (x|x) & (x|\theta) & (x|y) & (x|\phi) & (x|\delta) \\ (\theta|x) & (\theta|\theta) & (\theta|y) & (\theta|\phi) & (\theta|\delta) \\ (y|x) & (y|\theta) & (y|y) & (y|\phi) & (y|\delta) \\ (\phi|x) & (\phi|\theta) & (\phi|y) & (\phi|\phi) & (\phi|\delta) \\ (\delta|x) & (\delta|\theta) & (\delta|y) & (\delta|\phi) & (\delta|\delta). \end{bmatrix} \tag{3.3}$$

PREX-II/CREX required point to point imaging in order to minimize the spot size at the main detectors. To first order, this requires the matrix elements $(x|\theta)$ and $(y|\phi)$ to be zero at the detectors. The HRS is designed to have large dispersion $(x|\delta)$ so $(x|\theta)$ being zero means particles of one momentum focus to one "X" in the focal plane, independent of the scattering angle. This allows the rejection of inelastic states to the main measurement. As stated in Chapter 2, the active area of the main detectors is 10 (dispersive) x 3.5 (transverse) cm^2. The $(y|\phi)$ being zero requires the accepted electrons to focus onto the transverse dimension of quartz regardless of the scattering angle. This is schematically shown in Figure 3.1.

For point-to-point imaging, the magnification in the x and y planes is given by magnitude of the $(x|x)$ and $(y|y)$ respectively for a given spot size [66].

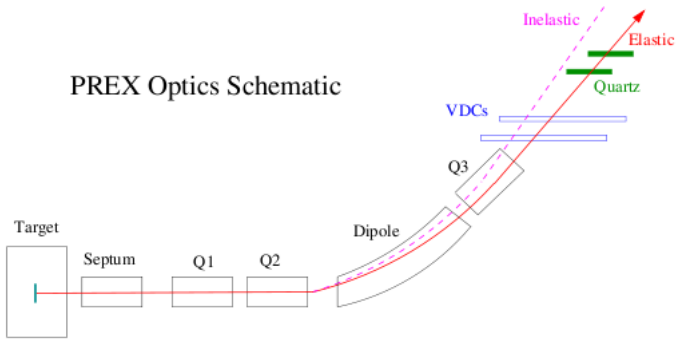

Figure 3.1: PREX Optics Schematic. The focal plane of the spectrometer coincides with the first lower plane of the VDC.

3.2 Coordinate Systems

The variables used in the optics calibration are measured in different coordinate systems [67]. A summary of the coordinate systems is presented here. A more detailed description can be found here [68]. The figures presented in this section were taken from [69].

- **Hall A Coordinate System (HCS)**: The origin of the HCS is at the Target center. It's defined by the intersection of the electron beam and the vertical symmetry axis of the target system. Because of the septum, the center is about 0.7 m upstream of the hall center. Direction $\hat{z}$ is along the beam direction, $\hat{y}$ is vertically up and $\hat{x}$ is beam left. See Figure 3.2.

- **Target Coordinate System (TCS)**: Each spectrometer has its own TCS. $\hat{z}$ is defined along the central ray and points away from the target. $\hat{x}$ points down and defines the dispersive direction. The $\hat{y}$ direction points away (toward) from the beamline for the left (right) spectrometer. The origin of the TCS is defined along $\hat{z}$ at a distance L, measured from the target center to the central sieve slit hole. See Figure 3.3. Ideally, the TCS has the same origin of the HCS.

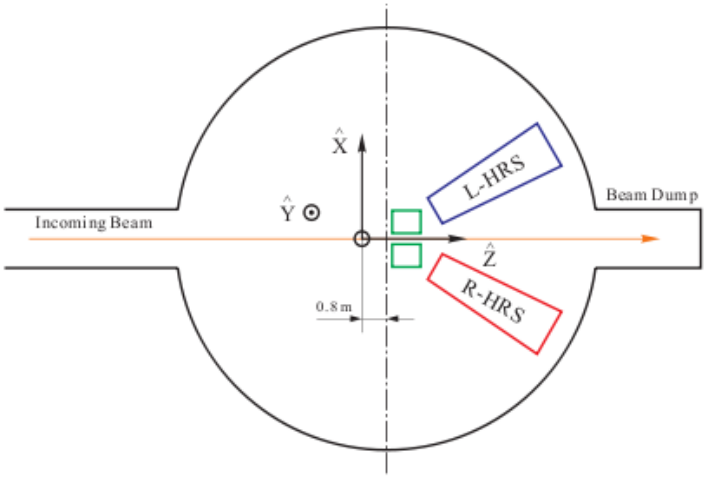

Figure 3.2: Top View of Hall Coordinate System

- **Detector Coordinate System (DCS)**: The intersection of wire 184 of VDC1 U1 plane and the perpendicular projection of wire 184 of the

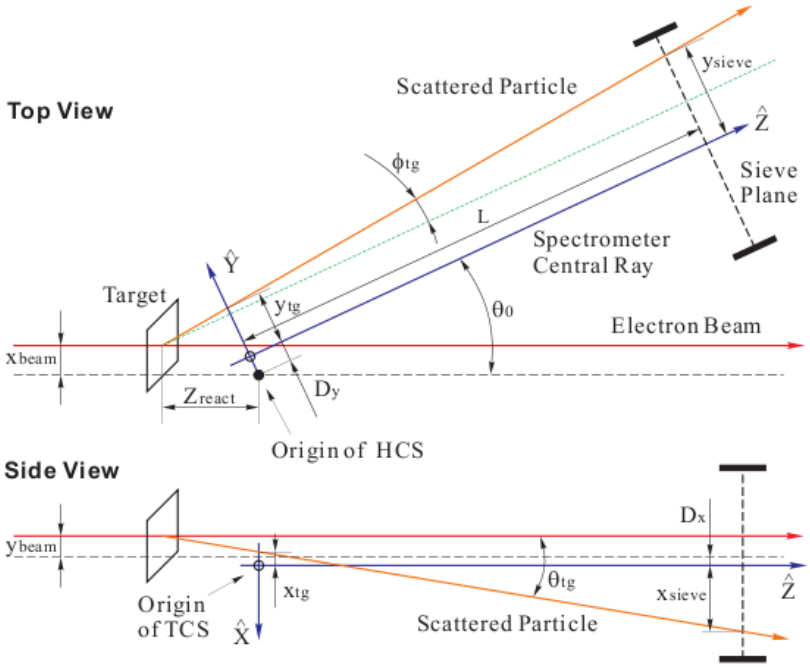

Figure 3.3: Top and Side Views of the Target Coordinate System

VDC1 V1 plane onto the VDC1 U1 plane defines the origin of the DCS. In this system, $\hat{z}$ is perpendicular to VDC plane pointing up, while $\hat{x}$ is along the VDC's long symmetry axis pointing away from the dipole. See Figure 3.4.

- **Transport Coordinate System (TRCS) at the focal plane**: The TRCS at the focal plane is generated by rotating the DCS 45^o clockwise about its y-axis as shown in Figure 3.5. Its z-axis ideally coincides with the spectrometer optic axis.

- **Focal plane Coordinate System (FCS)**: The focal plane Coordinate System is a rotated coordinate system used for the optics calibration. This system is obtained by rotating the DCS about its y-axis by an angle ρ, where ρ is the angle between the local central ray[1] and $\hat{z}$ axis of the DCS. As a result, $\hat{z}$ in the FCS is a function of the relative momentum $\frac{\delta p}{p}$ (Figure 3.6).

[1]Ray with $\theta = \phi = 0$ for a given $\frac{\delta p}{p}$

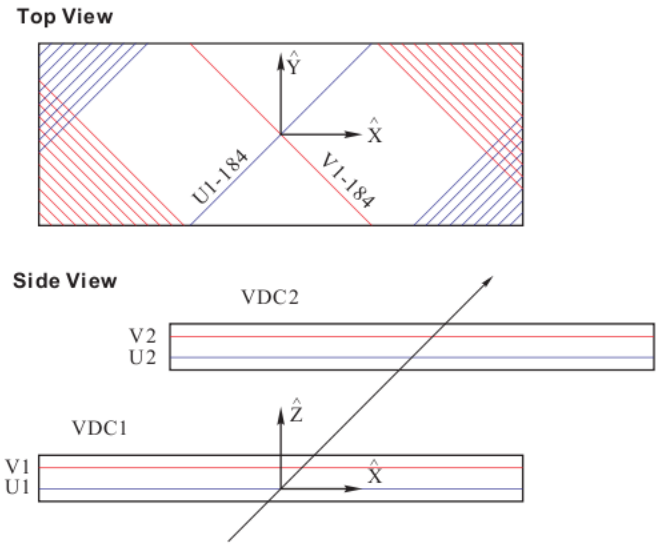

Figure 3.4: Detector Coordinate System

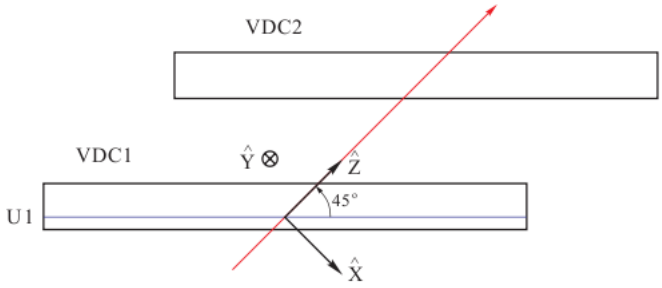

Figure 3.5: Transport Coordinate System (side view)

For each event, the position (x_{det},y_{det}) and angle (θ_{det},ϕ_{det}) are measured at the VDCs in the DCS. The dispersive direction is given by x and θ while the transverse is given by y and ϕ. These variables get corrected for any detector offsets from the ideal central ray and transformed to give the focal plane coordinates x_{fp}, y_{fp}, θ_{fp} and ϕ_{fp}. The transformations are given in [68]. These variables are used to calculate x, θ, y,ϕ and δ in the TCS. During optics calibration, the data is taken with the raster off and x_{tg}, the vertical beam position on target is effectively fixed at zero requiring that the beam on target is within 250 μm of the HCS origin. This reduces the number of unknowns. A set of tensors (5^{th} order) link the focal plane variables to the target variables according to

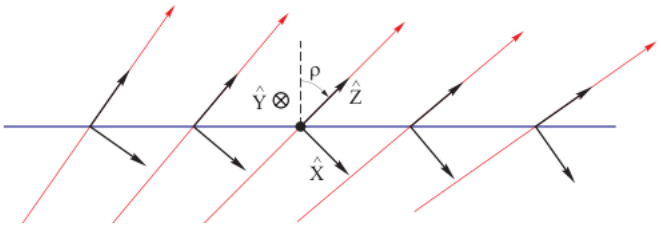

Figure 3.6: Focal Plane Coordinate System

$$y_{tg} = \sum_{j,k,l} Y_{jkl} \theta_{fp}^{j} y_{fp}^{k} \phi_{fp}^{l} \tag{3.4}$$

$$\theta_{tg} = \sum_{j,k,l} T_{jkl} \theta_{fp}^{j} y_{fp}^{k} \phi_{fp}^{l} \tag{3.5}$$

$$\phi_{tg} = \sum_{j,k,l} P_{jkl} \theta_{fp}^{j} y_{fp}^{k} \phi_{fp}^{l} \tag{3.6}$$

$$\delta = \sum_{j,k,l} D_{jkl} \theta_{fp}^{j} y_{fp}^{k} \phi_{fp}^{l}. \tag{3.7}$$

The tensors Y_{jkl},T_{jkl},P_{jkl},D_{jkl} are polynomials in x_{fp} e.g.,

$$Y_{jkl} = \sum_{i=0}^{m} C_i^{Y_{jkl}} x_{fp}^{i}. \tag{3.8}$$

3.3 Optics Calibration

Determining the tensor elements is critical to understanding our kinematics. Optimizing the optics database requires data covering a wide range in momentum acceptance and solid angle acceptance. This data is taken without the raster and with the sieve slit collimators inserted into the beam path. The sieve collimators are shown in Figure 3.7.

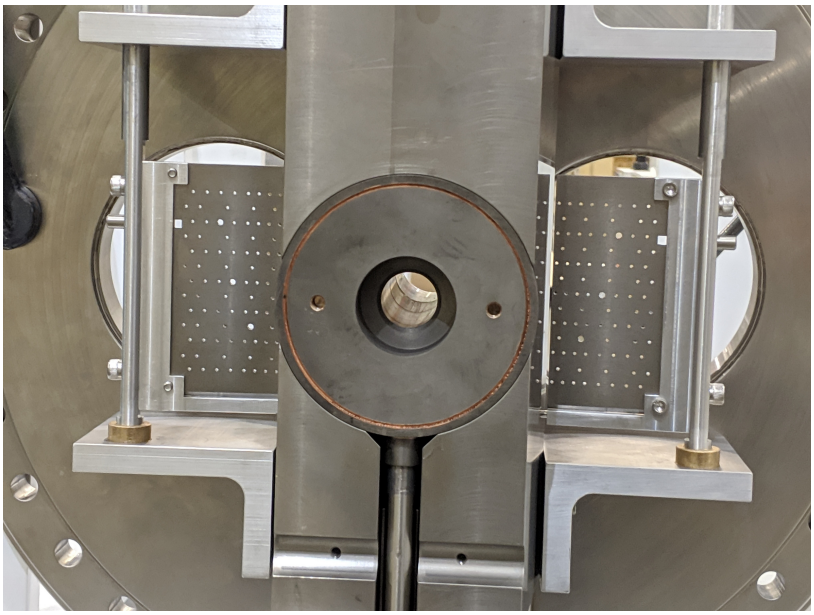

Figure 3.7: Sieve Slit Collimators

3.3.1 Spatial and Angular Calibration

The angular calibration was done first because the spatial and momentum calibrations depend on this. The beam and surveyed positions of the sieve relative to the target was used to calculate the expected position for each sieve hole. The details of the hole positions are shown in Figure 3.8. The position for each hole was calculated using the matrix elements. The difference between the squares of the expected position and calculated position is minimized. The output gives the theta and phi tensor elements. The spatial calibration is done by the same procedure [45].

3.3.2 Momentum Calibration

The momentum calibration involved taking data on the thin carbon foil at several spectrometer central momentum settings P_o to sweep the electrons across the focal plane. For each event passing through a given hole, the scattering angle is calculated. Each sieve hole in the same column has a fixed scattering angle. From this, the expected momentum of each hole is calculated and hence the fractional momentum for a given P_o is calculated. The difference of squares of the actual central value and the expected value is minimized [45].

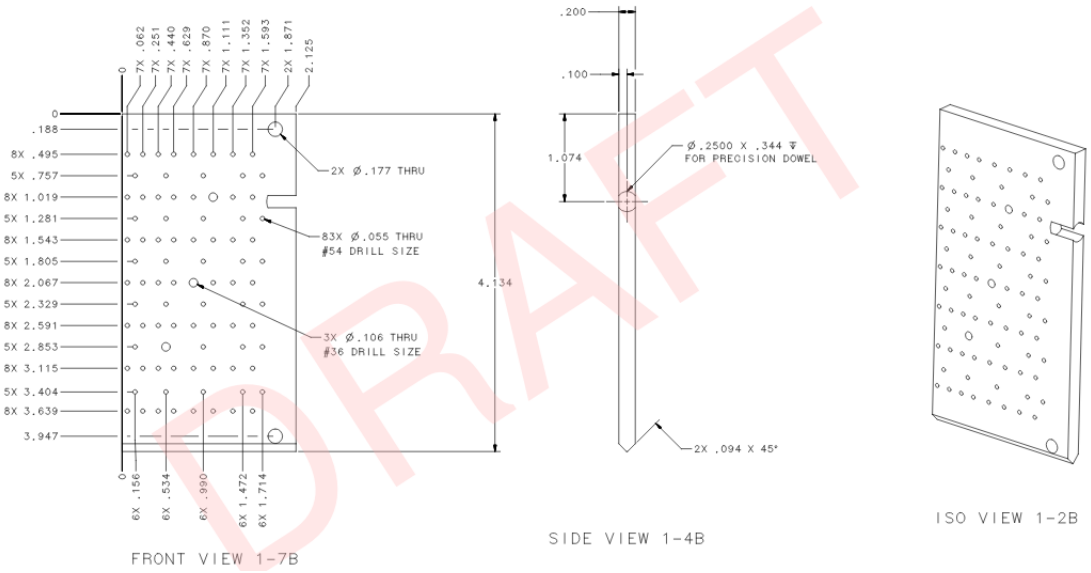

Figure 3.8: CAD drawing of RHRS Sieve. All dimensions are given in inches. The large sieve holes are used a reference for the tracks

3.4 Optics Simulation Tools

Evaluating the acceptance is crucial to interpreting the PREX-II and CREX results. The angular experimental acceptance is defined by the Q1 collimator while the momentum acceptance is defined by the dimensions and placement of the main detector. With this information, we define an acceptance function $\epsilon(\theta)$ which is the probability that an electron as a function of kinematic parameters that reaches the detector, scattered off of ^{208}Pb[2]. To interpret the measurement with theoretical models, one must integrate over the acceptance function:

$$\langle A \rangle = \frac{\int d\theta \sin\theta A(\theta) \frac{d\sigma}{d\Omega} \epsilon(\theta)}{\int d\theta \sin\theta \frac{d\sigma}{d\Omega} \epsilon(\theta)}, \tag{3.9}$$

where $\frac{d\sigma}{d\Omega}$ is the differential cross section and $A(\theta)$ is the modeled parity-violated asymmetry as function of the lab-frame scattering angle [70]. The acceptance function is generated through simulation to match the observed data. This section discusses the simulation tools used for optics. The comparisons will be limited to PREX-II i.e., 1 GeV data.

[2]For CREX, ^{48}Ca

3.4.1 HRSTrans

HRSTrans is a Monte Carlo program that studies first and second order optics in an idealized framework. Particle trajectories are sampled as vectors in the target phase space and transported through the spectrometer via matrix multiplication (see [66] for the matrices). HRSTrans provides a quick way to study different spectrometer tunes for a given experiment.

HRSTrans provides the transport chain for four configurations, standard (no septum), PREX, CREX and APEX. The standard tune describes the design of the HRS in Hall A [49]. The program uses a natural unit of length so that the transport can be understood in terms of positions, angles and a central reference trajectory. An instance of the class is specified by three quadrupole fields at the bore given in units of inverse length and are fields are specified for any spectrometer momentum setting which allows a direct scaling between tunes by the momentum ratio. One of the first goals of HRSTrans was to reproduce the standard tune which adjusted the quad settings to reproduce both the first order transport matrix and z-dependence of the matrix elements. This is shown in Figure 3.9. Reproducing the standard tune was important for proof of principle.

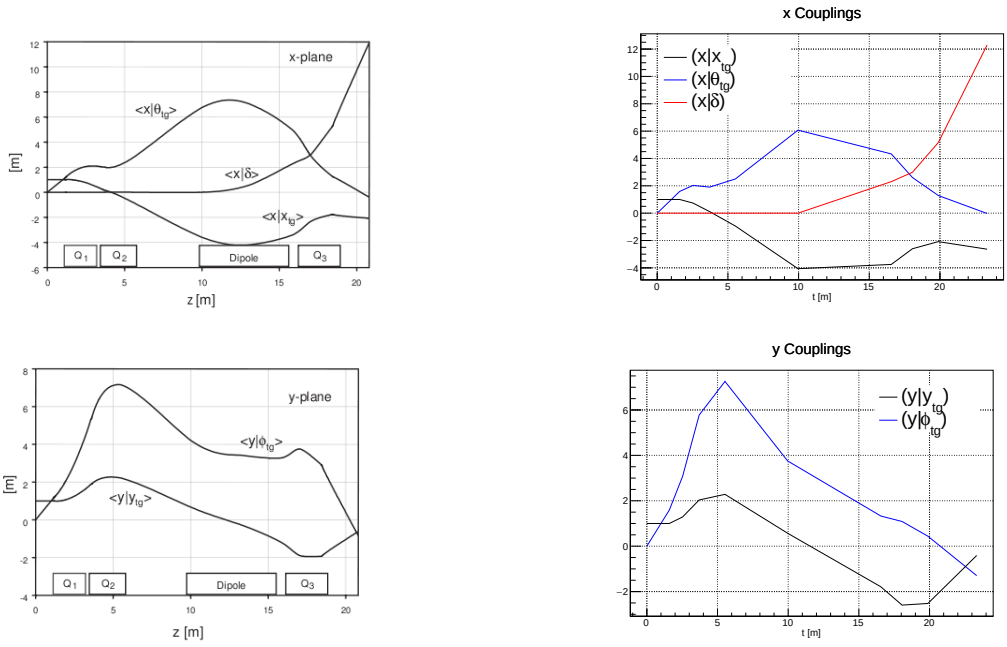

Figure 3.9: Z-dependence of the first order matrix elements for the Standard Tune

The initial PREX transport configuration was designed based on PREX-I, the 2010 run. However, the tune was designed to still minimize $(x|\theta)$ and $(y|\phi)$ matrix elements at the main detectors. The initial optimization provided what was called "Tune B", which is the spectrometer tune PREX-I ran with. PREX-II was different in the fact that the target was moved 10 cm upstream relative to PREX-I. Scaling the quads to account for this didn't result in the optimal tune for PREX-II. PREX-II ran with a relative tune from Tune B called Tune P, which ran 6% low on Q1 and 7% low on Q3 while keeping Q2 the same. Tune P provided the same focusing properties at the main detector that it did for Tune B (figure 3.10) but weaker raster coefficients and dispersion (See Figure 3.11). However, Tune P provided better momentum resolution defined as the ratio of the dispersion over the magnification factor (x raster coefficient).

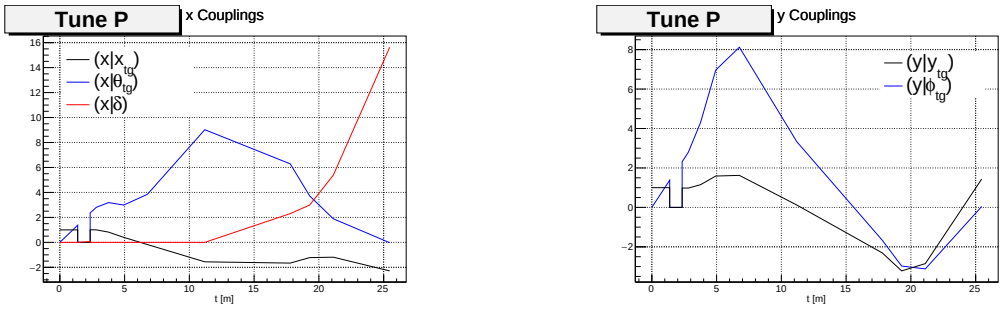

(a) Tune P x Matrix Elements

(b) Tune P y Matrix Elements

Figure 3.10: Z-dependence of the first order matrix elements for Tune P. The blue lines indicating the position due to angle on target intersect the detectors at t$\sim$ 25 at zero.

$$\begin{bmatrix} -2.29 & -0.03 & 0 & 0 & 15.63 \\ -0.25 & -0.44 & 0 & 0 & 2.35 \\ 0 & 0 & 1.44 & 0.04 & -0.34 \\ 0 & 0 & 0.98 & 0.73 & -0.14 \\ 0 & 0 & 0 & 0 & 1 \end{bmatrix}$$

(a) Tune P Matrix

$$\begin{bmatrix} -2.72 & -0.02 & 0 & 0 & 16.47 \\ -0.31 & -0.37 & 0 & 0 & 2.52 \\ 0 & 0 & 1.83 & 0.09 & -0.43 \\ 0 & 0 & 1.02 & 0.59 & -0.17 \\ 0 & 0 & 0 & 0 & 1 \end{bmatrix}$$

(b) Tune B Matrix

Figure 3.11: First order matrix elements for Tune B and Tune P. The nonzero $(y|\delta)$ and $(\phi|\delta)$ matrix elements are due to the septum. The sign depends on the spectrometer(+ for LHRS, - for RHRS). The matrix elements colored in red highlight the differences between the tunes.

3.4.2 G4HRS

3.4.2.1 Overview

G4HRS is a Geant4 ray tracing Monte Carlo program. Electrons are sampled and transported through the spectrometer. The geometry consists of the septa and HRSs(see Figure 3.12). The hits are recorded on virtual planes located at various locations throughout the spectrometer chain. Unlike HRSTrans, G4HRS takes into account initial and final state radiation, energy loss and multiple scattering in the target.

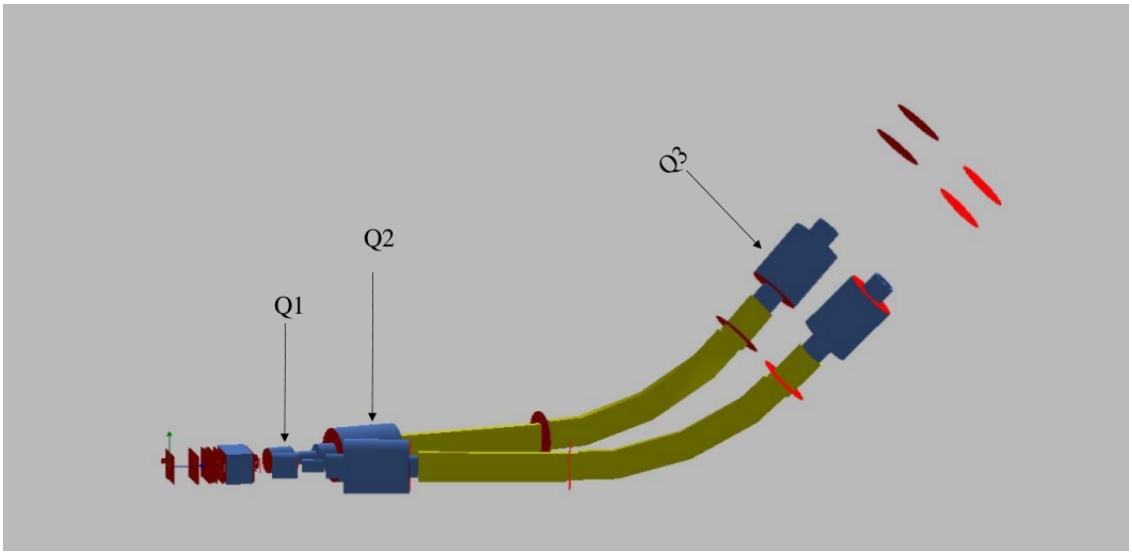

Figure 3.12: Geometry in G4HRS. The square box is the septum, the yellow volume is the dipole volume including the fringe volumes. The red disks are the virtual planes the hits are recorded on.

The septum field is described by a current and momentum scale while the spectrometer magnets are scaled by the momentum only. More explicitly, the septum is given by

$$B'_{xyz} = (\frac{J}{J_0}) \times (\frac{p}{p_0}) \times B_{xyz} \tag{3.10}$$

where B_{xyz} are the field components at current density J_0. B_{xyz} are read in from a TOSCA file and were produced at $J_0 = -1320A/cm^2$. The fields for the spectrometer magnets are scaled by

$$(B^i_o)' = (\frac{p}{p_0}) \times B^i_o, \quad i = Q1, Q2, D, Q3. \tag{3.11}$$

The momentum scale p_0 was chosen to be 1 GeV. The dipole field is described by a analytic function (written by J. LeRose) while the quadrupole fields are explicitly defined at the poletip field b and aperture radius R as given by Equation 3.12.

$$\mathbf{B_i} = \{(\frac{b_i}{R_i})(\frac{P}{1GeV})y, (\frac{b_i}{R_i})(\frac{P}{1GeV})x, 0\} \tag{3.12}$$

i.e., there are no fringe fields and the indices i go from 1 to 3. The momen-

tum P was set to the ideal momentum settings of the recoil central ray, given the exact beam momentum.

3.4.2.2 G4HRS Magnet Tune

Similar to HRSTrans, the spectrometer is tuned to meet the PREX/CREX design optics. This first involves defining the central ray and then a quad tune. Defining the central ray consists of two parts: (1) finding the septum current density J such that the central ray goes through the center of Q1 and is normally incident onthe Q1 face and (2) varying the dipole field to have the central ray normally incidence on Q3 and through its center. Once the central ray is established, the quadrupole fields b_i are optimized to minimize $(x|\theta)$ and $(y|\phi)$ matrix elements at the detector plane. The quadrupole tune involves sampling constant vectors in theta and phi at the target and projecting those to x and y at the detector plane. The points are fit to quadratics and the linear coefficients are optimized to satisfy the optics requirement.

3.5 Acceptance Function

This section discusses how the acceptance function and its systematic uncertainty for PREX-II was determined. The acceptance function is generated in G4HRS.

The integrating measurement encodes the vertex kinematics which sees radiated and multiple scattered beam however, what the detector measures has been additionally radiated and multiple scattered as it passes through the target. Our snapshot of the kinematics as it leaves the target come from counting mode measurements. What is measured in counting mode are the event by event angles, momentum and Q^2, after scattering. These kinematic quantities are known as "apparent" quantities. In reality, because our counting mode measurements have no access to vertex information, we rely on the simulation. As an example, there can be smaller angle events that multiple scatter in the acceptance that is not identified with counting mode measurements.

However, for theorists to interpret our measurements, requires computing what is called the "elemental" asymmetry, where we can think of the scattering as point-like scattering for a fixed beam energy over the accepted angles. Simply stated, for a given model, theorists compute the asymmetry for a fixed beam energy over a range of scattering angles so that equation 3.9 is applicable. To use equation 3.9 involves integrating over the acceptance function which includes vertex scattering angles. The simulation is used to correct the

measurement corresponding to a change in the asymmetry from measuring with a monoenergetic beam i.e.,

$$\langle A_e \rangle = A_m R_{radcor}, \quad R_{radcor} \equiv \frac{\langle A_e^s \rangle}{\langle A_v^s \rangle} \tag{3.13}$$

where A_m is the measured asymmetry, the superscript s refers to simulation and the subscripts e and v are for the elemental and vertex quantities respectively [71]. R_{radcor} is the pre-vertex radiative correction.

Benchmarking $\epsilon(\theta)$ involves comparing the apparent kinematic quantities between data and simulation. The relevant quantities are the asymmetry, lab-scattering polar angle, the momentum and Q^2. Evaluating the uncertainty in the acceptance function involves simulating models that can cause variations in the acceptance. The models include varying the Q1 collimator position, target position and pinch point positions for various septum currents and quantifying the relative differences between the data and simulation.

3.5.1 Angular acceptance

The septum current in G4HRS is tuned to match the central ray of the experiment. To verify the edges of the acceptance, an inner collimator edge search was done in the simulation to see which holes blinked in and out of the acceptance by changing the septum current. The sieve pattern in simulation was compared to the data as shown in Figure 3.13.

The correspondence between data and simulation is pretty good aside from a few marginal differences. The simulation shows two holes that seem attenuated at the second to last column on the outermost edge and a hole on the innermost edge in the center row (see Figure 3.14). We explored the difference between the data and simulation by looking at the sieve holes patterns through various parts of the spectrometer in the simulation. The simulation showed that the sieve holes highlighted in blue in the Figure 3.14 were lost in the spectrometer at Q1 or Q2 (Figure 3.15).

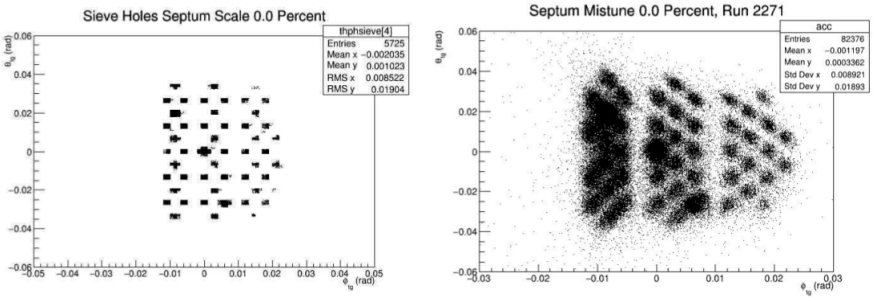

(a) LHRS

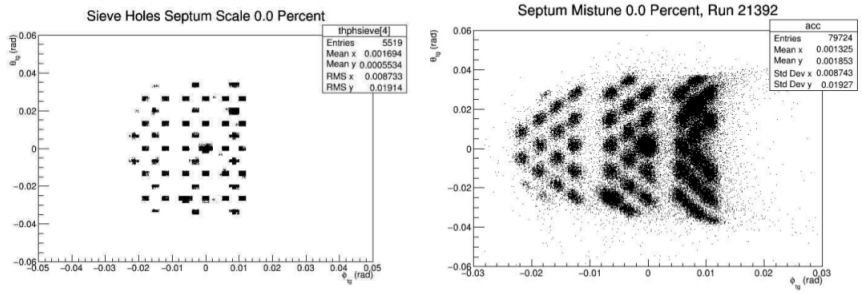

(b) RHRS

Figure 3.13: Sieve pattern comparison between data (right hand side) and simulation (left). For the LHRS, beam center is toward negative phi. Beam center is toward positive phi for RHRS

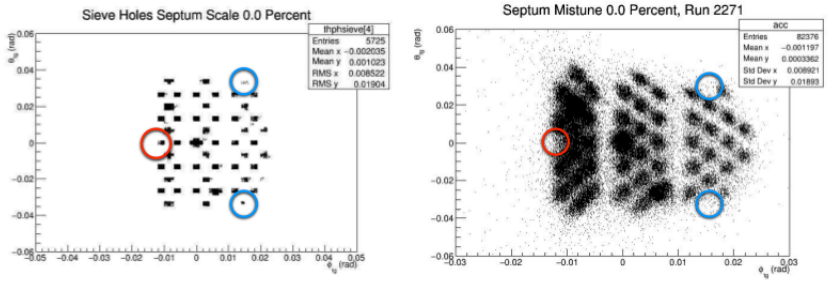

Figure 3.14: LHRS Sieve Patterns isolating the difference between data and simulation. Figure taken from [71]

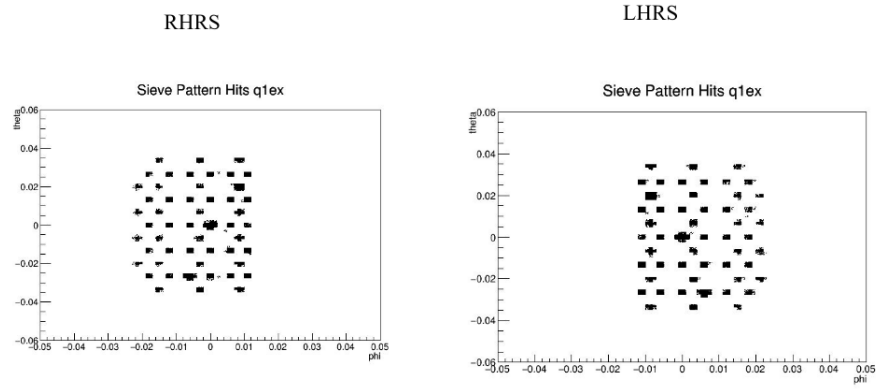

(a) Accepted sieve pattern at the Q1 exit

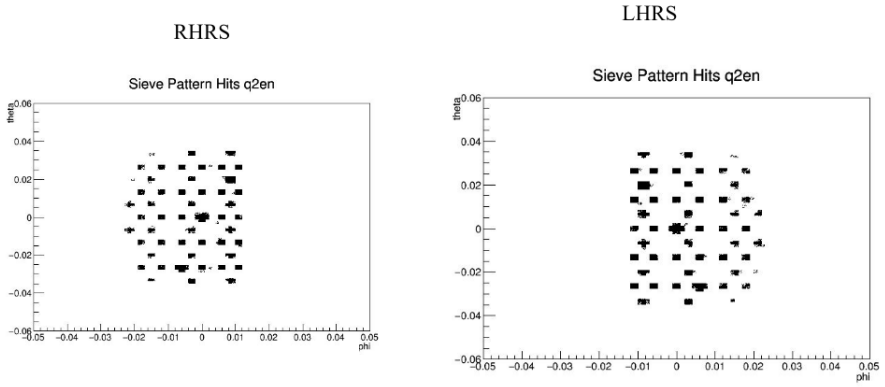

(b) Accepted sieve pattern at the Q2 entrance

Figure 3.15: The two holes at the top/bottom in the third to last column get attenuated between the Q1 exit and Q2 entrance.

Figure 3.15a shows the sieve pattern that make it through the Q1 collimator and Q1 exit while 3.15b shows the pattern that makes it the Q2 entrance. The holes on the third outermost edge get partly attenuated somewhere in the spectrometer [72]. To see where the innermost hole comes to focus, we simulated a fine tune septum scan from ± 2% on the nominal field strength in 0.5% steps. The scan shows that the innermost holes come into focus when the septum current is scaled down -1% from nominal while the holes at the top and bottom of the outermost edge are lost as you increase the current(Figure 3.16). The innermost hole in the center row probably gets lost somewhere in septum or Q1 [73]. The effect of the missing holes on the polar angle, Q^2 and the asymmetry relative to the nominal configuration is summarized in Table

3.1.

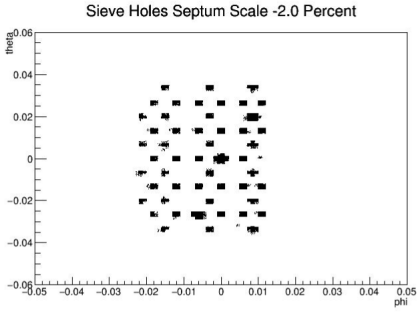

(a) -2% from Nominal

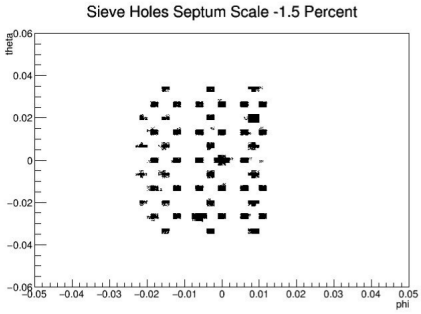

(b) -1.5% from Nominal

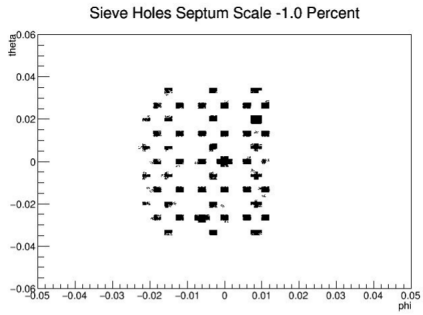

(c) -1% from Nominal

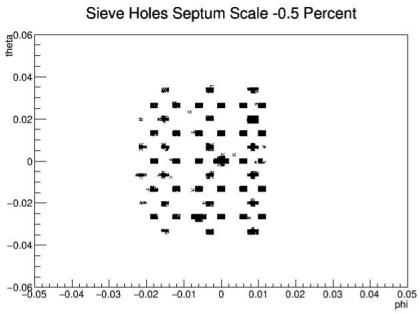

(d) -0.5% from Nominal

Figure 3.16: RHRS Septum scan from -2% up to -0.5% detuned from nominal. The innermost hole in the center row begins to show up at -1% from nominal. It is the same for the LHRS septum scan as well.

	$\theta_{lab}(deg)$	$Q^2 GeV^{-2}$	$A_{PV}(ppb)$
No hole	4.778	0.006364	576.7
Inner hole	4.783 (+0.1%)	0.006377 (+0.2%)	577.5 (+0.14%)
Outer holes	4.769 (-0.19%)	0.006338 (-0.4%)	575.5 (-0.21%)

Table 3.1: The variation in the apparent quantities with the missing hole cuts are within 0.5% level with respect no cut configuration

3.5.1.1 Target Position

As mentioned previously, various factors can limit the angular acceptance. One such factor is the target position. The cryotarget is on a long lever arm which was not surveyed or viewed after pulling vacuum or cooldown [71]. As a result, the target may have moved a few millimeters from its nominal position. We scanned the target position in the simulation, by moving it 5mm upstream and downstream relative to the nominal target position. For each target position, the simulated septum current was varied by $\pm$ 2% from the nominal current. The relative change in the apparent quantities was compared to the data. Figure 3.17 shows an observed 0.5% change in the lab scattering angle and the apparent asymmetry between for the upstream and downstream target position simulations at a fixed septum current, while Table 3.2 shows that changing the septum current to match the lab scattering angle to the data, the apparent asymmetry matched as well.

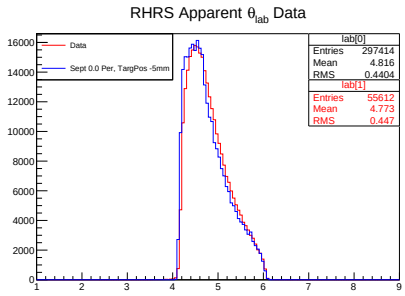

(a) Lab Angle, 5mm Upstream

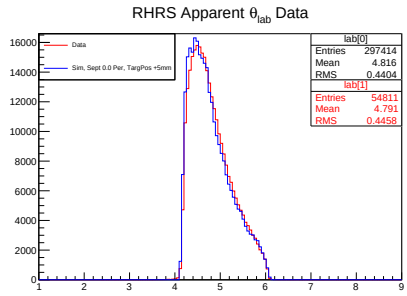

(b) Lab angle, 5mm Downstream

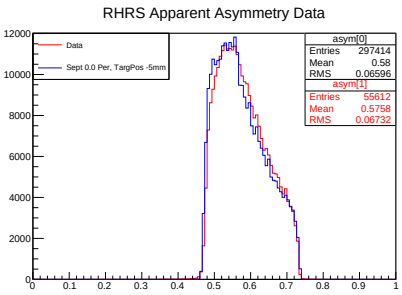

(c) Apparent Asymmetry, 5mm Upstream

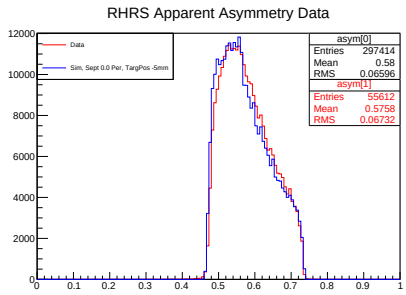

(d) Apparent Asymmetry, 5mm Downstream

Figure 3.17: RHRS polar angle and apparent asymmetry comparison between data and simulation for the target position. The relative changes are 0.5% level with the position shift. The data run is run 21185

(a) Downstream Scan

Target +5mm	$\frac{\theta_{sim}}{\theta_{dat}}$	$\frac{Q^2_{sim}}{Q^2_{dat}}$	$\frac{A_{sim}}{A_{dat}}$
Septum -2%	100.30%	101.17%	100.95%
Septum -1%	99.96%	100.486%	100.52%
Septum 0%	99.50%	99.54%	99.96%
Septum +1%	99.03%	98.60%	99.38%
Septum +2%	98.89%	98.32%	99.20%

(b) Upstream Scan

Target -5mm	$\frac{\theta_{sim}}{\theta_{dat}}$	$\frac{Q^2_{sim}}{Q^2_{dat}}$	$\frac{A_{sim}}{A_{dat}}$
Septum -2%	99.91%	100.38%	100.45%
Septum -1%	99.52%	99.60%	99.97%
Septum 0%	99.11%	98.78%	99.45%
Septum +1%	98.73%	98.00%	98.96%
Septum +2%	98.39%	97.33%	98.54%

Table 3.2: Septum scan for the upstream and downstream target positions. The comparison to data is done for Run 21185

3.5.1.2 Pinch Point

The pinch point is another factor that can limit the acceptance. The pinch point is defined as the closest approach between the septum's acceptance box to its coils at the septum entrance. A top view of pinch point is shown in Figure 3.18. The vacuum boxes are positioned by flanges which during installation were found to be slightly out of design specifications. As a result, the vacuum box could vary from ideal by as much as 3 mm [71]. In simulation, the acceptance path through the septum is modeled by virtual planes at various locations [74]. We performed a pinch scan to see its effect on the apparent quantities (see Figure 3.19).

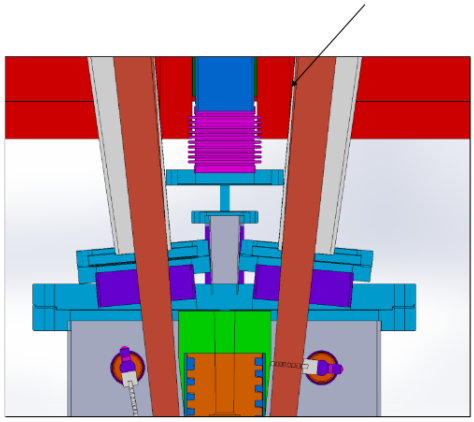

Figure 3.18: CAD of the pinch point (see arrow). The septum vacuum box is in gray and the septum coils are shown in bright red. The nominal accepted track envelopes are shown in red-brown. Figure from [75]

fig:Pinch

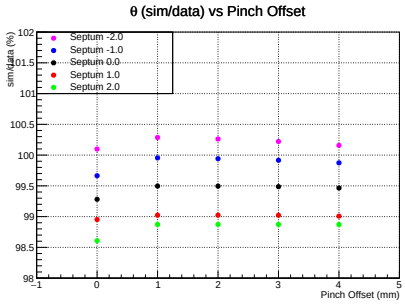

(a) Lab Theta vs. Pinch offset

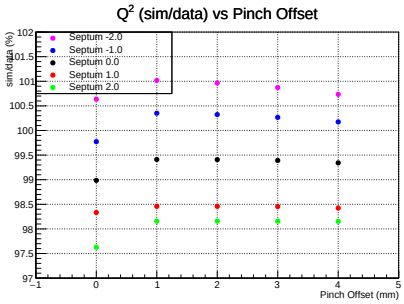

(b) Q^2 vs. Pinch offset

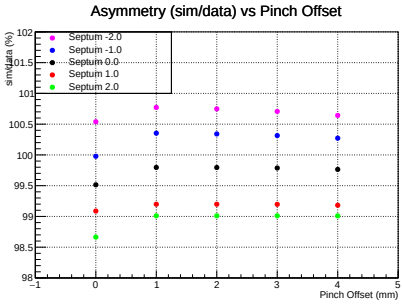

(c) Asymmetry vs. Pinch offset

Figure 3.19: RHRS pinch scan. The angle changes are at the level of 0.3% while the asymmetry changes are at the 0.5% level. Q^2 changes at the 1% level. These changes are for a fixed septum current.

3.5.1.3 Collimator Offset

The acceptance can also change if the Q1 collimator is in the wrong place. Any horizontal offset of the collimator position from ideal would change the lab scattering angle. A systematic study changing the collimator offset was done using the simulation. The coordinates of the Q1 collimator virtual plane in G4HRS was fixed to match the surveyed position in reality. Using a c++ function that modeled the collimator shape that was built, we offset the collimator horizontally and scanned the position at different septum currents [58]. The lab scattering angle and the asymmetry varied roughly at the 0.5% percent level for different collimator offsets for a given septum current, while Q^2 varied at the percent level (Figure 3.20).

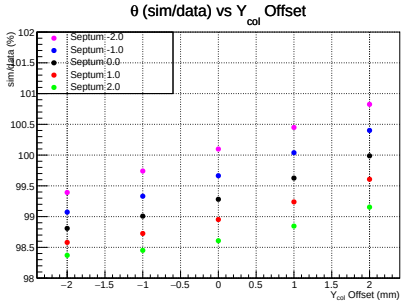

(a) Lab Theta vs. Y_{col} offset

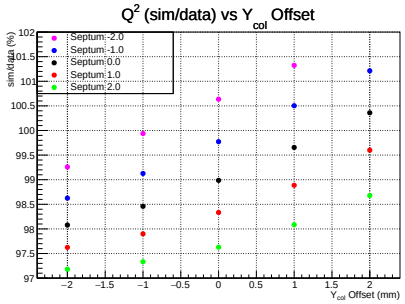

(b) Q^2 vs. Y_{col} offset

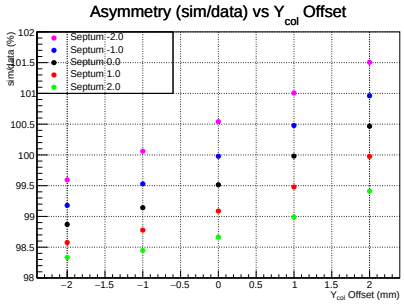

(c) Asymmetry vs. Y_{col} offset

Figure 3.20: RHRS collimator scan. Negative offset corresponds to away from beam center (x = 0) while positive is toward the beam center

3.5.1.4 Vertex Correction

The vertex correction is the implied difference between the apparent asymmetry and the vertex asymmetry. The vertex kinematics were extracted from the simulation. An example of the comparison between vertex and apparent distributions is shown in Figure 3.21. The vertex asymmetry only accounts for events that scatter off the lead target. The vertex distributions include smaller scattering angles due to multiple scattering that aren't seen in the apparent distributions. The relative difference between the vertex and apparent asymmetry is (3.7 ± 0.30) % for simulated configurations. The uncertainty was obtained by considering the simulation models that matched the apparent distributions well and look at the range of the vertex asymmetry. The vertex asymmetry for those scans agreed within 0.3%.

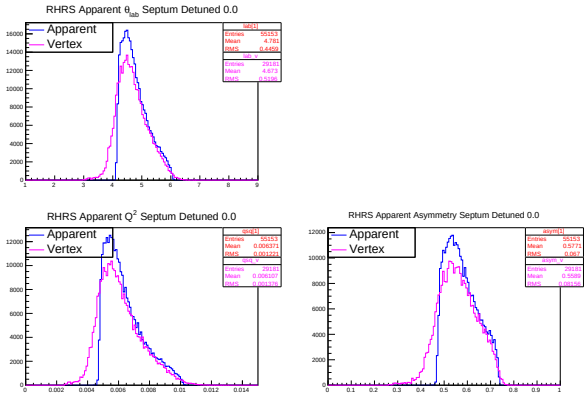

Figure 3.21: RHRS vertex and apparent kinematics from simulation. The vertex distributions only include events that scatter off lead while the apparent distributions consider all scattered events (both diamond and lead)

3.5.2 Momentum Acceptance

The main detectors define the momentum acceptance for the experiment. To see where the momentum is cutoff, we identify the location of the quartz edge in the dispersive plane. To identify the quartz edge, one looks at the tracks that are above and below an ADC threshold of the pulse height spectrum. For the simulation, we mimic the geometric cut by using a combined cut which includes momentum and target theta.

Different target theta show up at different x at the detector for the same momentum. Because of the nonzero coupling between the momentum and theta, they are correlated. We can use a correlated cut to mimic the geometric cut at the quartz edge [76] as shown in Figure 3.22. The correlated cut is what was used in the simulation and the previous analysis outlined in section 3.5.1.

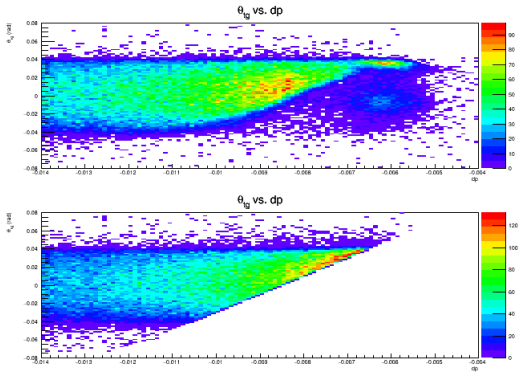

Figure 3.22: Theta and dp correlation. The top plot has an ADC cut in data while the bottom has the correlated theta/dp cut in simulation. Note one can observe a triangular "edge" of the acceptance in both plots.

3.5.3 Systematics Summary

The relative uncertainties on A_{PV} from the acceptance model is summarized in Table 3.2. The uncertainties in the acceptance function mismatch was determined by considering all the simulation scans for every configuration, picking the scans that best matched the apparent kinematics quantities. From those scans, the range of the vertex asymmetry was extracted from simulation. The vertex asymmetries for those configurations agreed at the 0.3% level. This suggests that even that we can reproduce the vertex asymmetry even if the acceptance function is not exactly correct, provided that apparent polar angle and Q^2 match. Finally, the quadrature sum of the uncertainties gives a 0.6% relative error on A_{PV}.

	Value	Uncertainty	$\frac{\delta A_{PV}}{A_{PV}}$
Apparent Acceptance Mismatch		0.3-0.5%	0.5%
Vertex kinematics correction	3.70%	0.3%	0.3%
Radiative correction A_e vs A_v	0.10%	0.1%	0.01%
total			0.6%

Table 3.3: Table of the systematics associated with the acceptance function. The dominant error is from the apparent acceptance mismatch

Chapter 4

PREX-II A_T Analysis

PREX-II performed A_T measurements on three isoscalar targets highlighted by the first measurement on an intermediate Z nucleus, ^{40}Ca. The ^{40}Ca measurement is interesting as it provides additional input on the $\frac{A}{Z}$ dependence of the analyzing power as given by equation 1.28. The other measurements were done on ^{12}C and ^{208}Pb. The A_T measurement on the ^{208}Pb was done as an nonzero analyzing power can contribute to the systematic error for PREX-II. The ^{12}C measurement was done since the lead targets are sandwiched between two diamond foils. Its contamination needs to be subtracted out to extract the ^{208}Pb result. This chapter addresses the analyses of the transverse data for PREX-II.

The goal was to measure A_T to better than 5%. Using 6 ppm magnitude asymmetry for ^{12}C A_T means that we planned to measure A_T to better than 0.3 ppm precision. Assuming that the ^{40}Ca should match the ^{12}C at the same Q^2 means that we want to also measure the ^{40}Ca A_T to better than 0.3 ppm precision. For ^{208}Pb, the expectation was to measure A_T to significantly below 0.3 ppm. To achieve the proposed statistical precision, the run plan was to take data on the ^{12}C, ^{208}Pb and ^{40}Ca for 2 hours, 4 hours and an hour respectively.

4.1 Asymmetry Data

The raw asymmetry for the detectors is calculated as the fractional difference between the detector signals $D^{+,-}$, in different helicity states normalized to the beam current $I^{+,-}$ in those states

$$A_{raw} = \frac{\frac{D^+}{I^+} - \frac{D^-}{I^-}}{\frac{D^+}{I^+} + \frac{D^-}{I^-}}. \tag{4.1}$$

The PREX-II transverse data ran with a 240 Hz helicity flip rate in an octet randomized helicity pattern with the initial helicity state being chosen pseudorandomly. The multiplet asymmetries were calculated by averaging the signals in the same helicity states using Equation 4.1. About 10000 multiplets form what is called a minirun. A collection of about 2-5 miniruns form a run. A collection of runs taken with or without half wave plate inserted form a slug. The carbon and lead data sets had four slugs of data while the calcium-40 data set had two (5 runs, 11 miniruns). The carbon data set consisted of seven runs (20 miniruns) while lead consisted of 13 runs (53 miniruns). To extract the correct asymmetry value, the runs without the half wave plate have their asymmetry values sign corrected i.e., multiplied by -1.

The left and right spectrometers measure the asymmetry with opposite sign due to the fact the vector normal to the scattering plane changes sign (see Equation 1.19). As a result, the main A_T measurement is given by the so-called double difference between the asymmetries in the left and right spectrometers. The ^{40}Ca raw double difference is plotted in Figure 4.1 as an example, while the raw asymmetry values in ppb are given in Table 4.1. The ^{12}C and ^{208}Pb asymmetry plots are shown in Section A.2 of Appendix A.

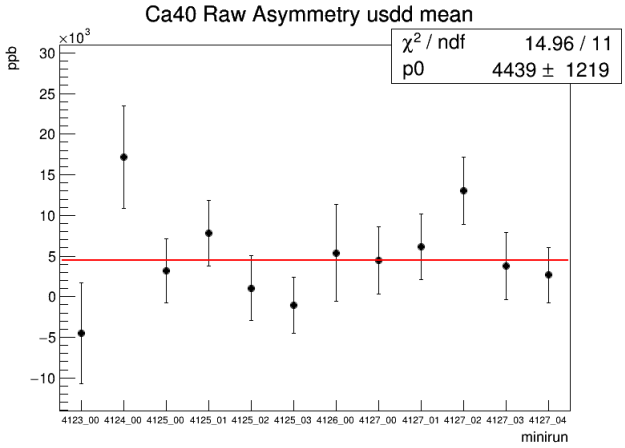

Figure 4.1: Raw ^{40}Ca A_T measurement plotted vs minirun given in ppb

	A^m_{C12}	A^m_{Pb}	A^m_{Ca40}
Raw Left	5041 ± 860.4	-783 ± 797	3272 ± 2354
Raw Right	-5437 ± 837	-579 ± 693	-5079 ± 1753
Raw Double Diff.	5268 ± 741	-196 ± 672	4439 ± 1219

Table 4.1: Tabulated Raw Asymmetries for the Left/Right Main Detectors and the Double Differences for ^{12}C, ^{208}Pb and ^{40}Ca given in ppb.

As mentioned in section 2.3, to extract the physics asymmetry, the asymmetry needs to be corrected for any helicity-correlated beam asymmetries (HBCAs) which was given by equation 2.3.

4.1.1 Charge Asymmetry

The charge asymmetry A_I arises in the electron source due to birefrigent elements downstream of the Pockels cell such as the vacuum window (see Figure 2.2) and imperfect alignment of the Pockels cell. The birefringence introduces residual linearly polarized laser light, which has opposing orientations between helicity states. Since the helicity states had their linear components oriented differently, they are transmitted differently, resulting in a nonzero charge asymmetry. This is known as the Polarized Intensity Transport Asymmetry (PITA) effect [77]. The PITA effect is minimized by the feedback loop described in Chapter 2.3. The Pockels cell high voltages get corrected by measuring the PITA slope which describes the relationship between the A_I and the corrected voltage (PITA scan) [78]. A PITA scan was performed before the transverse running. The charge asymmetry was less than 200 ppb for all three targets as shown in Table 4.2. The A_I figures are shown in Appendix A.2.1.

	^{12}C	^{208}Pb	^{40}Ca
A_I	-35 ± 1148	-173 ± 1188	128 ± 430

Table 4.2: Sign corrected charge asymmetry for all targets in units of ppb

4.1.2 Beam False Asymmetry

The other source of HCBAs is from beam fluctuations in position, angle, and energy. As discussed in Section 2.3, the detector rates are sensitive to any beam fluctuations. Helicity-correlated fluctuations introduces a beam false asymmetry (see third term in equation 2.3). The beam false asymmetries were extracted using two techniques, linear regression and dithering.

Regression

Regression is a technique that uses the natural beam motion to remove any HCBAs. It gets it name from the fact the slopes are calculated using χ^2 minimization. For a one parameter regression, the slope is calculated as [79]

$$b = \frac{\sum_i (y_i - < y >)(x_i - < x >)}{\sum_i (x_i - < x >)^2} \tag{4.2}$$

where y is the dependent variable and x is the independent variable. The dependent variable gets regressed by removing the calculated sensitivity to the dependent variable i.e., $y_i^{reg} = y_i - bx_i$. Multiparameter regression diagonalizes the covariance matrix, simultaneously regressing in all dimensions.

Dithering

The other method to extract slopes is using dithering. Dithering calibrates the detector response using the beam modulation system described in Chapter 2. By modulating the voltage applied to the coils sinusoidally, the DAQ measures the response in the BPMs and detectors along different points in the sinousoid. More specifically, what we measure are the BPMs and detectors' response to changes in the coils i.e, $\frac{\partial D}{\partial C_j}$ and $\frac{\partial x_i}{\partial C_j}$. To extract the slopes from the detector response, we note that

$$\frac{\partial D}{\partial x_i} = (\frac{\partial x_i}{\partial C_j})^{-1} \frac{\partial D}{\partial C_j} \tag{4.3}$$

where the expression in parenthesis is known as the dithering matrix [1].

The dithering matrix defines the monitor response due to a change in coil behavior. For each detector, the dithering matrix equation is solved for the slopes. The regressed and dither corrected asymmetries (ppb) are tabulated in Table 4.3.

	$A_{dit,L}$	$A_{reg,L}$	$A_{dit,R}$	$A_{reg,R}$	$A_{dit,dd}$	$A_{reg,dd}$
C12	5651 ± 473	5627 ± 472	-5326 ± 463	-5290 ± 462	5494 ± 330	5464 ± 330
Pb208	-208 ± 185	-238 ± 183	-197 ± 180	-239 ± 177	0 ± 129	0 ± 127
Ca40	5410 ± 482	5105 ± 442	-5226 ± 446	-5479 ± 413	5295 ± 290	5276 ± 288

Table 4.3: Regression and Dither Corrected asymmetries for Left/Right main detector and the double difference in ppb

The beam corrections for the double difference were dominated by horizontal position beam fluctuations with the largest slopes on the order of 30 ppb/nm for ^{12}C, 35 ppb/nm ^{40}Ca and 50 ppb/nm for the ^{208}Pb (see Table 4.3). Fluctuations in the horizontal beam position changes the acceptance in both arms in opposite ways while fluctuations in the vertical beam position and energy largely cancel in the double difference (see Table 4.4). The dithering results will be used for subsequent analysis. For the energy modulation, an effective BPM was used called BPM E, a linear combination of 11 and 12X. The uncertainty in the beam correction is discussed in Section 4.2.6.

(a) A_T Run Pd 1

	^{12}C	^{208}Pb	^{40}Ca
c_{4aX}	-8.95	-18.35	-14.25
c_{4eX}	29.45	47.5	37.0
c_{4aY}	-0.7	-1.05	-0.4
c_{4eY}	1.35	7.95	-1.5
c_E	-3.55	-2.8	2.4

(b) A_T Run Pd 2

	^{12}C	^{208}Pb
c_{4aX}	-10.1	24.3
c_{4eX}	29.15	23.85
c_{4aY}	17.95	0.7
c_{4eY}	0.1	-1.15
c_E	-3.8	-6.15

Table 4.4: Dithering slopes for the double difference for each target. The units are given in ppb/nm. The variation between the slopes are at the 5% level

4.1.3 Asymmetry Sign

It is important to determine what settings gave vertical spin up or down in the Hall and correlate that to helicity windows measured by the parity DAQ.

(a) A_T Run Pd 1

	^{12}C	^{208}Pb	^{40}Ca
$< 4aX >$	-5.3	3.2	-1.6
$< 4eX >$	-29.6	21.8	-22.9
$< 4aY >$	22.4	6.1	5.0
$< 4eY >$	13.6	2.3	2.2
$< E >$	-17.4	-17.8	2.9

(b) A_T Run Pd 2

	^{12}C	^{208}Pb
$< 4aX >$	-5.6	-1.4
$< 4eX >$	9.3	-56.2
$< 4aY >$	-22.5	15.2
$< 4eY >$	-14.2	19.6
$< E >$	-23.5	3.1

Table 4.5: The position differences for the different run periods on various targets given in nanometers.

Since the transverse measurements use the polarization from the Møller measurements, the sign of the longitudinal polarization was taken from the Møller polarimeter. Using the Møller measurements taken before PREX-II transverse running, longitudinal polarization was positive for IHWP out and negative for IHWP in [80, 81]. This means the asymmetry was calculated relative to the sign of the polarization. From calibration data taken after transverse running, the Møller and parity DAQs measured asymmetries with the same sign [82].

The sign of the asymmetry is tied to the scalar product of the electron spin and the cross product of the incoming and outgoing electron momentum (Eq 1.19). For the vertical up transverse case, this is positive for the LHRS. For PREX-II, the measured asymmetry for IHWP out state was positive and corresponded to vertical down since we sign correct for this state. This means that the LHRS measures a negative asymmetry while the RHRS measures a positive asymmetry [83].

4.2 A_n Extraction and Systematic Errors

After correcting for the HCBAs, we need to account for other background processes. The integrated signal can be separated into an elastic part and the sum of all background signals [48]

$$S = S_E + \sum_i S_B^i. \tag{4.4}$$

Following the derivation in [48], the corrected asymmetry can then be calculated as the fractional difference between + and - helicity states

$$
\begin{aligned}
A_{corr} =& \frac{S^+ - S^-}{S^+ + S^-} = \frac{(S_E^+ - S_E^-) + \sum_i (S_B^{+i} - S_B^{-i})}{(S_E^+ + S_E^-) + \sum_i (S_B^{+i} + S_B^{-i})} \\
&= \frac{S_E^+ - S_E^-}{(S_E^+ + S_E^-) + \sum_i (S_B^{+i} + S_B^{-i})} + \frac{\sum_i S_B^{+i} + S_B^{-i}}{(S_E^+ + S_E^-) + \sum_i (S_B^{+i} + S_B^{-i})} \\
&= \frac{S_E^+ - S_E^-}{S_E^+ + S_E^-} \frac{1}{1 + \frac{\sum_i S_B^{+i} + S_B^{-i}}{S_E^+ + S_E^-}} + \sum_i \frac{S_B^{+i} - S_B^{-i}}{S_B^{+i} + S_B^{-i}} \frac{1}{1 + \frac{S_E^+ + S_E^-}{S_B^{+i} + S_B^{-i}}} \\
&= A_E \frac{S_E^+ + S_E^-}{S_E^+ + S_E^- + \sum_i S_B^{+i} + S_B^{-i}} + \sum_i A_{Bi} \frac{\sum_i S_B^{+i} + S_B^{-i}}{S_E^+ + S_E^- + \sum_i S_B^{+i} + S_B^{-i}} \\
&= A_E (1 - \sum_i f_i) + \sum_i f_i A_{Bi}
\end{aligned}
\tag{4.5}
$$

where f_i are known as the dilution factors. The dilution factors are the fraction of each kind of background asymmetry (A_{Bi}). Isolating the elastic asymmetry, equation 4.5 becomes

$$
A_E = \frac{A_{corr} - \sum_i f_i A_{Bi}}{1 - \sum_i f_i} \sim (1 + \sum_i f_i) A_{corr} - \sum_i f_i A_{Bi} \tag{4.6}
$$

where it has been assumed f_i is much less than 1 [48]. Furthermore, the extracted asymmetry A_E must be corrected for both the beam polarization and finite acceptance so that A_n is given by

$$
A_n = \frac{(1 + \sum_i f_i) A_{corr} - \sum_i f_i A_{Bi}}{P \langle \cos \phi \rangle}. \tag{4.7}
$$

Equation 4.7 is the basis for all subsequent analysis.

4.2.1 $\langle \cos \phi \rangle$ Analysis

The A_n extraction requires a $\langle \cos \phi \rangle$ correction to account for the fact that the spectrometer acceptance is not strictly confined in the horizontal plane. However, it is confined enough horizontally, that the correction is small. To quantify this, we use the low current Q^2 tracking data. Here the azimuth is defined relative the vertical axis (see Figure 4.2).

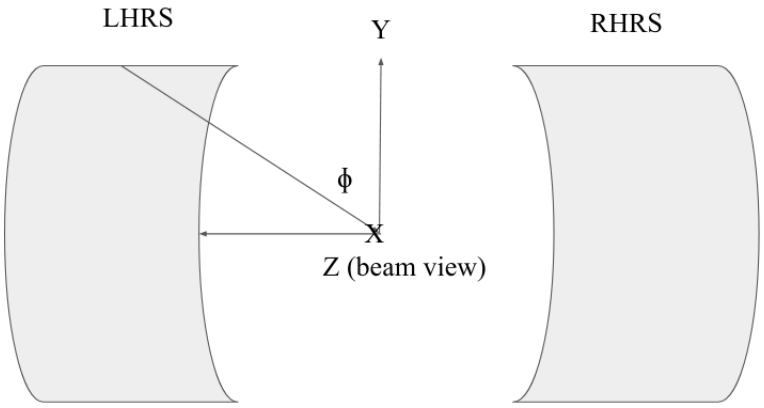

Figure 4.2: Beam view of the azimuth. The kidney shaped drawings are the Q1 collimators. Here ϕ is defined relative to the vertical.

The azimuth can be expressed directly in terms of the transport coordinates as

$$\cos\phi = \frac{\pm\theta_{tg}}{\sqrt{\theta_{tg}^2 + \sin^2\theta_o \pm 2\tan\theta_o\phi_{tg} + \frac{\phi_{tg}^2}{\cos^2\theta_o}}} \tag{4.8}$$

$$\sin\phi = \frac{\sec\theta_o(\phi_{tg} + \sin\theta_o\cos\theta_o)}{\sqrt{\theta_{tg}^2 + \sin^2\theta_o \pm 2\tan\theta_o\phi_{tg} + \frac{\phi_{tg}^2}{\cos^2\theta_o}}} \tag{4.9}$$

where θ_o is the central angle and the $\pm$ sign in equation 4.7 are for the LHRS and RHRS respectively. The central angle θ_o is 4.78^o for the LHRS and -4.762^o for the RHRS. The $\langle\cos\phi\rangle$ histograms for ^{40}Ca are shown in Figure 4.3 (see Appendix B for other targets). For the measurement, the central values were averaged for the left and right arms (Table 4.6).

	LHRS $\langle \cos\phi \rangle$	RHRS $\langle \cos\phi \rangle$	Avg $\langle \cos\phi \rangle$
C12	0.967	0.967	0.967
Pb208	0.966	0.966	0.966
Ca40	0.964	0.964	0.964

Table 4.6: Tabulated $\langle \cos\phi \rangle$ values. The lead A_T data was taken on two different ^{208}Pb targets. The ^{208}Pb acceptance correction was taken by averaging the two runs from the LHRS and two runs from the RHRS.

The cuts for the $\langle \cos\phi \rangle$ analysis were the same cuts that were used for the Q^2 analysis. The schematic for a Q^2 measurement is shown in Figure 4.4. The first cut was a cluster cut on each VDC plane. A cluster is a group of hits with consecutive wire numbers. We used a single cluster cut to remove any tracking inefficiencies. The S0 scintillator as the main trigger so we selected tracks that hit the main detector that were triggered by the S0 scintillator. The electrons that hit the detector produced a signal which was output from the ADC (see Figure 4.5). The pulse-height distribution includes both the pedestal and signal so we cut on the ADC value above pedestal to ensure that we pick the events that hit the main detector.

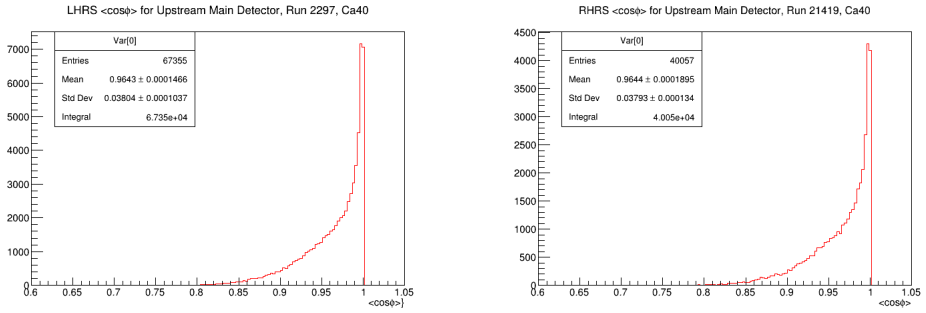

(a) LHRS Ca40 (b) RHRS Ca40

Figure 4.3: ^{40}Ca $\langle \cos\phi \rangle$ distributions

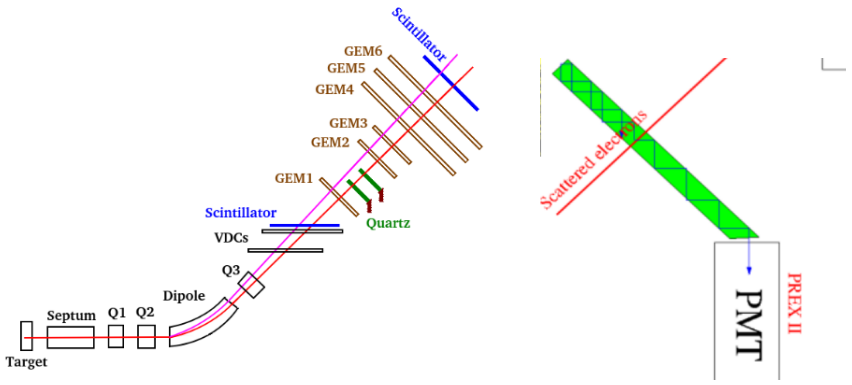

(a) Setup (b) Scattered Flux

Figure 4.4: Schematic of the Q^2 measurement. The events triggered by the S0 scintillator shown in (a) above the VDC hits the quartz detector producing Cherenkov light, which collected by the PMT (b). The signal is sent to an ADC, which is read out during the data replay. Figure a is from [84] and b is from [62]

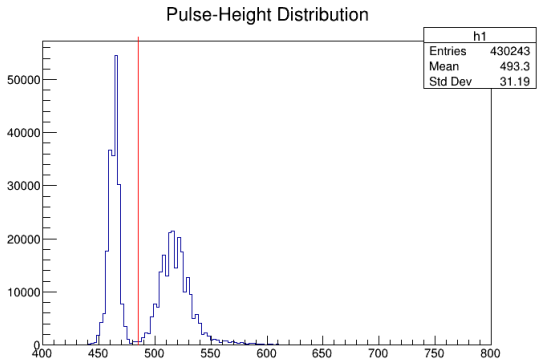

Figure 4.5: Pulse-height spectrum for Run 2292. The red line (at 485) indicates where the cut was made

In addition to ADC cut and trigger cut, we also cut on the target variables, theta, phi and momentum to ensure that the tracks are within the acceptance. The collimator height was 9 cm and roughly located about 2.5 m downstream of the target. The inner and outer edges of the collimator are located at -3.36 and +5.71 cm with respect to the central ray [85]. From these dimensions, we bound the acceptance by

$$\theta_{tg} \sim \frac{x_{height}}{z}, \quad \phi_{tg} \sim \frac{y_{edge}}{z}. \tag{4.10}$$

From equation, we expect θ_{tg} = (-36,36) mrad and $\phi_{tg} = (-14, 24)$ mrad[1]. In the data, we restricted abs(θ_{tg}) to be between 0.08 radians and abs(ϕ_{tg}) to be within 0.05 radians. The momentum cut was determined by identifying the quartz edge in momentum space. This involved drawing two histograms, one that passes the ADC cut(above the red line in Fig 4.5) and one that misses the ADC cut. The intersection of those two histograms defines the quartz edge. The momentum cut was $\delta = (-0.04, 0.002)$ which ensured we were isolating the elastic peak.

4.2.2 Polarization and Carbon Contamination

The ^{12}C and ^{40}Ca targets are isotopically pure while the ^{208}Pb targets were sandwiched between two diamond foils. Equation 4.7 reads

$$A_{n,i} = \frac{A_{E,i}}{P\langle\cos\phi\rangle}, \quad i =^{12} C,^{40} Ca \tag{4.11}$$

$$A_{n,Pb} = \frac{(1 + f_C)A_{corr} - f_C A_{corr,C}}{P\langle\cos\phi\rangle}. \tag{4.12}$$

The variable f_C is the dilution factor associated with the carbon contamination. It is defined as the carbon to lead rate ratio. The dilution faction was extracted from simulation and found to be 6.71±0.57% [86]. The uncertainty in the ratio was obtained by varying the target thickness (both diamond and lead) and the momentum cutoff in simulation. The asymmetries are -6340 ppb for ^{12}C, 430 ppb for ^{208}Pb and -6120 ppb for ^{40}Ca.

The polarization P for the transverse data was inferred from the Møller longitudinal polarization measurements. The Møller polarimeter measured the polarization to be 89.70 ±0.8%. The systematic associated with the beam polarization is given by

$$dA_P = -A_E \frac{dP}{P}. \tag{4.13}$$

The polarization systematic on the final asymmetry is given by 56 ppb for ^{12}C, 3 ppb for ^{208}Pb and 54 ppb for ^{40}Ca.

The lead asymmetry has an additional systematic due to the carbon contamination. The uncertainty consists of two parts given by

[1]This is for LHRS. For RHRS, (-24,14) mrad

$$dA_f^{Pb} = \frac{(A_{corr} - A_{corr,C12})df_C}{P\langle\cos\phi\rangle} \tag{4.14}$$

$$dA_C^{Pb} = \frac{dA_{corr,C12}f_C}{P\langle\cos\phi\rangle}. \tag{4.15}$$

Equation 4.14 originates from the uncertainty in the dilution factor f_C while equation 4.15 comes from the uncertainty in the carbon measurement. Using 0.6% uncertainty in the dilution factor gives a 36 ppb systematic. Using the ^{12}C asymmetry given in Table 4.3, the uncertainty due to the carbon asymmetry is 26 ppb. The combined error due to the carbon contamination is 44 ppb.

4.2.3 Detector Linearity

The main detectors were designed in such a way such that the integrated PMT signal is proportional to the electron flux. However, at certain PMT voltages, the PMT response is nonlinear, which can result in an increase in signal relative to amount of measured photons. This means for a given integrating window, the number of measured photons is given by [1]

$$N_{meas}^{+,-} = N^{+,-}(1 + \beta N^{+,-}) \tag{4.16}$$

where β is the nonlinearity.

The detector nonlinearity was measured both in-situ during the experiment, and on the bench pre- and post- experiment in a way that mimicked running conditions. The bench tests consisted of a PMT facing a pair of LED sources in a black box. One LED served as a baseline, where a constant signal was sent to it , thus producing a constant photon flux measured by the PMT. The other LED was pulsed at 240 Hz, the helicity flip rate for transverse running [87]. In addition, there is a filter wheel with 8 transmission settings in from of the baseline LED which attenuates the baseline signal without changing the pulsed signal. Using the parity DAQ, we can compute the asymmetry between two windows which differ by whether the pulse was sent or not. The asymmetry is given by

$$A_{meas} = A_{true}(1 + \beta\frac{N^+ + N^-}{2}) \tag{4.17}$$

where the positive sign is for a pulsed window and the negative sign is for an unpulsed window. The asymmetries were computed for 20 cycles of different

filter wheel rotation and different high voltage settings [87, 88]. For a linear PMT, the signal difference between pulsed and unpulsed signals should be independent of the filter setting so that the measured asymmetry is the true asymmetry , while a nonlinear PMT will a baseline dependent asymmetry (see Equation 4.16). The measured asymmetry was plotted against high voltage where the slope of the line is β. For the PREX-II transverse running, the PMT nonlinearity was within 0.3% for all three targets [89]. The systematic associated is 0.3% on the raw asymmetry.

The detector nonlinearity was monitored during the run using PITA and current calibration scans. Because the detectors are calibrated using the BCMs, the BCM performance can introduce a systematic effect on the detector non-linearity. The systematic effect comes the detector calibration which uses a beam-based calibration over a 28-80 uA range. The uncertainty in the detector calibration was assigned to be 1% percent. The results from the in-situ and bench tests agreed within 0.5%. Therefore a 0.5% systematic was assigned due to the non-linearity [89, 90]. Correcting for the polarization and finite acceptance, the systematic due to the detector nonlinearity is

$$dA_{det} = 0.5\% \frac{A_{raw}}{P\langle \cos\phi \rangle}. \tag{4.18}$$

The systematic error due to the detector non-linearity is 30 ppb for ^{12}C, 1 ppb for ^{208}Pb and 25 ppb for ^{40}Ca.

4.2.4 BCM Linearity

Given that the asymmetry is normalized to the beam charge, a nonlinear response in the BCM can contribute systematically to the main measurement. The BCM nonlinearity were monitored during the runs via current scans. The BCMs were fit against the Unser BCM to get the BCM pedestals. The nonlinearity was zeroed out but the uncertainty in the BCM calibration i.e., pedestals was assigned to be 1% of the charge asymmetry. Using the charge asymmetries from Table 4.2, the raw charge asymmetry uncertainties are 0.5 ppb for ^{12}C, 1 ppb for ^{208}Pb and 1 ppb for ^{40}Ca. Accounting for the polarization and $\langle \cos\phi \rangle$ acceptance factor, the systematic due to the BCM linearity are 0 ppb, 1 ppb and 1 ppb for ^{12}C, ^{208}Pb and ^{40}Ca respectively.

4.2.5 Q^2

The energy dependence on the transverse asymmetry comes from Q^2. The systematic error due to Q^2 is given by

$$\frac{dA_T}{A_T} = \frac{1}{2}\frac{dQ^2}{Q^2}. \tag{4.19}$$

From the PREX-II A_{PV} analysis, the relative error on Q^2 was 0.65% which implies the error on A_T is 0.325%. From this, the error in the corrected asymmetry is 2 ppb for ^{12}C, 2 ppb for ^{40}Ca and 0 ppb for ^{208}Pb. Correcting for the beam polarization and acceptance $\langle \cos\phi \rangle$, the systematic error in the physics asymmetry A_n due to Q^2 is 2 ppb for ^{12}C, 2 ppb for ^{40}Ca and 0 ppb for ^{208}Pb. The ^{40}Ca Q^2 distributions in Figure 4.6. The ^{208}Pb and ^{12}C Q^2 distributions are shown in Appendix B.

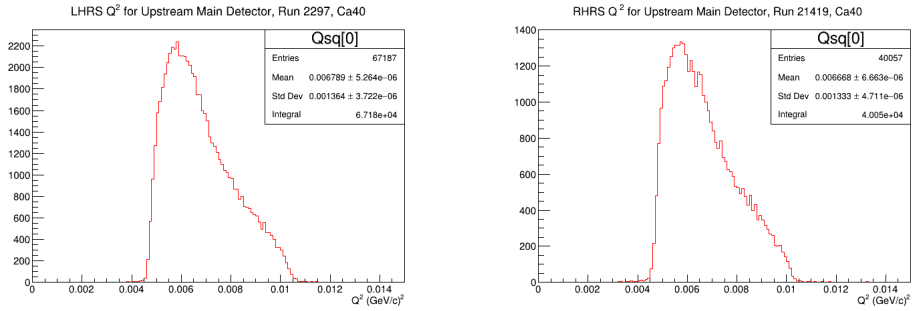

(a) LHRS Ca40 Q^2 (b) RHRS Ca40 Q^2

Figure 4.6: Q^2 distributions for the ^{40}Ca target. The same cuts used for the $\langle \cos\phi \rangle$ histograms were used for Q^2.

The average Q^2 in $(GeV/c)^2$ for each target is given in Table 4.7.

Target	LHRS	RHRS	Average
C12	0.0068	0.0066	0.00671
Pb208	0.0065	0.0063	0.00640
Ca40	0.0068	0.0067	0.00673

Table 4.7: Q^2 values for LHRS and RHRS in units of $(GeV/c)^2$. The ^{208}Pb result was obtained by averaging the LHRS runs and RHRS runs on the different two lead targets.

4.2.6 Beam False Asymmetry Fluctuation Correction

The uncertainty in the beam correction is associated with the dithering correction. The beam false correction is given by Equation 2.3.

The position differences and dithering slopes were measured twice during the transverse run for carbon and lead[2] as shown in Tables 4.3 and 4.4.

The largest beam corrections come from the horizontal position 4eX. Because the largest correction came from the horizontal position 4eX, we took the uncertainty to be dominated by that correction. The source of uncertainty is dominated by how well we measure the 4eX dithering slope. The variation in the 4eX slope between the two data sets is within 5% so 5% of the beam false asymmetry was taken as the uncertainty i.e.,

$$dA_{beam} = \frac{|A_{corr} - A_{raw}|}{20}. \tag{4.20}$$

The systematic uncertainty in the transverse asymmetry due to beam false asymmetry is 11 ppb for ^{12}C, 10 for ^{208}Pb and 43 ppb for ^{40}Ca.

4.2.7 Results

Following the analysis, the results for the asymmetries are

$$A_{C12} = -6.34 \pm 0.38(stat) \pm 0.07(sys)\text{ppm}$$

$$A_{Pb208} = 0.43 \pm 0.16(stat) \pm 0.05(sys)\text{ppm}$$

[2]We only had one measurement on Ca40

$$A_{Ca40} = -6.12 \pm 0.33(stat) \pm 0.08(sys)\text{ppm}.$$

The systematic errors are summarized in Table 4.8 (ppm). The carbon-12 and calcium-40 result are consistent with one another while the lead measurement is consistent with zero. This will be further discussed in Chapter 6.

Error	^{12}C	^{208}Pb	^{40}Ca
Polarization	-0.057	0.004	-0.055
Nonlinearity(BCM+Det)	0.031	0.002	0.026
Beam False Asymmetry	0.011	0.010	0.043
Carbon Contamination		0.044	
Q^2	0.002	0	0.002
Total Syst	0.07	0.05	0.08
Statistical	0.38	0.16	0.33
Total (Stat+Sys)	0.39	0.17	0.34

Table 4.8: Breakdown of systematic and statistical errors given in ppm. The errors are absolute errors

Chapter 5

A_T Corrections

From the PREX-II transverse measurements (Chapter 4.2.5), the ^{208}Pb result is consistent with zero to 0.16 ppm to be compared to a raw A_{PV} of about 0.5 ppm. What this means is that for PREX-II is that the A_T correction was negligible. However, CREX measured an nonzero ^{48}Ca A_n. The CREX ^{48}Ca A_n was measured to be about 9 ppm at $Q^2 = 0.03$ $(GeV/c)^2$. This was about 4 times larger than the predicted parity-violating asymmetry A_{PV} of about 2.3 ppm at CREX kinematics [91]. Therefore, we have to carry out a careful treatment of the A_T correction for CREX. This chapter discusses the correction procedure. The numbers are preliminary. The CREX data is not the main subject of this thesis.

Any residual transverse polarization results in a potential false asymmetry in A_{PV} (see Chapter 1.3.5). Equation 1.31 serves as the starting point which says that when the beam is not 100% longitudinally polarized, the measured asymmetry for each detector consists of three parts, the parity-violating asymmetry and the contributions from the transverse asymmetry due to vertical and horizontal transverse polarization. For the vertical A_T correction, we will use the main detectors. In contrast, a special combination of the A_T detectors will be used to correct for the horizontal A_T.

5.1 Measured Asymmetries Using Kinematic Distributions

Recall from Chapter 2, there are six integrating detectors used during CREX. The main CREX A_{PV} measurement is done by taking the average of the upstream left and right main detectors (See Figure 5.1). But this measurement consists of both the parity-violating part and transverse part with no *a priori* way to decouple the two although there are significant cancellations due to symmetry in the apparatus. The question becomes can we pick a clever combination of detectors that is sensitive to vertical and horizontal transverse polarization while being insensitive to A_{PV}. The answer is yes and requires looking at the kinematic distributions, which give the event by event energy and scattering angle.

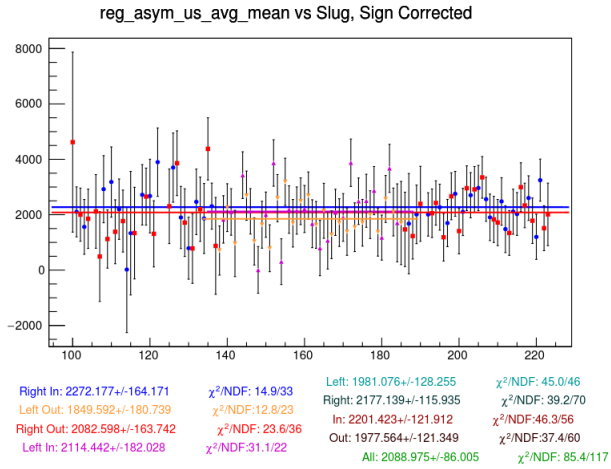

Figure 5.1: The grand average sign corrected asymmetry

As discussed in Chapter 4.2.1, defining the azimuth ϕ relative to the vertical means the vertical transverse asymmetry has a $\langle \cos\phi \rangle$ dependence while the horizontal has $\langle \sin\phi \rangle$ dependence. From equations 4.8 and 4.9, the azimuth depends on θ_{tg} and ϕ_{tg}. Figures 5.2a and b show $\langle \cos\phi \rangle$ and $\langle \sin\phi \rangle$ weighted average main detector acceptance. Lines of constant $\cos\phi$ and $\sin\phi$ are curved. However, to first order $\langle \cos\phi \rangle$ is correlated with θ_{tg}, which is the out-of-plane variable, and $\langle \sin\phi \rangle$ is correlated with ϕ_{tg}, the in-plane variable. Drawing lines of constant θ_{tg} and ϕ_{tg} decouples up/down from left/right (see Figure 5.2 c and d). Since $\sin\phi \approx \phi$, we can think of $\langle \theta_{tg} \rangle$ and $\langle \phi_{tg} \rangle$ as a analyzing power for the horizontal and vertical A_T after accounting for the central angle. From this we have,

$$A_{TV} = P_V A_n \langle \phi_{tg} \rangle, \quad A_{TH} = P_H A_n \langle \theta_{tg} \rangle \tag{5.1}$$

where P_V and P_H are the vertical and horizontal transverse polarization respectively. Using the ansantz that parity-violating asymmetry scales with Q^2 (see Equation 1.19), each integrating detector measures

$$A_m = P_L \hat{A_{PV}} Q^2 + P_V A_n \langle \phi_{tg} \rangle + P_H A_n \langle \theta_{tg} \rangle \tag{5.2}$$

where $\hat{A_{PV}}$ is the invariant asymmetry given in ppm/GeV^{-2}. Equation 5.2 is the starting point for subsequent analysis. To isolate the parity-violating asymmetry, we need to evaluate the second and third terms in equation 5.2.

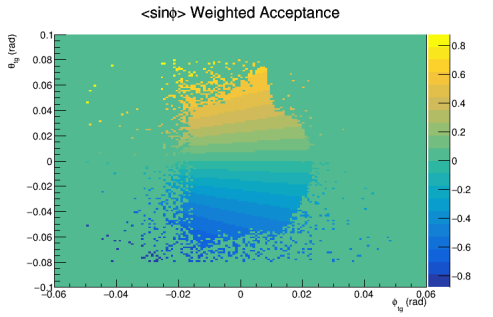

(a) $\langle \sin \phi \rangle$ Weighted Acceptance

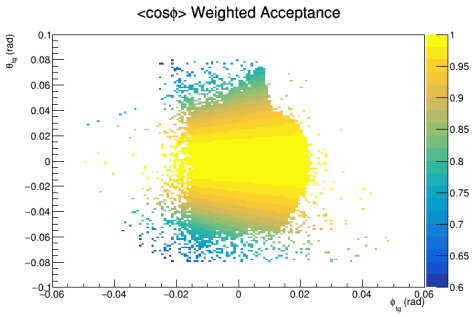

(b) $\langle \cos \phi \rangle$ Weighted Acceptance

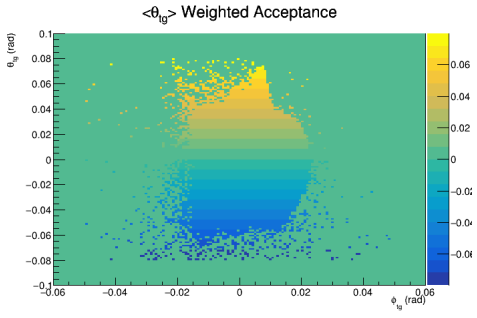

(c) θ_{tg} Weighted Acceptance

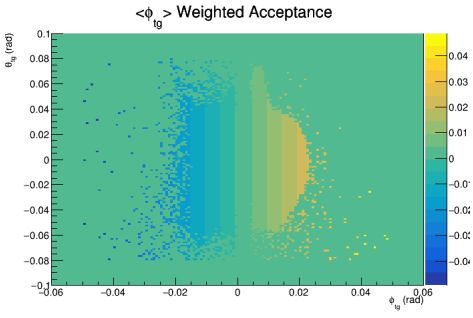

(d) ϕ_{tg} Weighted Acceptance

Figure 5.2: LHRS Acceptance for CREX run 3213. The event cuts used were the same used for the $\langle \cos \phi \rangle$ analysis described in Chapter 4. In these figures, increasing negative ϕ_{tg} corresponds to moving toward beamline. In the RHRS, increasing positive ϕ_{tg} is toward the beamline.

5.2 Vertical Polarization Correction Using Main Detectors

For the main detectors, equation 5.2 reads

$$A_{m,usl} = P_L \hat{A_{PV}} Q^2_{usl} + P_V A_n \langle \phi_{tg} \rangle_{usl} + P_H A_n \langle \theta_{tg} \rangle_{usl} \tag{5.3}$$

$$A_{m,usr} = P_L \hat{A_{PV}} Q^2_{usr} + P_V A_n \langle \phi_{tg} \rangle_{usr} + P_H A_n \langle \theta_{tg} \rangle_{usr} \tag{5.4}$$

where usl and usr refer to the upstream main detectors on the left and right arms respectively. For the transverse running, the longitudinal and horizontal transverse polarization are neglected. We can further define

$$A^T_{m,usl} = P_T A_n \langle \phi_{tg} \rangle_{usl}, \quad A^T_{m,usr} = P_T A_n \langle \phi_{tg} \rangle_{usr}. \tag{5.5}$$

The superscript T indicates that this is transverse running. As discussed in Chapter 4, the A_T measured by the left and right arms comes in opposite sign. Considering the average and double difference of equation 5.5 leads to

$$A^T_{m,usavg} = P_T A_n \frac{\langle \phi_{tg} \rangle_{usl} + \langle \phi_{tg} \rangle_{usr}}{2} \tag{5.6}$$

$$A^T_{m,usdd} = P_T A_n \frac{\langle \phi_{tg} \rangle_{usl} - \langle \phi_{tg} \rangle_{usr}}{2}. \tag{5.7}$$

Taking the ratio of equation of equations 5.6 and 5.7 leads to

$$\xi = \frac{A^T_{m,usavg}}{A^T_{m,usdd}} = \frac{\langle \phi_{tg} \rangle_{usl} + \langle \phi_{tg} \rangle_{usr}}{\langle \phi_{tg} \rangle_{usl} - \langle \phi_{tg} \rangle_{usr}} \tag{5.8}$$

where ξ is the left-right apparatus asymmetry. Since $\langle \phi_{tg} \rangle_{usl}$ and $\langle \phi_{tg} \rangle_{usr}$ have opposite sign, ξ is small.

For production running, the average and double difference are

$$A_{m,usavg} = P_L \hat{A_{PV}} Q^2_{us,avg} + P_V A_n \langle \phi_{tg} \rangle_{us,avg} + P_H A_n \langle \theta_{tg} \rangle_{us,avg} \tag{5.9}$$

$$A_{m,usdd} = P_L \hat{A_{PV}} Q^2_{us,d} + P_V A_n \langle \phi_{tg} \rangle_{us,d} + P_H A_n \langle \theta_{tg} \rangle_{us,d} \tag{5.10}$$

with

$$Q^2_{usavg,d} = \frac{Q^2_{usl} \pm Q^2_{usr}}{2}$$
$$\langle \phi_{tg} \rangle_{usavg,d} = \frac{\langle \phi_{tg} \rangle_{usl} \pm \langle \phi_{tg} \rangle_{usr}}{2}$$
$$\langle \theta_{tg} \rangle_{usavg,d} = \frac{\langle \theta_{tg} \rangle_{usl} \pm \langle \theta_{tg} \rangle_{usr}}{2}.$$

We now address which main detector combination can be used as a vertical transverse polarization monitor. Before that, a discussion about the A_T due to a horizontal polarization is necessary. To understand the magnitude of $\langle \theta_{tg} \rangle$ for the main detectors, we revisit Figure 5.2c as an example. If the top/bottom apparatus symmetry is broken, events at the top/bottom of the acceptance are more sensitive to A_T ($\langle \theta_{tg} \rangle$ is increasing) relative to the events at the center of acceptance where the A_T sensitivity is roughly zero. So for an apparatus that is perfectly symmetric top to bottom, there is cancellation leading to a null A_T sensitivity at the main detectors. The acceptance defining collimators were designed and installed to millimeter top/bottom tolerance. Given this, a 1 mm vertical misalignment in the acceptance would result in $\langle \theta_{tg} \rangle$ on the order of 10^{-4} and then for a -9.34 ppm A_n, the transverse asymmetry measured by the main detectors is suppressed by at least 100. This means that we can't use the main detectors as a horizontal transverse monitor since $\langle \theta_{tg} \rangle$ is small and we can neglect the third terms in equations 5.9 and 5.10. With this in mind and recalling that the vertical A_T comes in opposite sign between the left and right arms, the double difference can be used as vertical transverse monitor. In this case, equation 5.10 can be written as

$$A_{m,usdd} \approx P_L \hat{A_{PV}} Q^2_{usd} + P_V \langle \phi_{tg} \rangle_{usd}. \tag{5.11}$$

If Q^2 is the same between the left and right arms, the first term in equation 5.13 is zero. However, for a difference in Q^2 we must subtract that part from the double difference,

$$A_{m,corr,usdd} = A_{m,usdd} - P_L \hat{A_{PV}} Q^2_{usd} = P_V A_n \langle \phi_{tg} \rangle_{usd} \tag{5.12}$$

where the $A_{m,corr,usdd}$ is the Q^2 corrected double difference. The corrected double difference is then a direct measure of the vertical transverse polarization. Equation 5.12 together with equation 5.8 gives the vertical A_T correction, $A_{TV,usavg}$ for the upstream average i.e.,

$$A_{TV\,usavg} = A_{m,corr,usdd}\xi \tag{5.13}$$

while the systematic error in that correction is

$$\frac{dA_{TV\,usavg}}{A_{TV\,usavg}} = \sqrt{(\frac{dA_{m,corr,usdd}}{A_{m,corr,usdd}})^2 + (\frac{d\xi}{\xi})^2} \tag{5.14}$$

We can also find the fraction of the beam that is vertically polarized, f_V. This is obtained by taking the ratio of the corrected double difference (equation 5.12) and the double difference from transverse running (equation 5.7). The fraction f_V and its uncertainty is given by

$$f_V \equiv \frac{P_V}{P_T} = \frac{A_{m,corr,usdd}}{A^T_{m,usdd}}. \tag{5.15}$$

$$\frac{df_V}{f_V} = \sqrt{(\frac{dA_{m,corr,usdd}}{A_{m,corr,usdd}})^2 + (\frac{dA^T_{m,usdd}}{A^T_{m,usdd}})^2} \tag{5.16}$$

5.2.1 Vertical A_T Correction Analysis

The vertical A_T correction given by equation 5.13, requires computing the left/right apparatus asymmetry ξ and the corrected double difference. The corrected double difference comes from the production integrating measurement, while ξ can be extracted from either counting mode measurements or transverse integrating mode measurements. From the transverse data, ξ is can be extracted using either the regression or dither corrected averages and double differences. The regression and dither corrected values and their errors (ppb) for transverse running are given in Table 5.1.

	$A^T_{reg,usavg}$	$A^T_{dit,usavg}$	$A^T_{reg,usdd}$	$A^T_{dit,usdd}$
^{48}Ca	-172.844 ± 844.647	-290.674 ± 852.216	7969.8 ± 837.6	7916.9 ± 839.2

Table 5.1: ^{48}Ca average and double difference for vertical transverse running

The uncertainty in ξ given by

$$\frac{d\xi}{\xi} = \sqrt{(\frac{dA^T_{m,usavg}}{A^T_{m,usavg}})^2 + (\frac{dA^T_{m,usdd}}{A^T_{m,usdd}})^2} \tag{5.17}$$

leading to

	ξ_{reg}	ξ_{dit}
^{48}Ca	-0.022 ± 0.110	-0.037 ± 0.108

Table 5.2: Left/Right apparatus asymmetry calculated from regression and dithering

For the counting mode measurements, we use the Q^2 runs to calculate ξ using the average of the reconstructed angles in the spectrometer optics for each event. The asymmetry ξ is calculated on a run by run basis, by taking the central values of the $\langle \phi_{tg} \rangle$ distributions for a LHRS run and its corresponding RHRS run. Then ξ is computed using the central values. Figure 5.3 show ξ values calculated from counting mode which are compared to the ξ measurements from integrating mode using both regression and dithering. The figures show that the counting mode measurements fall within the error of the integration measurements (see bands in Figure 5.3). However, due to large statistical uncertainties in the integrating measurements, ξ for counting mode is used to do the vertical A_T correction. Only runs where there is clean signal to pedestal separation in the ADC spectra were considered for this analysis.

Figure 5.3 shows a discrete change in ξ between the pre-COVID and post-COVID run periods. For this reason, the data is broken up into pre and post-COVID periods where the A_T corrections are done separately. The ξ measurements from counting mode were fit to a line which is shown in Figure 5.4 and the results from the fits are summarized in Table 5.3.

	Pre-COVID	Post-COVID
ξ	0.0329 ± 7.5e-04	-0.0432 ± 2.93e-03

Table 5.3: Pre and post-COVID ξ values. The uncertainties are from the fit.

The next part of the analysis involves removing the Q^2 dependence of the measured double difference $A_{m,usdd}$ to get the corrected double difference $A_{m,corr,usdd}$ (equation 5.12). The signed corrected double difference is shown in Figure 5.8 and tabulated in table 5.4. The error bars in the measured double difference are statistical.

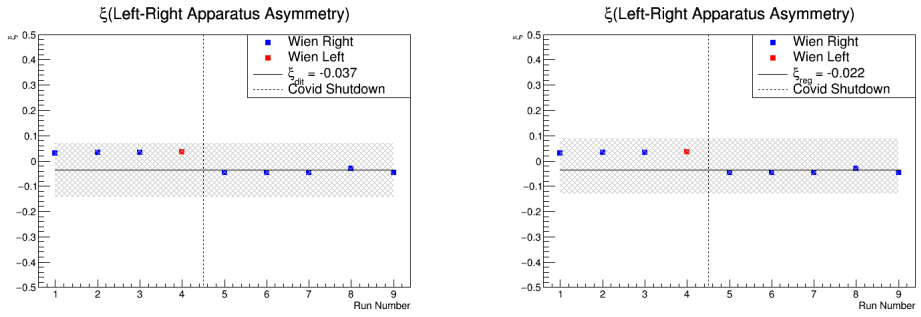

(a) Dithering (b) Regression

Figure 5.3: Comparison of the counting mode measurements with integrating measurement. (a) Uses the dithering result (b) Uses the regression mode. The shaded region represents the errors from integrating measurement while solid line represents the central value. The dashed line indicates whether the data was taken pre or post-COVID shutdown. Counting measurements fall within the error of the integrating measurements. The uncertainties in the counting mode measurements are negligible in these figures

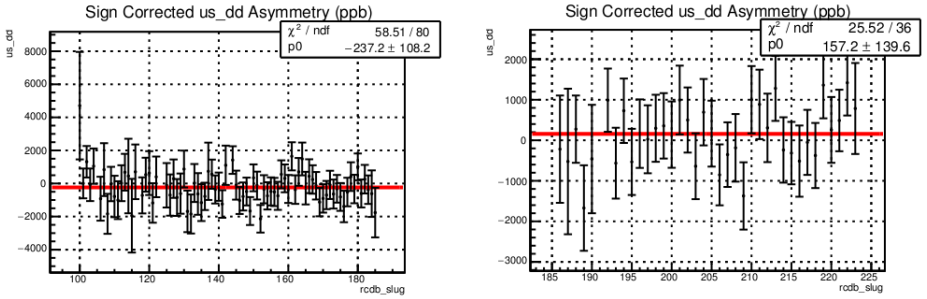

(a) Pre-COVID double difference (b) Post-COVID double difference

Figure 5.5: Signed Corrected Double Differences vs. Slug Number in ppb

Removing the Q^2 dependence in the double difference requires computing the invariant asymmetry $\hat{A_{PV}}$ and knowing the polarization. Using the predicted asymmetry of about 2.3 ppm at $Q^2 = 0.03 GeV^{-2}$, which gives $\hat{A_{PV}}$ is 77 ppm/GeV^{-2}. This value will be used for subsequent analysis.

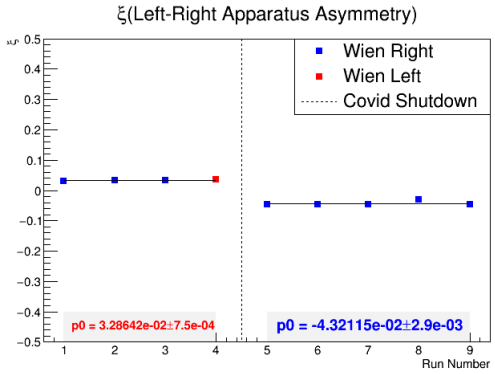

Figure 5.4: ξ fits pre and post-COVID

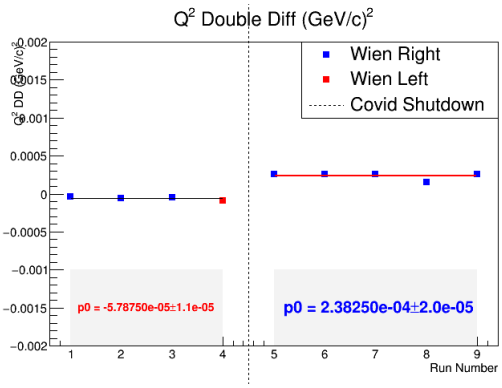

Figure 5.6: Q^2 Double Differences for the main detector. The units are $(GeV/c)^2$

The Q^2 double differences are shown in Figure 5.6 and was computed to same way as ξ i.e., using the central values of the distributions for a given run. The parity-violating component $A_{PV,usdd}$ is -4.44 $\pm$ 0.84 ppb and 18.27 $\pm$ 1.53 ppb for the pre and post COVID run periods respectively. The errors here consider the errors from the Q^2 double difference fit and polarization. The longitudinal polarization was taken from a preliminary analysis of the Møller polarimeter measurements. The polarization was measured to 86.7 $\pm$ 0.06 % pre-COVID and 87.5 $\pm$ 0.07 % post-COVID [92]. The parity violating component measured by the main detector double difference is tabulated in Table 5.4, while the corrected double difference is given in Table 5.5, both of which are given in ppb.

	Pre COVID	Post COVID
$A_{PV,usdd}$	-3.85 ± 0.73	15.98 ± 1.35

Table 5.4: Parity-violating component in the double difference of the main detectors in ppb.

	Pre COVID	Post COVID
$A_{m,corr,usdd}$	-233.4 ± 108.2	141.2 ± 139.6

Table 5.5: Corrected double difference in ppb

The values from tables 5.5 together with the ξ values from table 5.3 give the vertical A_T correction $A_{TV,usavg}$. The pre and post-COVID corrections and their uncertainties are shown in table 5.6.

	Pre COVID	Post COVID
$A_{TV,usavg}$	-7.68 ± 3.56	-6.10 ± 6.04

Table 5.6: pre and post-COVID Vertical A_T corrections given in units of ppb.

From the errors given in Table 5.6, the uncertainty in the vertical A_T correction is less than 5% of the statistical error of the double difference for both run periods. The statistical error in the average is about the same as the double difference. This means for a 4% precision measurement of A_{PV}, the total statistical error is about 90 ppb for A_{PV} of about 2.3 ppm at CREX kinematics. The vertical A_T systematic error is about 4.5 ppb which in quadrature with the total statistical error changes the error bar from 90 ppb to 90.1 ppb which is negligible.

The magnitude of the fraction of the beam that is transverse polarized vertically and its error is given by equations 5.15 and 5.16. Using the regressed asymmetry double difference from Table 5.1 together with the corrected double differences from Table 5.6, we get f_V. The values are given in % and summarized in Table 5.8.

	Pre COVID	Post COVID
f_V	-2.9 ± 1.39	1.77 ± 1.76

Table 5.7: Magnitude of the vertical transverse polarization

5.3 Horizontal Polarization Correction Using A_T Detectors

The null horizontal A_T sensitivity for the main detectors means that we cannot use the main detectors to monitor horizontal polarization. Given that we need a way to account for the case there is residual transverse polarization. To do that, we use the A_T detectors. The A_T detectors located about a meter downstream of the main detectors, were placed to intercept events at the top and bottom of the acceptance where the events are A_T enhanced, where the A_T sensitivity is maximized.

5.3.1 A_T Detector Placement Optimization

The A_T detector locations were determined by optimizing the square root of horizontal A_T figure of merit defined as

$$A_{T,FOM} = R\langle\theta_{tg}\rangle^2 \tag{5.18}$$

where R is the accepted rate at the detector. This quantity is a measure of how well the A_T detectors measure a horizontal A_T. The A_T detectors were designed to isolate the blue and yellow spots indicating the top and bottom of the acceptance of Figure 5.7. Each A_T detector has an active area 3.5x10 cm^2. By introducing two A_T detectors, one for each spot, a position scan was performed, scanning both vertically and horizontally. At each position, the horizontal A_T sensitivity and sqrt(FOM) was calculated by integrating over the detector dimensions. In counting mode, the detector intercepting the yellow blob is called A_T In and the other is A_T Out. In integrating, A_T In is referred to atl1, while the other is atl2 on the left arm.

The position scan was performed using data. In the data, an acceptance function was defined, which represented the quartz response due the tracks

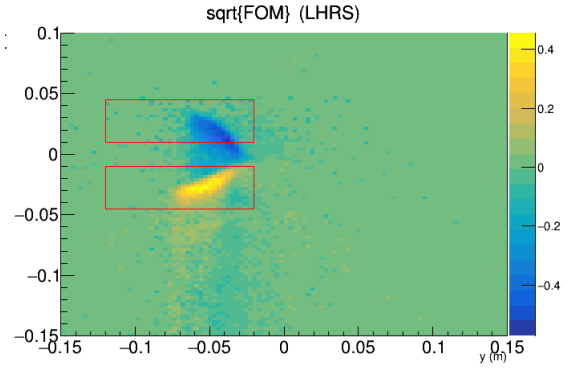

Figure 5.7: Plot of the $\sqrt{A_{T,FOM}}$ for a given run. The red boxes indicate the A_T detectors, one for each spot sensitive to the top/bottom of the acceptance. The optimal location of these detectors are found by scanning the position in x (vertically) and y (horizontally).

that hit the detector. This is defined as the ratio of two histograms, one of which has an additional cut on the ADC spectrum of the A_T detectors (see Figure 5.8). To parameterize the acceptance function, small slices were fit vertically and horizontally making sure to highlight the falloff in probability (e.g., yellow to light blue). The slice in y (vertical slice) was fit to the difference in error functions, parameterized by the amplitude and Gaussian sigma and two means, representing the edges of the detector. The x (horizontal slice) was fit with a complementary error function also parameterized by an amplitude, sigma and mean.

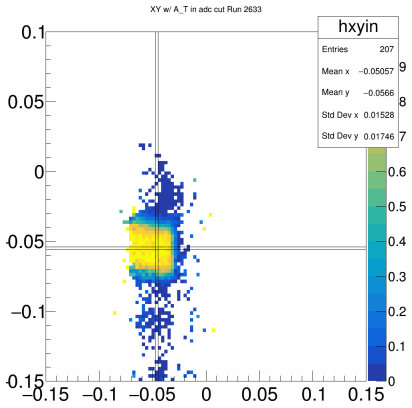

Figure 5.8: Acceptance Function for A_T In for a CREX run. The color scale represents the probability that quartz fired given the tracks that hit it. The falloff from yellow to blue is indicative of edges of the detector. The lines represent the slices taken to parameterize the acceptance function.

To do the position scan, the acceptance function was used as a weight by varying the edge parameters described by the means of the fit distribution. The results for the A_T FOM scan for the left arm A_T detectors are shown in Figure 5.9.

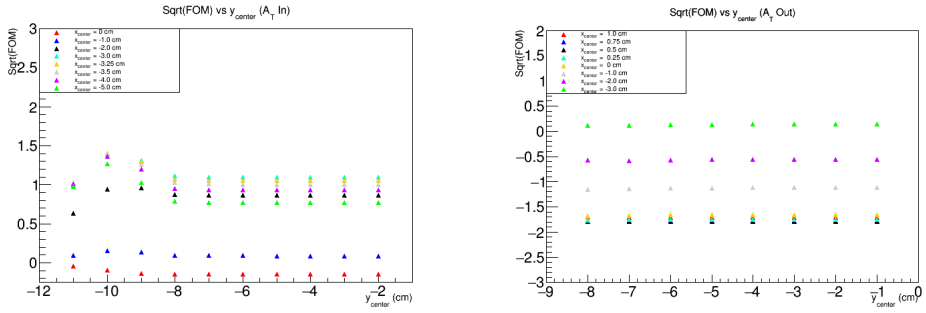

(a) atl1 Scan

(b) atl2 Scan

Figure 5.9: A_T FOM position scans. (a) is for A_T in. (b) is for A_T out. Going toward zero on the vertical axis for (a) implies moving toward positive x indicating we are accepting more of the blue spot (figure 5.3). It is the opposite for (b) meaning we are accepting more yellow. The horizontal axis represents the detector center. If the edge is at -4 cm, the -9 cm is y_{center} (along transverse dimension. The A_T Out detector's FOM is insensitive to the y position while A_T In has a preferred location in y

5.3.2 Extracting the Horizontal Transverse Polarization using the A_T Detectors

Once the A_T detectors are placed in their ideal positions, the next thing is to work out which combinations of A_T detectors are sensitive to the horizontal transverse polarization while suppressing A_{PV}. For simplicity, only the left arm will be considered. Returning back to equation 5.2, the two left arm A_T detectors measure

$$A_{m,atl1} = P_L \hat{A_{PV}} Q^2_{atl1} + P_V A_n \langle \phi_{tg} \rangle_{atl1} + P_H A_n \langle \theta_{tg} \rangle_{atl1} \tag{5.19}$$

$$A_{m,atl2} = P_L \hat{A_{PV}} Q^2_{atl2} + P_V A_n \langle \phi_{tg} \rangle_{atl2} + P_H A_n \langle \theta_{tg} \rangle_{atl2}. \tag{5.20}$$

Considering the case where the beam is transversely polarized vertically, the average and double difference of A_T detectors on the left arm measure

$$A^T_{m,atlavg} = P_V A_n \frac{\langle \phi_{tg} \rangle_{atl1} + \langle \phi_{tg} \rangle_{atl2}}{2} \tag{5.21}$$

$$A^T_{m,atldd} = P_V A_n \frac{\langle \phi_{tg} \rangle_{atl1} - \langle \phi_{tg} \rangle_{atl2}}{2}. \tag{5.22}$$

As discussed in 5.1.1, the left and right arms measure A_T with opposite sign, implying equation 5.21 is sensitive to the vertical A_T since $\langle \phi_{tg} \rangle_{atl1}$ and $\langle \phi_{tg} \rangle_{atl2}$ have the same sign.

For a transversely polarized beam horizontally, the average and double difference are

$$A^H_{m,atlavg} = P_H A_n \frac{\langle \theta_{tg} \rangle_{atl1} + \langle \theta_{tg} \rangle_{atl2}}{2} \tag{5.23}$$

$$A^H_{m,atldd} = P_H A_n \frac{\langle \theta_{tg} \rangle_{atl1} - \langle \theta_{tg} \rangle_{atl2}}{2}. \tag{5.24}$$

In this case, double difference measures the horizontal A_T, while in average the horizontal A_T is suppressed since the one A_T detector isolates events with a negative average θ_{tg} while the other isolates events with a positive θ_{tg}. For production running, the double difference of the two A_T detectors gives

$$A_{m,atldd} \approx P_L \hat{A_{PV}} \frac{Q^2_{atl1} - Q^2_{atl2}}{2} + P_H A_n \frac{\langle \theta_{tg} \rangle_{atl1} - \langle \theta_{tg} \rangle_{atl2}}{2}. \tag{5.25}$$

Removing the Q^2 dependence, the corrected double difference $A_{m,corr,atldd}$ is given by

$$A_{m,corr,atldd} = A_{m,atldd} - P_L \hat{A_{PV}} \frac{Q^2_{atl1} - Q^2_{atl2}}{2}. \tag{5.26}$$

Equation 5.26 is a horizontal transverse monitor. Using equation 5.26, the correction due to a horizontal A_T for left arm main detector is

$$A_{TH,usl} = \frac{A_{m,corr,atldd}}{\chi_{LHRS}} \tag{5.27}$$

where

$$\chi_{LHRS} = \frac{\langle\theta_{tg}\rangle_{atl1} - \langle\theta_{tg}\rangle_{atl2}}{2\langle\theta_{tg}\rangle_{usl}}. \tag{5.28}$$

The correction factor χ_{LHRS} can be thought of as an up/down apparatus asymmetry. The error in the correction is

$$\frac{dA_{TH,usl}}{A_{TH,usl}} = \sqrt{(\frac{dA_{m,corr,atldd}}{A_{m,corr,atldd}})^2 + (\frac{d\chi_{LHRS}}{\chi_{LHRS}})}. \tag{5.29}$$

One can also extract the portion of the beam polarized horizontally transverse. The horizontal transverse beam polarization and its uncertainty is obtained from

$$P_H = \frac{A_{m,corr,atldd}}{A_n \langle\theta_{tg}\rangle_{atld}} \tag{5.30}$$

$$\frac{dP_H}{P_H} = \sqrt{(\frac{dA_{m,corr,atldd}}{A_{m,corr,atldd}})^2 + (\frac{dA_n}{A_n})^2 + (\frac{d\langle\theta_{tg}\rangle_{atld}}{\langle\theta_{tg}\rangle_{atld}})^2} \tag{5.31}$$

5.3.3 Horizontal A_T Correction Analysis

After correcting for the vertical A_T contribution, we correct for the horizontal A_T using equations 5.26-5.29. The correction involves correcting for the Q^2 dependence for the A_T detectors and calculating the up/down apparatus asymmetry. The analysis presented in this thesis will be for the left arm. The pre and post-COVID grand averages for the upstream left main detector and A_T double difference is given in Table 5.8 while the plots are shown in Figure 5.10.

	$A_{m,usl}$	$A_{m,atldd}$
Pre-COVID	1795 ± 154.1	-150 ± 241.3
Post-COVID	2339 ± 197.6	-298 ± 305.1

Table 5.8: Pre and post-COVID regressed asymmetries in ppb for the left main detector and the double difference for the A_T detector

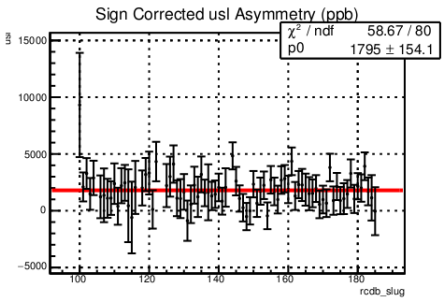

(a) Pre-COVID $A_{m,usl}$

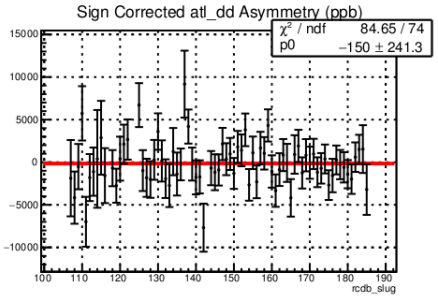

(b) Pre-COVID $A_{m,atldd}$

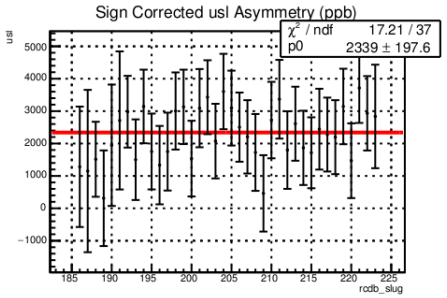

(c) Post-COVID $A_{m,usl}$

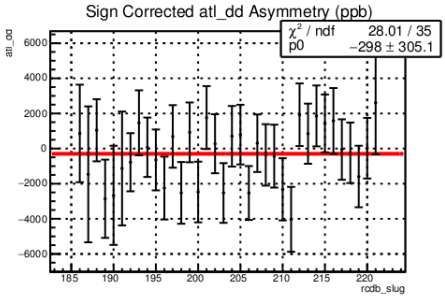

(d) Post-COVID $A_{m,atdd,avg}$

Figure 5.10: Grand average regressed $A_{m,usl}$ and $A_{m,atldd}$ vs. Slug Number in ppb

As done in the Section 5.2.1, the Q^2 dependence must be removed from the regressed values for the A_T double difference. The Q^2 difference is shown in Figure 5.11 for the left and right arms. The data set consisted of runs where the A_T detectors weren't touched from their optimally placed positions. Using the invariant asymmetry and polarization measurements from Section 5.2, the

parity-violating component (in ppb) in the A_T double difference is given in Table 5.9 .

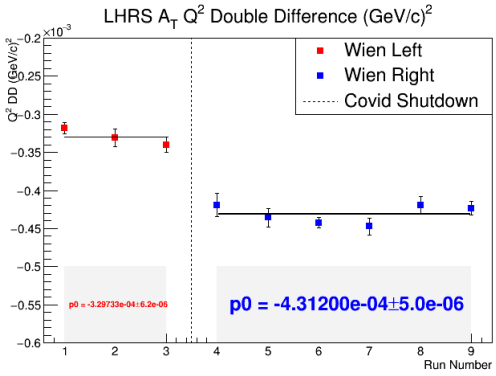

Figure 5.11: Q^2 Difference for the Pre and Post-COVID Run Periods. The error bars are statistical in units of $(GeV/c)^2$

	Pre-COVID	Post-COVID
$A_{PV,atldd}$	-21.93 ± 1.94	-28.91 ± 2.75

Table 5.9: Pre and Post-COVID parity-violating Component for A_T double difference given in ppb

The Q^2 corrected A_T double difference is given below in Table 5.10.

	Pre-COVID	Post-COVID
$A_{m,corr,atldd}$	-128.1 ± 241.3	-269.1 ± 305.1

Table 5.10: Corrected A_T double difference given in ppb

The last part of the analysis involves obtaining the up/down asymmetry χ_{LHRS}, which is also computed using the central values of the distributions. The fit for χ_{LHRS} is shown in Figure 5.12 while the fit values are summarized in Table 5.11.

The horizontal A_T correction is then given by 21.6 ± 40.7 ppb for the pre-COVID period and 43 ± 48.8 ppb for the post-COVID period. This is also shown in Table 5.12.

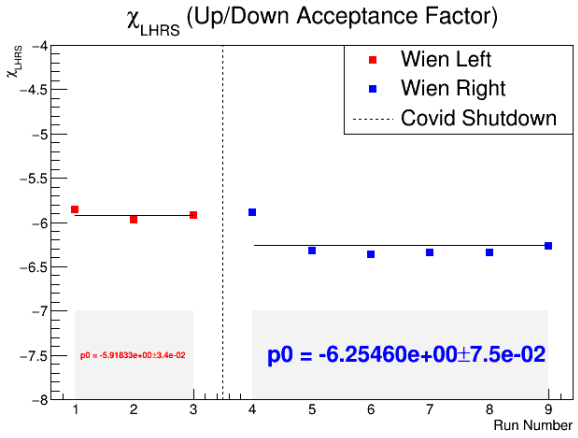

Figure 5.12: Up/Down Apparatus asymmetry for the Horizontal A_T correction. The uncertainties are negligible

	Pre-COVID	Post-COVID
χ_{LHRS}	-5.9 ± 3.4e-02	-6.3 ± 7.5e-02

Table 5.11: χ_{LHRS} values pre and post-COVID. The uncertainty is from the fits

	Pre-COVID	Post-COVID
$A_{TH,usl}$	21.6 ± 40.7	43 ± 48.8

Table 5.12: Corrected A_T double difference given in ppb

The statistical errors for the left upstream main detector were 154.1 ppb and 197.6 ppb pre and post-COVID. From the uncertainties in the horizontal A_T correction given in table 5.12, we see that the systematic error is about 25% of the statistical error measured by the main detector. If this is true on the right arm as well, then for a 4% measurement in A_{PV} with a 90 ppb error, the systematic error due to a horizontal A_T is about 22.5 ppb. Adding these errors in quadrature, the error goes from 90 ppb to 92.8 ppb. Including the error from the vertical A_T (4.5 ppb), the quadrature sum of the statistical error and the systematic due to A_T goes from 90 to 92.9 ppb.

The horizontal transverse polarization is gotten from equations 5.30 and 5.31. The measured vector analyzing power for ^{48}Ca was -9.35 ± 1.09 ppm (statistical error). The $\langle\theta_{tg}\rangle_{atld}$ shown in Figure 5.13. Using the numbers

from Table 5.10, the horizontal transverse polarization and its uncertainty is summarized in Table 5.13.

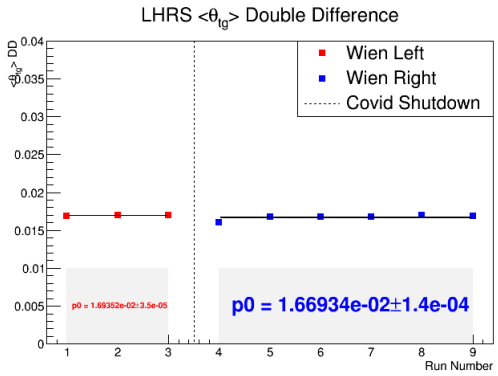

Figure 5.13: $\langle\theta_{tg}\rangle_{atd}$ fits pre- and post-COVID

	Pre-COVID	Post-COVID
P_H	0.81 $\pm$ 1.53	1.72 $\pm$ 1.95

Table 5.13: Extracted horizontal transverse beam polarization

Chapter 6

Results and Discussion

6.1 A_n Measurements at 1 GeV

The PREX-II A_n measurements were summarized in Chapter 4.2.7. These measurements are shown together with the PREX-I measurements in Figure 6.1. Figure 6.1 shows the new theory predictions at $E_{beam} = 0.95$ GeV/c, based on the calculations done by [42] where the Dirac equation was solved numerically with an optical potential while including Coulomb distortions. Together with the old theory predictions which used the optical theorem [31] (see Figure 1.14a), the data indicates that the dynamics of light to intermediate mass nuclei are well understood within both theoretical frameworks. The ^{208}Pb measurements remain discrepant with both theoretical predictions at two different Q values. It should be noted that the new calculation is somewhat closer to the measured ^{208}Pb result but it's still over 15 standard deviations away from theory. In contrast, the ^{12}C and ^{40}Ca results are somewhat consistent.

The ^{40}Ca measurement provided new insight on the Z dependence of the analyzing power. The fact that the result is consistent with the old model seems to indicate that Coulomb distortions don't play as big a role which is consistent with the new theory at PREX-II kinematics. This strongly suggests that the theoretical model is missing important dynamics, and therefore further investigation is needed. The PREX-II and CREX (2 GeV) A_n measurements will be published together in the upcoming months.

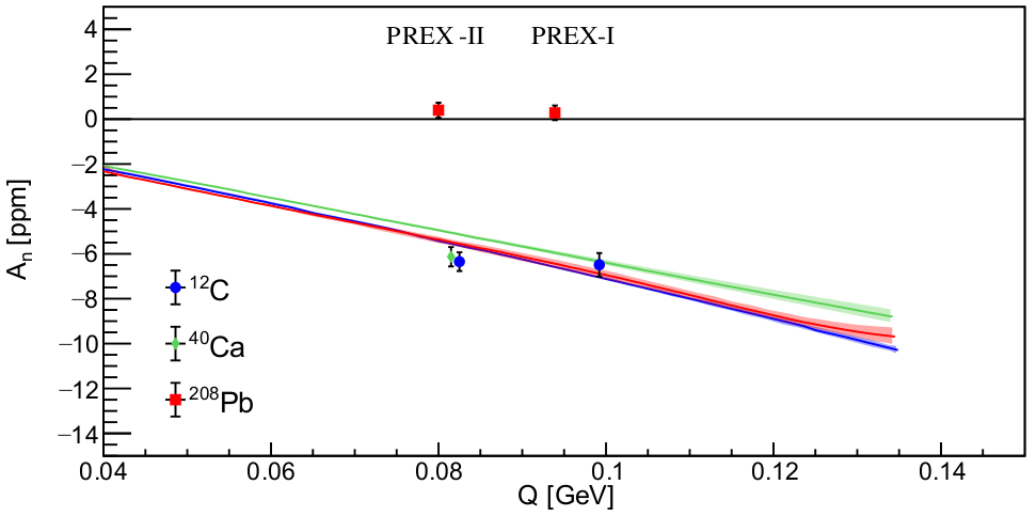

Figure 6.1: PREX-I and PREX-II A_n measurements at beam energies E_{beam} = 1.06 GeV/c and 0.95 GeV/c respectively. Overlapping points were offset slightly in Q.

6.2 Neutron Skin Thickness Measurements

As discussed in Chapter 5, the A_n measurement of ^{208}Pb during PREX-II resulted in no correction to the ^{208}Pb A_{PV} analysis. The PREX-II collaboration reported an A_{PV} measurement of 550 $\pm$ 18(total) ppb at $Q^2 = 0.0062$ $(GeV/c)^2$. The weak form factor was extracted to be 0.318 $\pm$ 0.013 at PREX-II kinematics. The neutron skin thickness r_{ns} defined as the difference between the point neutron and proton radius was measured to be 0.283 $\pm$ 0.071 fm [70]. CREX plans to report an A_{PV} measurement which will lead to a neutron skin measurement on ^{48}Ca. The CREX analysis is underway and the result is forthcoming. The CREX A_{PV} measurement may follow the PREX-II observation of a large neutron skin, stimulating interest in what CREX will say about the neutron skin thickness on ^{48}Ca.

Bibliography

[1] Jon Wexler, *Measurement of Parity Violating Asymmetry in Elastic Electron Scattering off 208Pb*. PhD Thesis, University of Massachusetts Amherst, May 2014.

[2] Mark Thomson, Modern Particle Physics.New York, Cambridge University Press, 2013.

[3] Caryn A. Palatchi, *Laser and Electron Beam Technology for Parity Violating Electron Scattering Measurements*. PhD Thesis, University of Virginia, May 2019.

[4] L. Ray, W. R. Coker, G. W. Hoffmann, Phys. Rev. C 18, 2641 (1978).

[5] V. E. Starodubsky, N. M. Hintz, Phys. Rev. C 49, 2118 (1994)

[6] B. C. Clark, S. Hama, L. J. Kerr, Phys. Rev. C 67, 054605 (2003).

[7] C. Garcia-Recio, J. Nieves and E. Oset, Nucl. Phys. A 547, 473 (1992).

[8] A. Trzcinska et al., Phys. Rev. Lett. 87, 082501 (2001).

[9] H. Lenske, Hyperfine Interact. 194, 277 (2009).

[10] Krishna Kumar, "The PREX and CREX experiments. Measurements of the Parity-Violating Electron Scattering Asymmmetries off of ^{208}Pb and ^{48}Ca: The first PREX Result at Jefferson Laboratory and Future Plans", 3rd International Symposium on Nuclear Symmetry Energy, NSCL/FRIB, East Lansing, MI, July 25, 2013

[11] Seamus Riordan, "PREX Overview Extracting the Neutron Radius from ^{208}Pb", CREX Workshop, Thomas Jefferson National Accelerator Facility, Newport News, VA, March 17, 2013

[12] B. Waidyawansa, *A 3% Measurement of the Beam Normal Single Spin Asymmetry in Forward Angle Elastic Electron-Proton Scattering using the Q_{weak} Setup*. PhD Thesis, Ohio University, August 2013.

[13] R. Arnold, C. E. Carlson, and F. Gross, "Polarization Transfer in Elastic electron Scattering from Nucleons and Deuterons," Phys.Rev., vol. C23, p. 363 (1981).

[14] M. Rosenbluth, "High Energy Elastic Scattering of Electrons on Protons", Phys.Rev., vol. 79, pp. 615–619 (1950).

[15] L. W. Mo and Y.-S. Tsai, "Radiative Corrections to Elastic and Inelastic ep and p Scattering", Rev.Mod.Phys., vol. 41, pp. 205–235 (1969).

[16] L. Maximon and J. Tjon, "Radiative Corrections to Electron Proton Scattering," Phys.Rev., vol. C62, p. 054320 (2000)

[17] J. Arrington, P. Blunden, and W. Melnitchouk, "Review of Two-Photon Exchange in Electron Scattering," Prog.Part.Nucl.Phys., vol. 66, pp. 782–833 (2011).

[18] P. Blunden, W. Melnitchouk, and J. Tjon, "Two Photon Exchange and Elastic Electron Proton Scattering," Phys.Rev.Lett., vol. 91, p. 142304 (2003).

[19] P. A. Guichon and M. Vanderhaeghen, "How to Reconcile the Rosenbluth and the Polarization Transfer Method in the Measurement of the Proton Form factors," Phys.Rev.Lett., vol. 91, p. 142303 (2003).

[20] J. Arrington, W. Melnitchouk, and J. Tjon, "Global Analysis of Proton Elastic Form Factor Data With Two-Photon Exchange Corrections," Phys.Rev., vol. C76, p. 035205 (2007).

[21] B. Pasquini and M. Vanderhaeghen, "Single Spin Asymmetries in Elastic Electron Nucleon Scattering", Phys.Rev., vol. C70, p. 045206 (2004).

[22] Y. W. Zhang et al. (Jefferson Lab Hall A Collaboration), Phys. Rev. Lett. 115, 172502 (2015).

[23] A. Browman, F. Liu, and C. Schaerf, "Positron-Proton Scattering", Phys.Rev., vol. 139, pp. B1079–B1085 (1965).

[24] R. Anderson et al., "Scattering of Positrons and Electrons from Protons", Phys.Rev.Lett., vol. 17, pp. 407–409 (1966).

[25] J. Mar et al., "A Comparison of Electron-Proton And Positron-Proton Elastic Scattering At Four Momentum Transfer Up To 5.0 $(GeV/c)^2$", Phys.Rev.Lett.,vol. 21, pp. 482–484 (1968).

[26] R. Anderson et al., "Positron-Proton Elastic Scattering at 800 and 1200 MeV", Phys.Rev., vol. 166, pp. 1336–1342 (1968).

[27] J. Arrington et al., "Beyond the Born Approximation: A Precise Comparison of e+ p and e p Elastic Scattering in CLAS", A Proposal Prepared for Jefferson Lab PAC31

[28] R. G. Milner, "The OLYMPUS Experiment", AIP Conf.Proc., vol. 1441, pp. 159–161 2012.

[29] J. Arrington, "Evidence for Two Photon Exchange Contributions in Electron Proton and Positron Proton Elastic Scattering", Phys.Rev., vol. C69, p. 032201 (2004).

[30] E. D. Cooper and C. J. Horowitz, "Vector analyzing power in elastic electron-nucleus scattering", Phys. Rev. C 72, 034602 (2005).

[31] M. Gorchtein and C. J. Horowitz," Analyzing power in elastic scattering of electrons off a spin-0 target", Phys. Rev. C 77, 044606 (2008).

[32] M. Gorchtein, "Doubly virtual Compton scattering and the beam normal spin asymmetry", Phys. Rev. C 73, 035213, 2006

[33] Krishna Kumar, "A_n Experiments", The Electroweak Box Workshop at ACFI, University of Massachusetts Amherst, September 28, 2017

[34] L. Diaconescu and M. Ramsey-Musolf, "Vector analyzing power in elastic electron-proton scattering", Phys. Rev. C 70, 054003 (2004).

[35] A. V. Afanasev and N. Merenkov, " Collinear photon exchange in the beam normal polarization asymmetry of elastic electron–proton scattering", Phys. Lett. B599, 48 (2004).

[36] M. Gorchtein, P. A. M. Guichon, and M. Vanderhaeghen, "Beam normal spin asymmetry in elastic lepton–nucleon scattering", Nucl. Phys. A741, 234 (2004).

[37] D. Drechsel, O. Hanstein, S. Kamalov, and L. Tiator, "A Unitary Isobar Model for Pion Photoproduction and Electroproduction on the Proton up to 1-GeV", Nucl.Phys., vol. A645, pp. 145–174, 1999.

[38] S. Wells et al., "Measurement of the Vector Analyzing Power in Elastic Electron Proton Scattering as a Probe of Double Photon Exchange Amplitudes", Phys.Rev., vol. C63, p. 064001 (2001)

[39] A. Afanasev, I. Akushevich, and N. Merenkov, "Nucleon Compton Scattering with Two Space - Like Photons", pp. 142–150 (2002).

[40] S. Abrahamyan et. al, "New Measurements of the Transverse Beam Asymmetry for Elastic Electron Scattering from Selected Nuclei", PRL109, 192501 (2012)

[41] D. Androic et. al, "Measurement of the Beam-Normal Single-Spin Asymmetry for Elastic Electron Scattering from ^{12}C and ^{27}Al", 2021, arXiv:2103.09758 [nucl-ex]

[42] O. Koshchii, M. Gorchtein, X. Roca-Maza, and H. Spiesberger, "Beam-normal single-spin asymmetry in elastic scattering of electrons from a spin-0 nucleus",2021, arXiv:2102.11809 [nucl-th]

[43] C. W. Leemann, D. R. Douglas and G. A. Krafft, "THE CONTINUOUS ELECTRON BEAM ACCELERATOR FACILITY: CEBAF at the Jefferson Laboratory", Annu. Rev. Nucl. Part. Sci., 2001.

[44] Rupesh Silwal, *Probing the Strangeness Content of the Proton and the Neutron Radius of ^{208}Pb using Parity-Violating Electron Scattering*. PhD Thesis, University of Virginia, May 2012.

[45] Kiadtasik Saenboonruang, *Measurement of the Neutron Radius of ^{208}Pb Through Parity Violation in Electron Scattering*, PhD Thesis, University of Virginia, May 2013.

[46] Tao Ye, "Calibrating the Sensitivity of High-Rate Asymmetry Measurements to Beam Motion", DNP 2020 Fall Meeting, November 1, 2020

[47] D.W. Higinbotham and T. Keppel, "2017 Version: Jefferson Lab Hall AStandard Equipment Manual", 2017

[48] C. Jen, /textitFirst Leptonic Probe of Neutron Radii in Lead at Low Q^2, PhD Thesis, Syracuse University, May 2013

[49] J. Alcorn et. al, *Nuclear Instruments and Methods in Physics Research Section A: Accelerators, Spectrometers, Detectors and Associated Equipment* 522, 294, 2004. ISSN 0168-9002

[50] Ye Tian, Private Communication

[51] M. Friend et. al, "Upgraded photon calorimeter with integrating readout for Hall A Compton Polarimeter at Jefferson Lab", arXiv:1108.3116 [physics.ins-det]

[52] J. C. Cornejo, *Compton Scattering Polarimetry for The Determination of the Proton'S Weak Charge Through Measurements of the Parity-Violating Asymmetry of 1H(E,e')P*, PhD Thesis, College of William and Mary, August 2016

[53] Hall A Møller Manual, February 19, 2021, $https : //hallaweb.jlab.org/equipment/moller/OSP/20190219_moller_manual.pdf$

[54] Silviu Covrig Dusa, "The PREX2/CREX Target", February 28, 2020

[55] Silviu Covrig Dusa, "PREX2-CREX Target Design Update", PREX/CREX Collaboration Meeting, March 3, 2017

[56] PREX Collaboration, "PREX/CREX Design Document Version 3.0", $https : //prex.jlab.org/DocDB/0000/000002/003/prex - crex_V3.pdf$, 2017

[57] Cameron Clarke, "High Luminosity Lead-208 Targets for the PREX-2 experiment", DNP 2020 Fall Meeting, October, 28, 2020

[58] Seamus Riordan,"PREX and CREX Collimator Figure of Merit",$https : //prex.jlab.org/DocDB/0002/000293/001/prexcrex_collfom.pdf$, December 14, 2018

[59] K. G. Fissum et. al, textitNuclear Instruments and Methods in Physics Research Section A:Accelerators, Spectrometers, Detectors and Associated Equipment 474, 108, 2001. ISSN 0168-9002

[60] Dustin McNulty, "Main Detectors for PREX-II and CREX", PREX/CREX Collaboration Meeting, July 26, 2018

[61] Dustin McNulty, "HRS Detector Package and Installation", PREX/CREX Collaboration Meeting, February 16, 2019

[62] Dustin McNulty, "Detectors for High Flux Parity Experiments at JLab: PREX-II, CREX and MOLLER", INT Weak Elastic Workshop, March 5, 2019

[63] K. Saenboonruang and N. Liyanage. "Q^2 Measurement and Challenges in PREX", Nat. Sci. 49, 277-287 (2015)

[64] Chandan Ghosh, Private Communication

[65] Cameron Clarke, Private Communication

[66] Karl Brown, "A First- and Second Order Matrix Theory for the Design of Beam Transport Systems and Charged Particle Spectrometers", June 1982

[67] Hanjie Liu, Measurement of the Ratio of the Neutron to Proton Structure Functions, and the Three-Nucleon EMC Effect in Deep Inelastic Electron Scattering Off Tritium and Helium-3 Mirror Nuclei , PhD thesis, Columbia University, 2020

[68] Nilanga Layanage, "Optics Calibration of the Hall A High Resolution Spectrometers using the new optimizer", July 18, 2002

[69] Yi Qiang, *Search for Pentaquark Partners Theta++, Sigma0 and N0 in H(e,e'K(pi))X Reactions at Jefferson Lab Hall A*, PhD Thesis, Massachusetts Institute of Technology, May 2007

[70] D. Adhikari et al., "An Accurate Determination of the Neutron Skin Thickness of ^{208}Pb through Parity-Violation in Electron Scattering", arXiv:2102.10767 [nucl-ex]

[71] Kent Paschke, "Acceptance Function", PREX-2 Analysis Meeting, October 3, 2020

[72] `http://ace.phys.virginia.edu/HAPPEX/4294`

[73] `http://ace.phys.virginia.edu/HAPPEX/4291`

[74] `http://ace.phys.virginia.edu/HAPPEX/3762`

[75] Allison Zec, Private Communication

[76] `http://ace.phys.virginia.edu/HAPPEX/4319`

[77] K. A. Aniol et al., "Parity-violating electroweak asymmetry in ep scattering", Phys. Rev. C 69, 065501 (2004)

[78] R. S. Beminiwattha, *A Measurement of the Weak Charge of the Proton through Parity ViolatingElectron Scattering using the Qweak Apparatus: A 21% Result*, PhD Thesis, Ohio University, August 2013

[79] Bryan Moffit,*Elastic Scattering of Longitudinally Polarized Electrons from ^4He. A measurement of G_E^s at Q^2 = 0.1 $(GeV/c)^2$*, PhD thesis, College of William and Mary, May 2007

[80] https://logbooks.jlab.org/entry/3717393

[81] `https://logbooks.jlab.org/entry/3717389`

[82] `https://logbooks.jlab.org/entry/3721958`

[83] http://ace.phys.virginia.edu/HAPPEX/4157

[84] Chandan Ghosh, "Results from PREX-2", Virtual Hall A Winter Collaboration Meeting, January 21, 2021

[85] http://ace.phys.virginia.edu/HAPPEX/3880

[86] Weibin Zhang, "PREX-II Carbon Contamination", PREX-2 Analysis Meeting, September 30, 2020

[87] Devi Adhikari, "PREX-II Detector Non-LinearityStudies at ISU ", October 1, 2017

[88] Devi Adhikari, "PREX-II Detector Non-Linearity Update", July 7, 2020

[89] http://ace.phys.virginia.edu/HAPPEX/4408

[90] http://ace.phys.virginia.edu/HAPPEX/4409

[91] The CREX Collaboration, "CREX: Parity Violating Measurement of the Weak Charge Distribution of ^{48}Ca to 0.02 fm Accuracy"

[92] Eric King, Private Communication

Appendix A

Transverse Running Integrating Data

A.1 Asymmetries at the Minirun Level

A.1.1 Raw Asymmetries

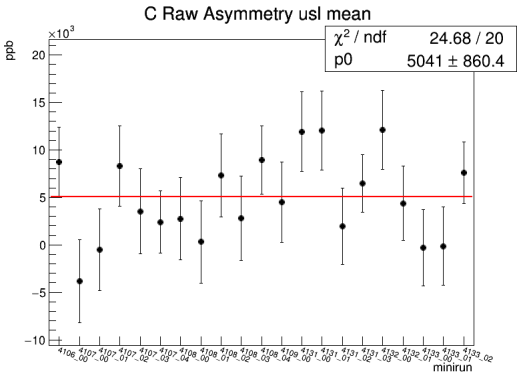

(a) ^{12}C Upstream Left Asymmetry

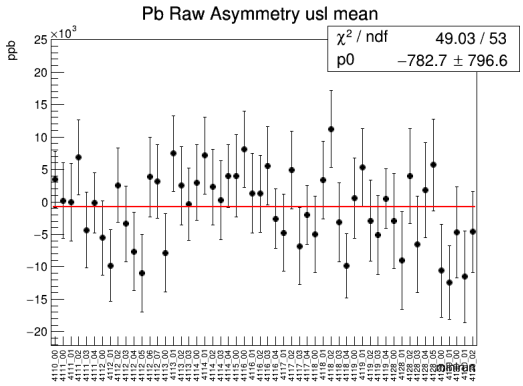

(b) ^{208}Pb Upstream Left Asymmetry

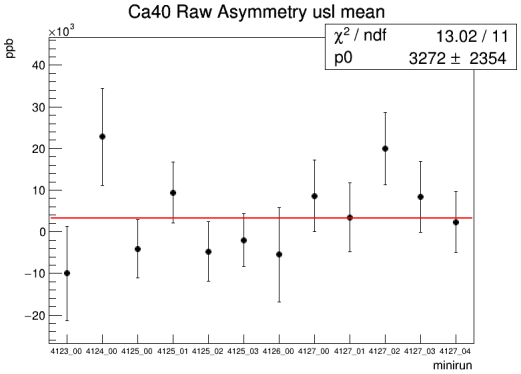

(c) ^{40}Ca Upstream Left Asymmetry

Figure A.1: Raw Asymmetries for upstream left detectors in ppb

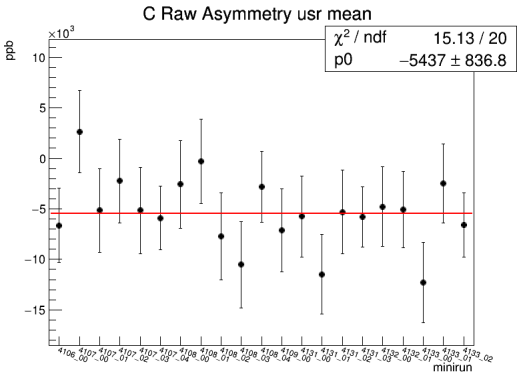

(a) ^{12}C Upstream Right Asymmetry

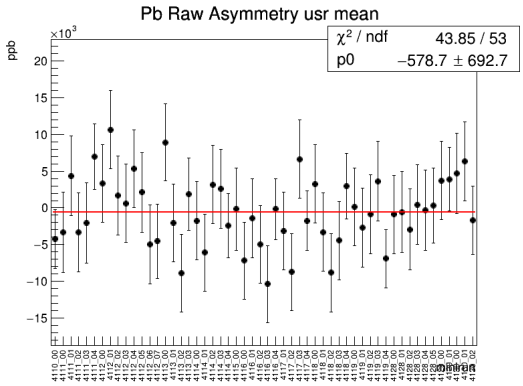

(b) ^{208}Pb Upstream Right Asymmetry

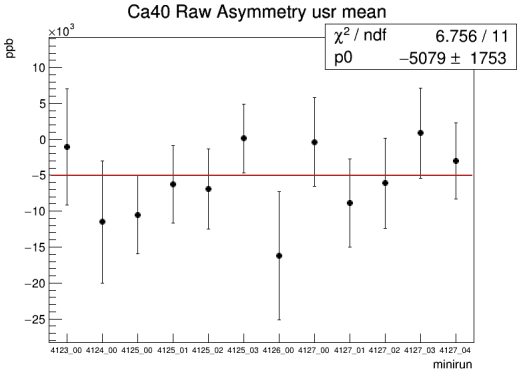

(c) ^{40}Ca Upstream Right Asymmetry

Figure A.2: Raw Asymmetries for upstream right detectors in ppb

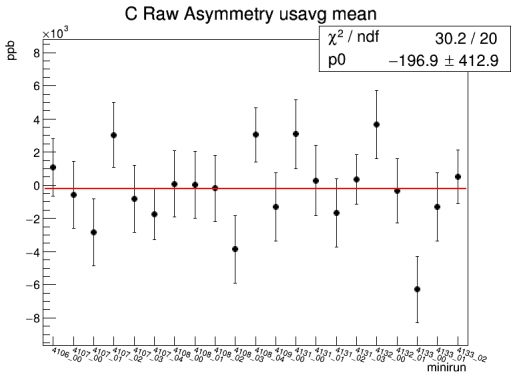

(a) ^{12}C Upstream Average

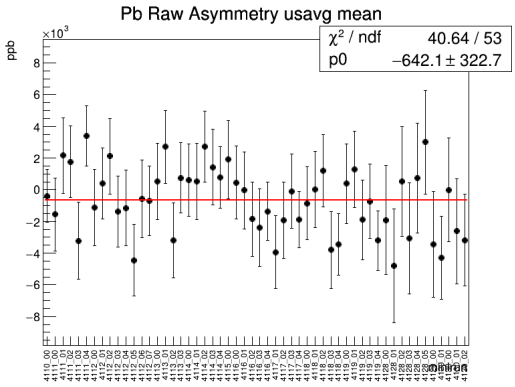

(b) ^{208}Pb Upstream Average

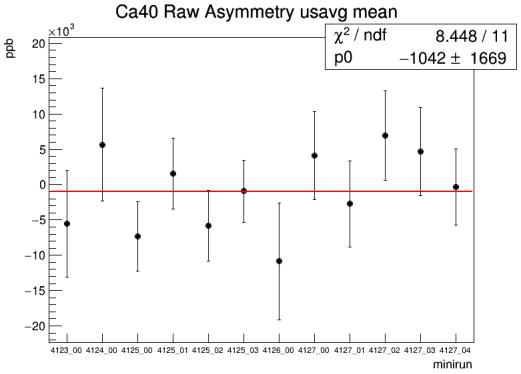

(c) ^{40}Ca Upstream Average

Figure A.3: Raw Upstream Averages in ppb

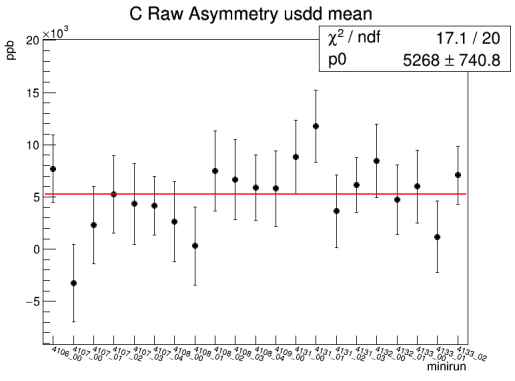

(a) ^{12}C Raw Double Difference

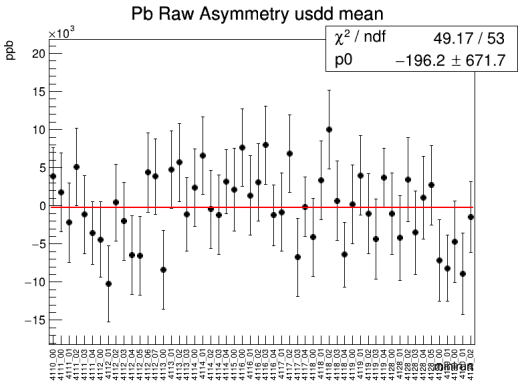

(b) ^{208}Pb Raw Double Difference

Figure A.4: Raw Double Differences for ^{12}C and ^{208}Pb given in ppb

A.1.2 Charge Asymmetry

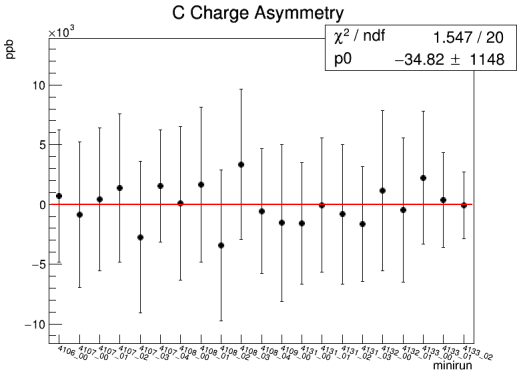

(a) ^{12}C A_I

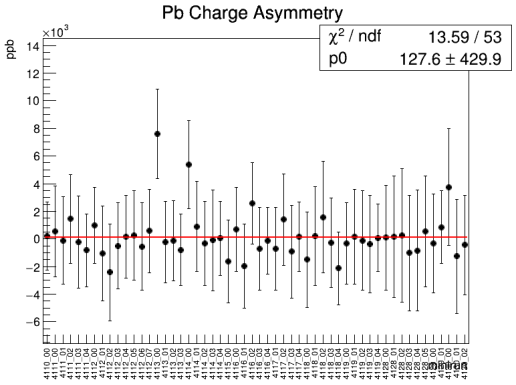

(b) ^{208}Pb A_I

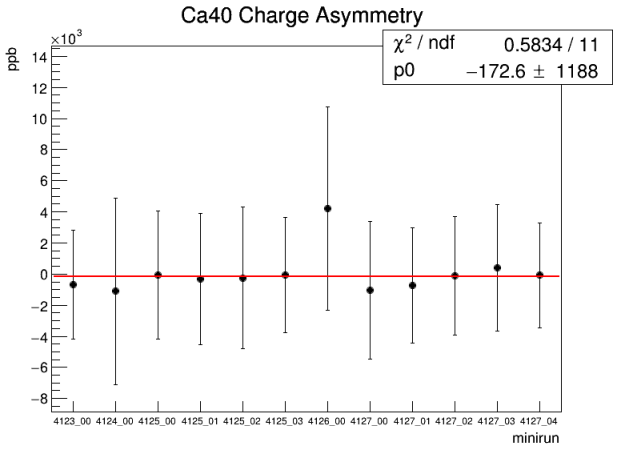

(c) ^{40}Ca A_I

Figure A.5: Sign corrected charge asymmetries in ppb.

A.1.3 Regression Corrected Asymmetries

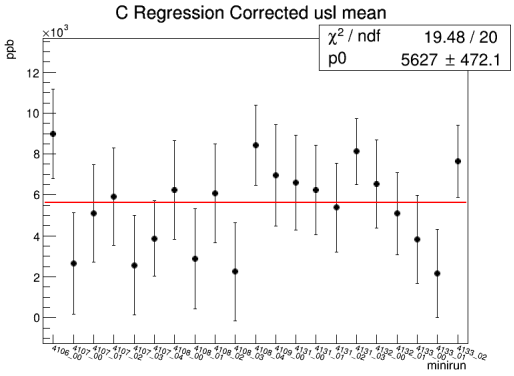

(a) ^{12}C Regression Corrected Upstream Left Asymmetry

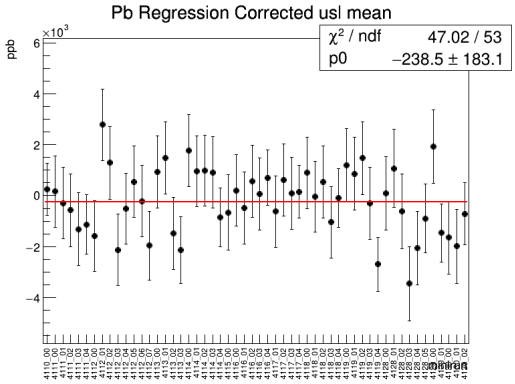

(b) ^{208}Pb Regression Corrected Upstream Left Asymmetry

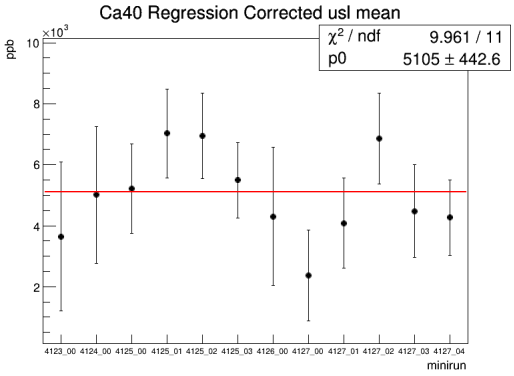

(c) ^{40}Ca Upstream Regression Corrected Left Asymmetry

Figure A.6: Regression Corrected Asymmetries for upstream left detectors in ppb

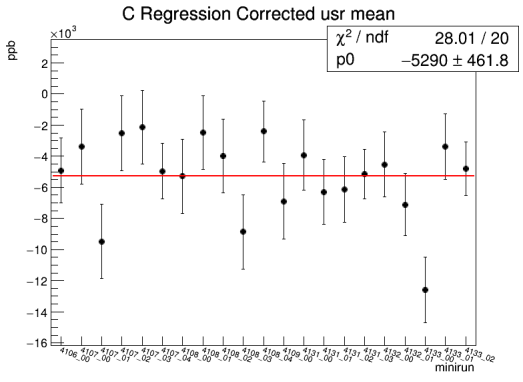

(a) ^{12}C Regression Corrected Upstream Right Asymmetry

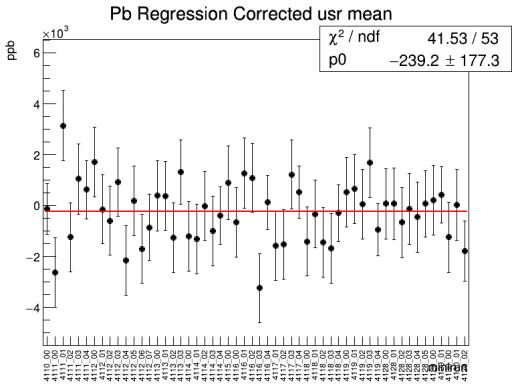

(b) ^{208}Pb Regression Corrected Upstream Right Asymmetry

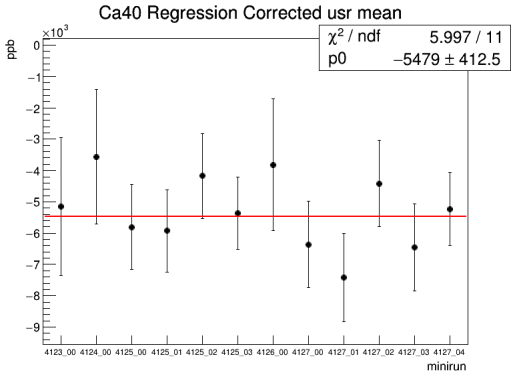

(c) ^{40}Ca Upstream Regression Corrected Right Asymmetry

Figure A.7: Regression Corrected Asymmetries for upstream right detectors in ppb

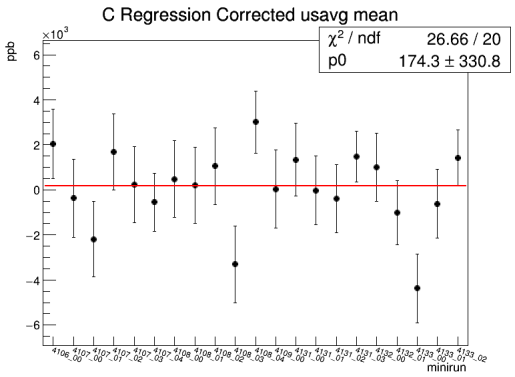

(a) ^{12}C Upstream Average

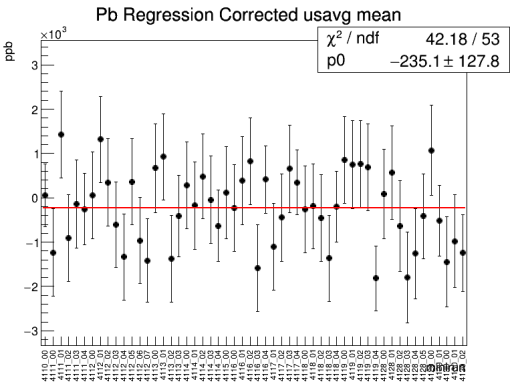

(b) ^{208}Pb Upstream Average

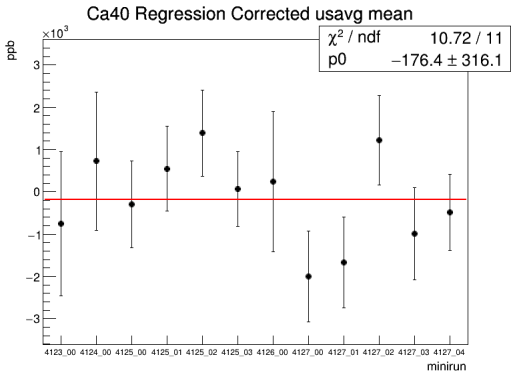

(c) ^{40}Ca Upstream Average

Figure A.8: Regression Corrected Upstream Averages in ppb

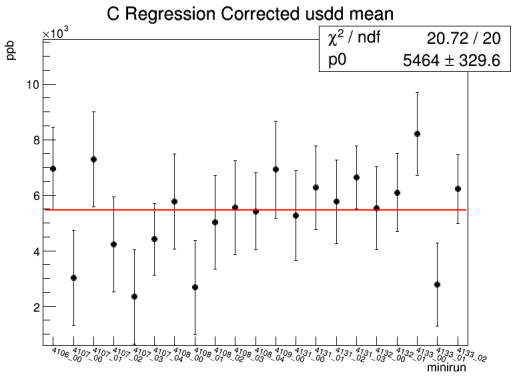

(a) ^{12}C Regression Corrected Upstream Double Difference

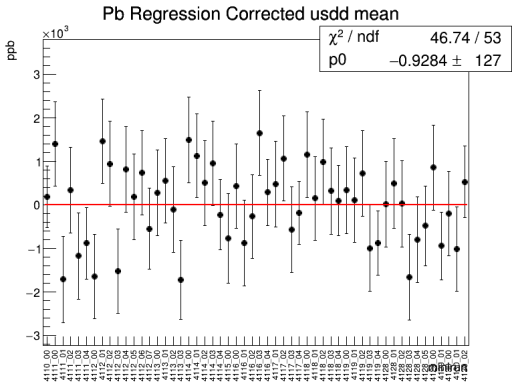

(b) ^{208}Pb Regression Corrected Upstream Double Difference

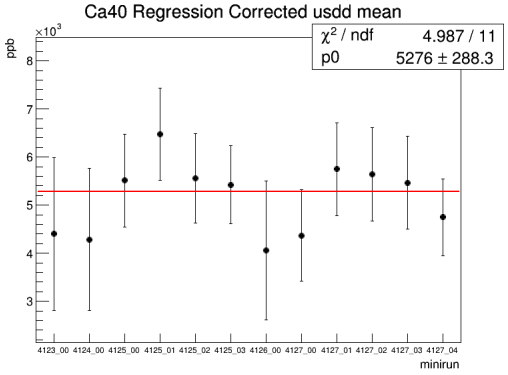

(c) ^{40}Ca Upstream Regression Corrected Double Difference

Figure A.9: Regression Corrected Double Differences in ppb

Dither Corrected Asymmetries

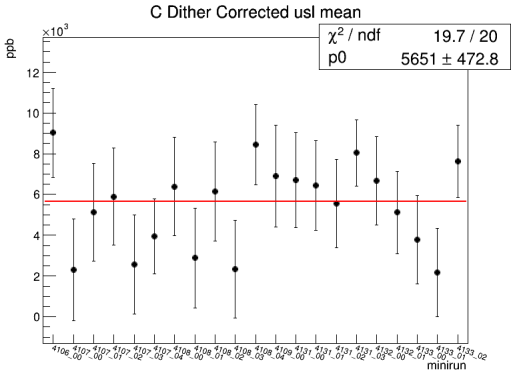

(a) ^{12}C Dither Corrected Upstream Left Asymmetry

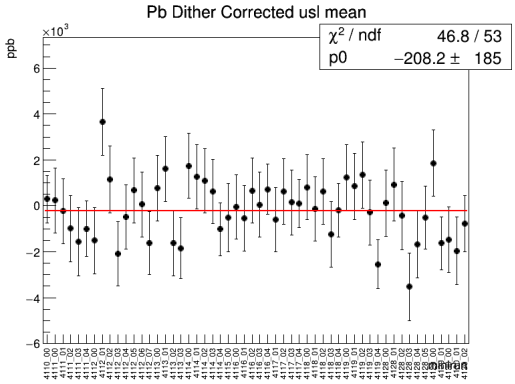

(b) ^{208}Pb Dither Corrected Upstream Left Asymmetry

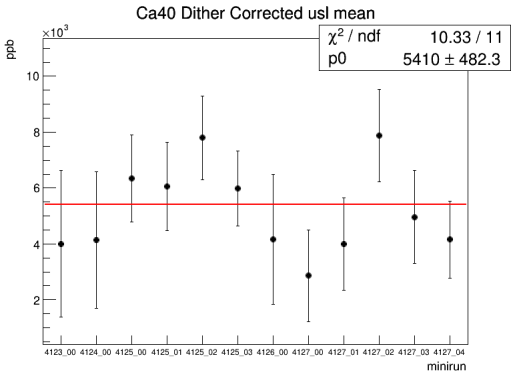

(c) ^{40}Ca Upstream Dither Corrected Left Asymmetry

Figure A.10: Dither Corrected Asymmetries for upstream left detectors in ppb

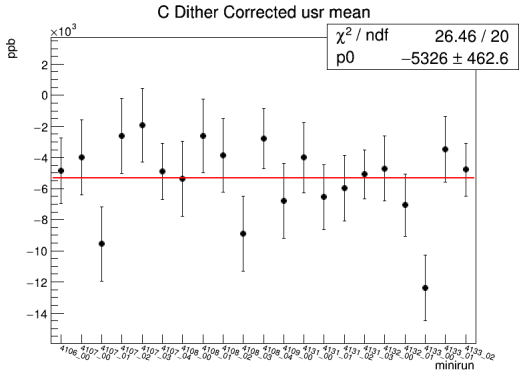

(a) ^{12}C Dither Corrected Upstream Right Asymmetry

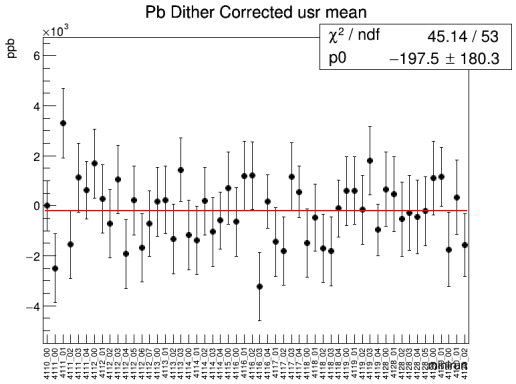

(b) ^{208}Pb Dither Corrected Upstream Right Asymmetry

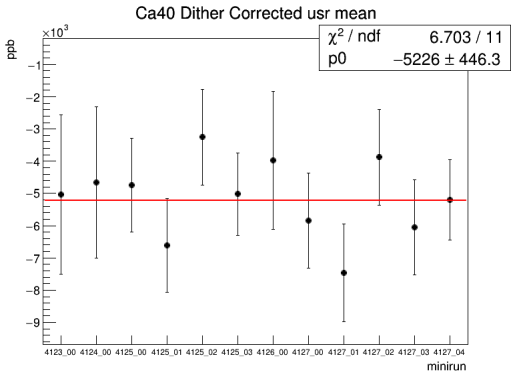

(c) ^{40}Ca Upstream Dither Corrected Right Asymmetry

Figure A.11: Dither Corrected Asymmetries for upstream right detectors in ppb

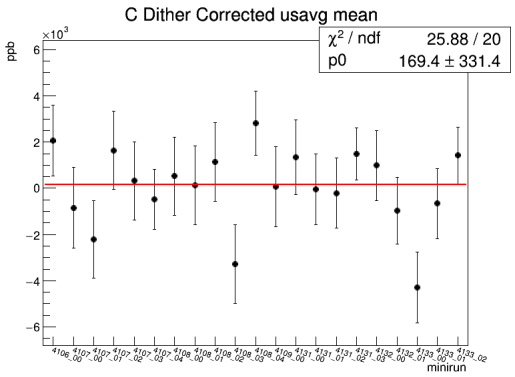

(a) ^{12}C Upstream Average

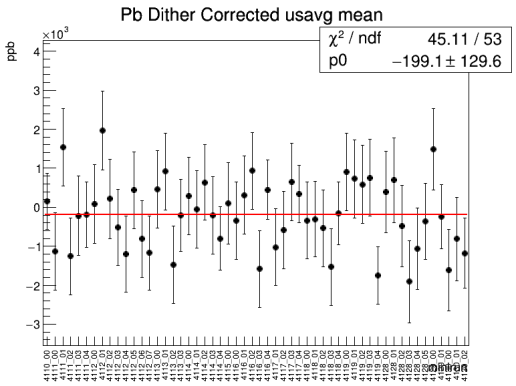

(b) ^{208}Pb Upstream Average

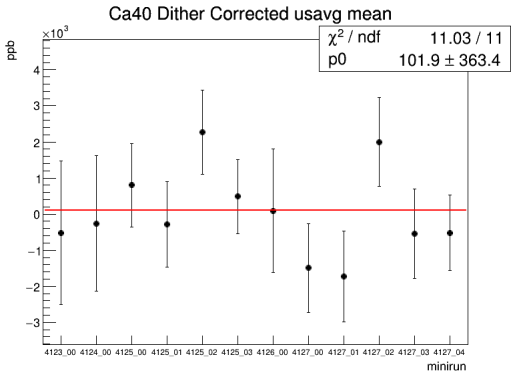

(c) ^{40}Ca Upstream Average

Figure A.12: Dithering Corrected Upstream Averages in ppb

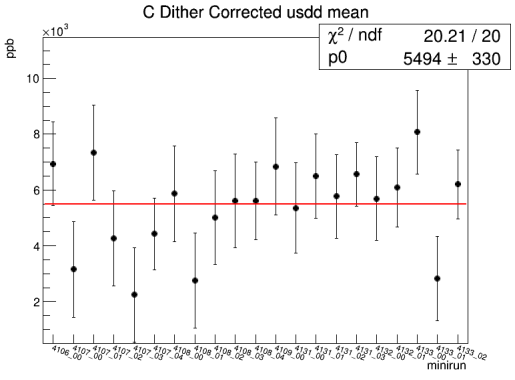

(a) ^{12}C Dither Corrected Upstream Double Difference

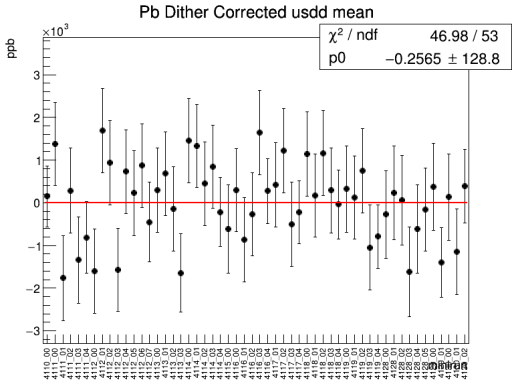

(b) ^{208}Pb Dither Corrected Upstream Double Difference

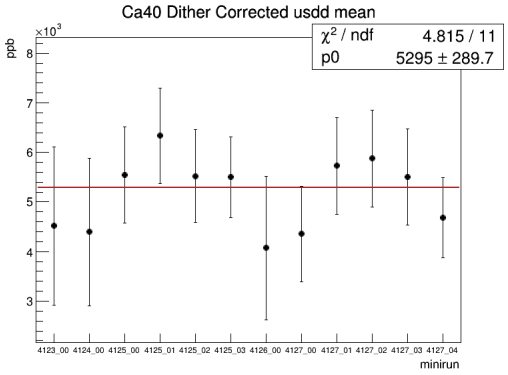

(c) ^{40}Ca Upstream Dither Corrected Double Difference

Figure A.13: Dither Corrected Double Differences in ppb

A.2 Multiplet Level Asymmetries

A.2.1 ^{40}Ca Asymmetry Distributions

A.2.1.1 ^{40}Ca Raw Asymmetries

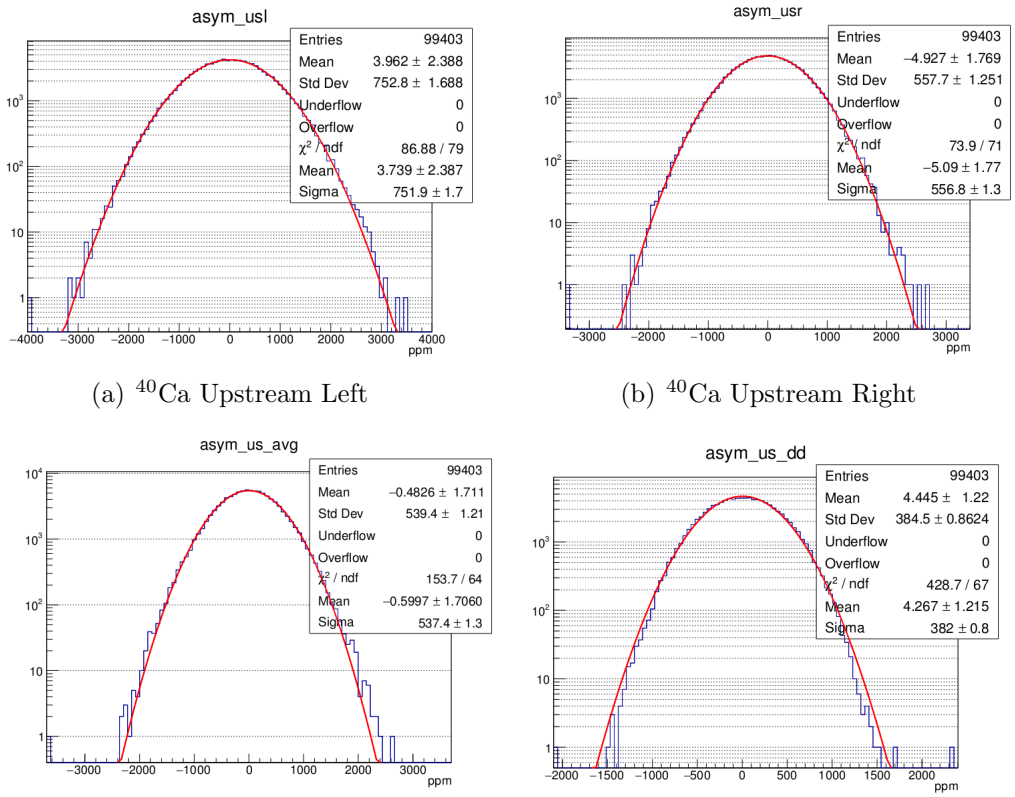

(a) ^{40}Ca Upstream Left

(b) ^{40}Ca Upstream Right

(c) ^{40}Ca Upstream Average

(d) ^{40}Ca Upstream Double Difference

Figure A.14: ^{40}Ca Raw Octet Level Asymmetries in ppm

A.2.1.2 ^{40}Ca Regression Corrected Asymmetries

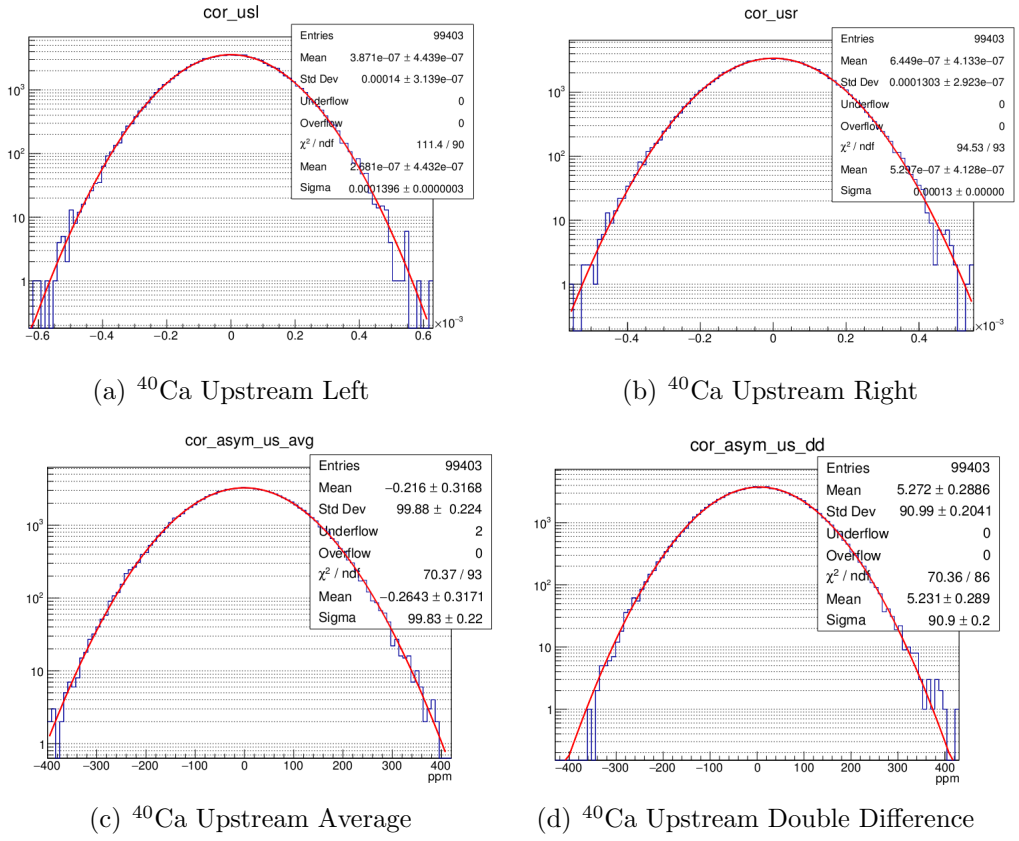

(a) ^{40}Ca Upstream Left

(b) ^{40}Ca Upstream Right

(c) ^{40}Ca Upstream Average

(d) ^{40}Ca Upstream Double Difference

Figure A.15: ^{40}Ca Regression Corrected Octet Level Asymmetries in ppm

A.2.1.3 ^{40}Ca Dithering Corrected Asymmetries

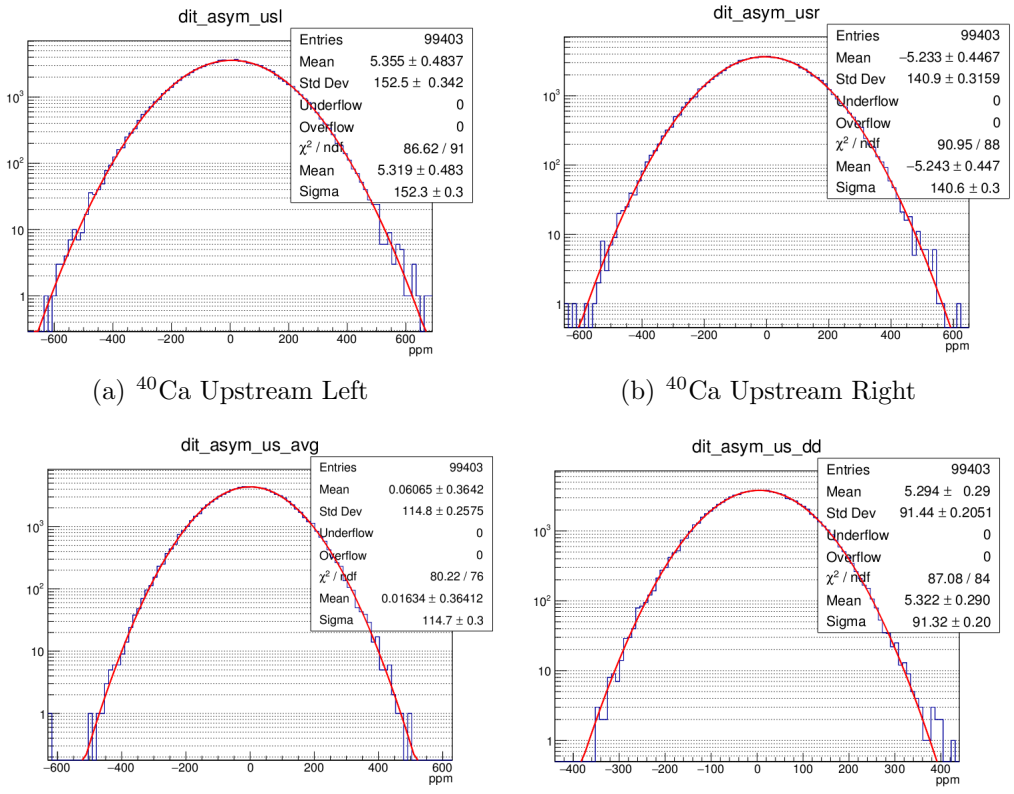

(a) ^{40}Ca Upstream Left

(b) ^{40}Ca Upstream Right

(c) ^{40}Ca Upstream Average

(d) ^{40}Ca Upstream Double Difference

Figure A.16: ^{40}Ca Dithering Corrected Octet Level Asymmetries in ppm

A.2.2 ^{12}C Asymmetry Distributions

A.2.2.1 ^{12}C Raw Asymmetries

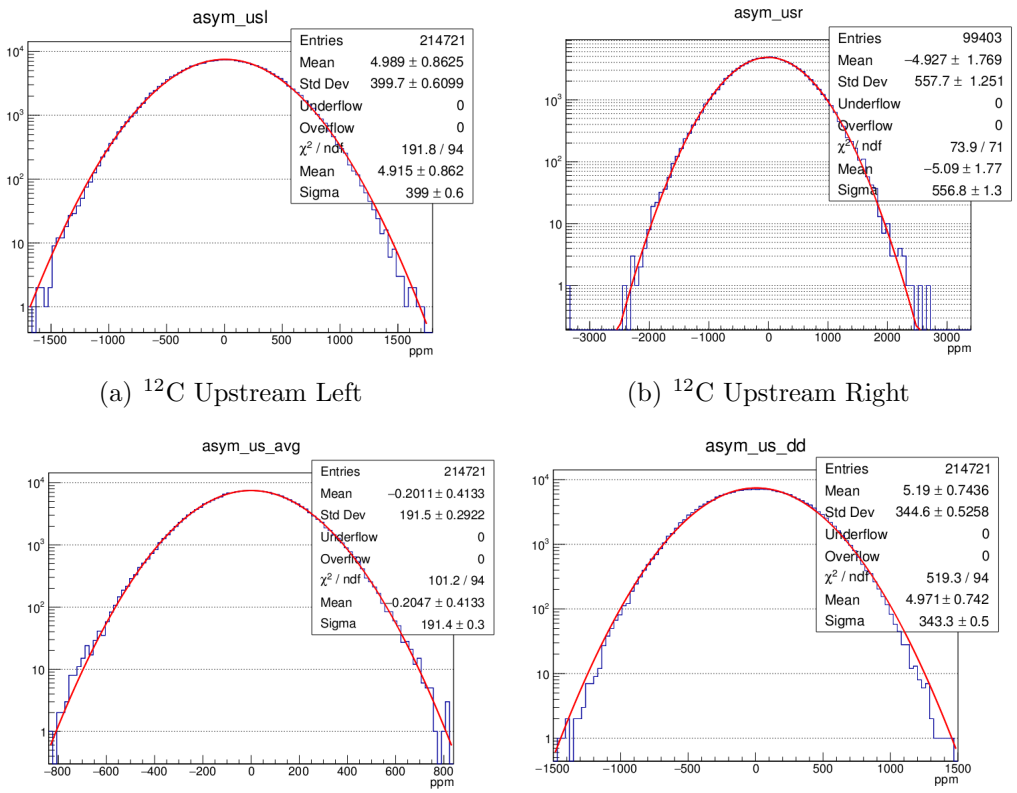

(a) ^{12}C Upstream Left

(b) ^{12}C Upstream Right

(c) ^{12}C Upstream Average

(d) ^{12}C Upstream Double Difference

Figure A.17: ^{12}C Raw Octet Level Asymmetries in ppm

A.2.2.2 ^{12}C Regression Corrected Asymmetries

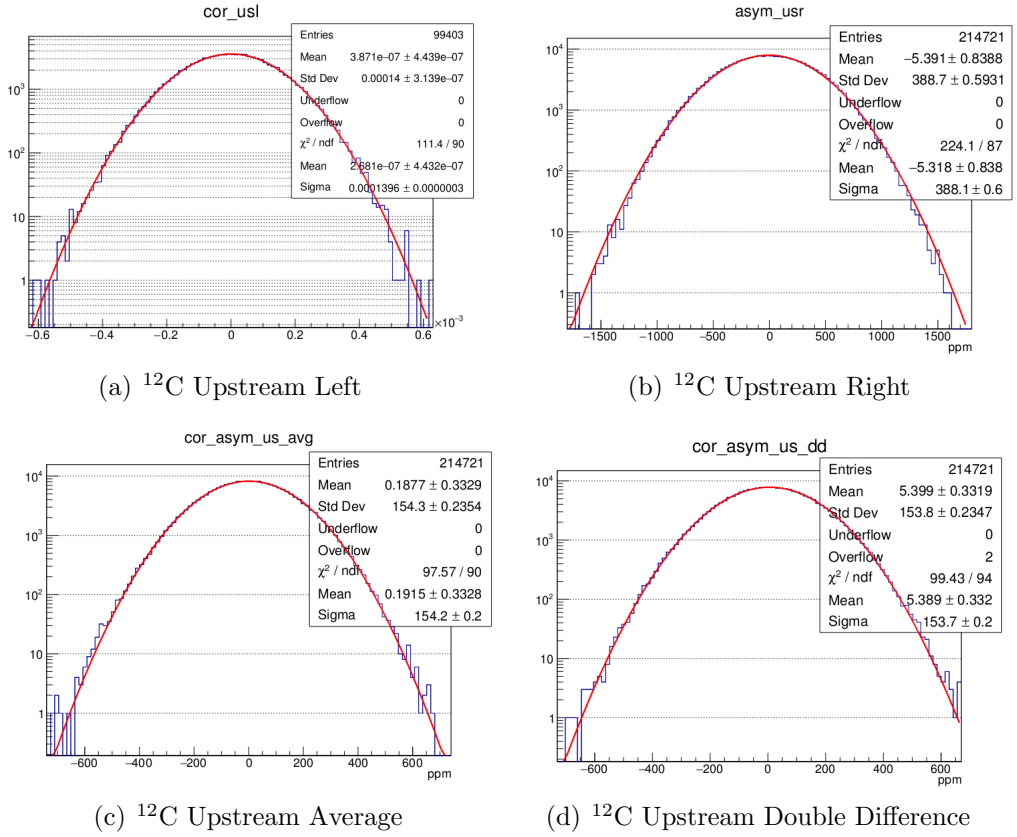

(a) ^{12}C Upstream Left

(b) ^{12}C Upstream Right

(c) ^{12}C Upstream Average

(d) ^{12}C Upstream Double Difference

Figure A.18: ^{12}C Regression Corrected Octet Level Asymmetries in ppm

A.2.2.3 ^{12}C Dithering Corrected Asymmetries

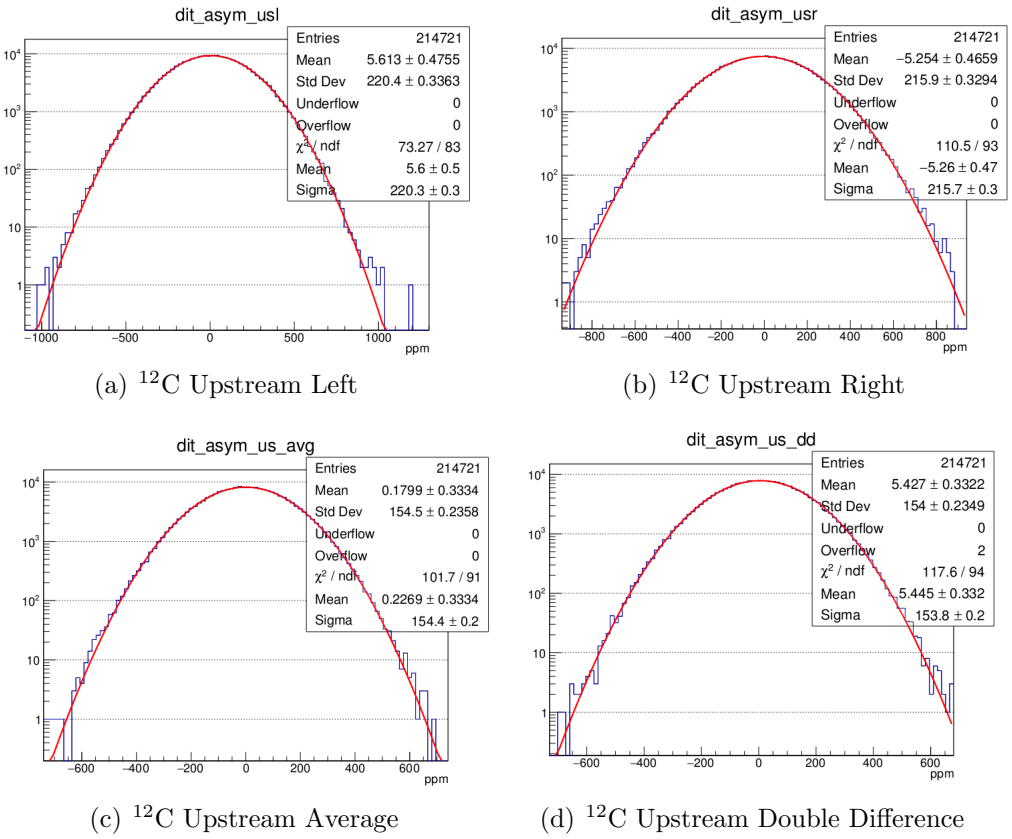

(a) ^{12}C Upstream Left

(b) ^{12}C Upstream Right

(c) ^{12}C Upstream Average

(d) ^{12}C Upstream Double Difference

Figure A.19: ^{12}C Dithering Corrected Octet Level Asymmetries in ppm

A.2.3 ^{208}Pb Asymmetry Distributions

A.2.3.1 ^{208}Pb Raw Asymmetries

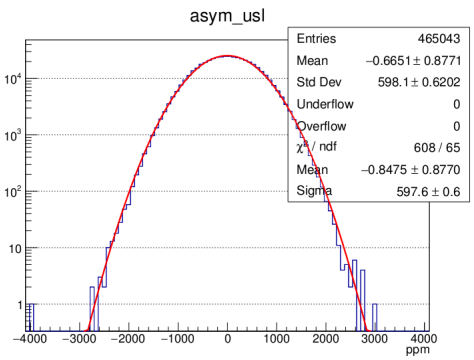

(a) ^{208}Pb Upstream Left

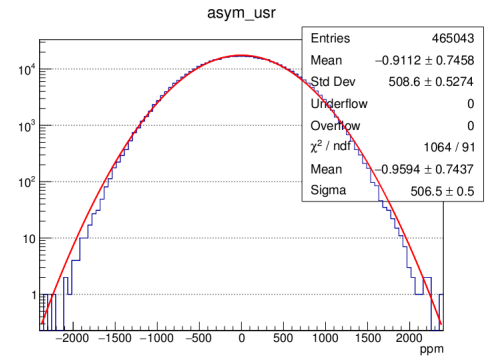

(b) ^{208}Pb Upstream Right

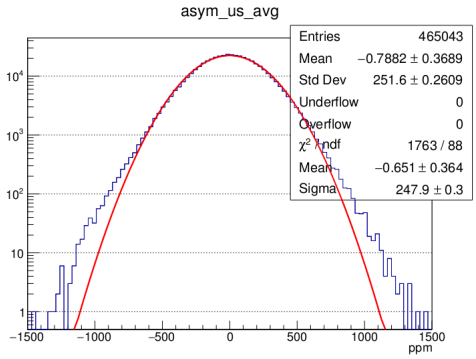

(c) ^{208}Pb Upstream Average

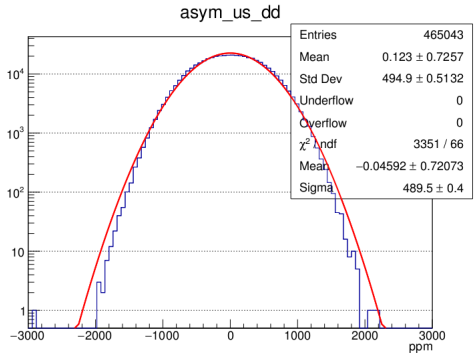

(d) ^{208}Pb Upstream Double Difference

Figure A.20: ^{208}Pb Raw Octet Level Asymmetries in ppm

A.2.3.2 ^{208}Pb Regression Corrected Asymmetries

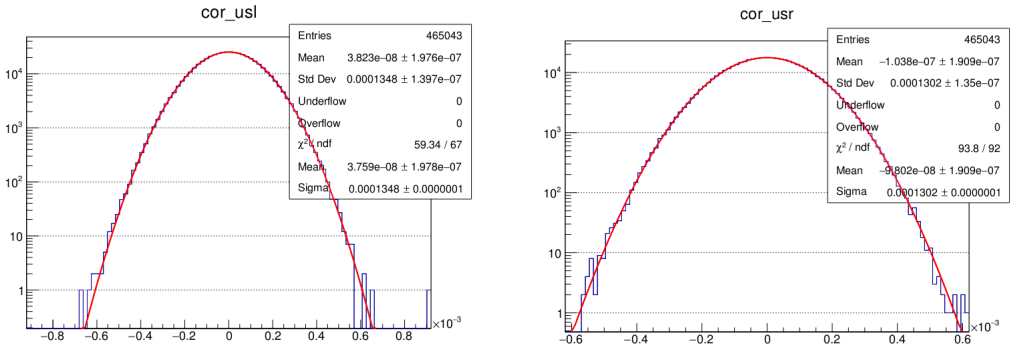

(a) ^{208}Pb Upstream Left

(b) ^{208}Pb Upstream Right

sectsiocnts/Apps/AnalysisFigures/Regression/Pb208_208a_vs_dd.png

(c) ^{208}Pb Upstream Average

(d) ^{208}Pb Upstream Double Difference

Figure A.21: ^{208}Pb Regression Corrected Octet Level Asymmetries in ppm

A.2.3.3 ^{208}Pb Dithering Corrected Asymmetries

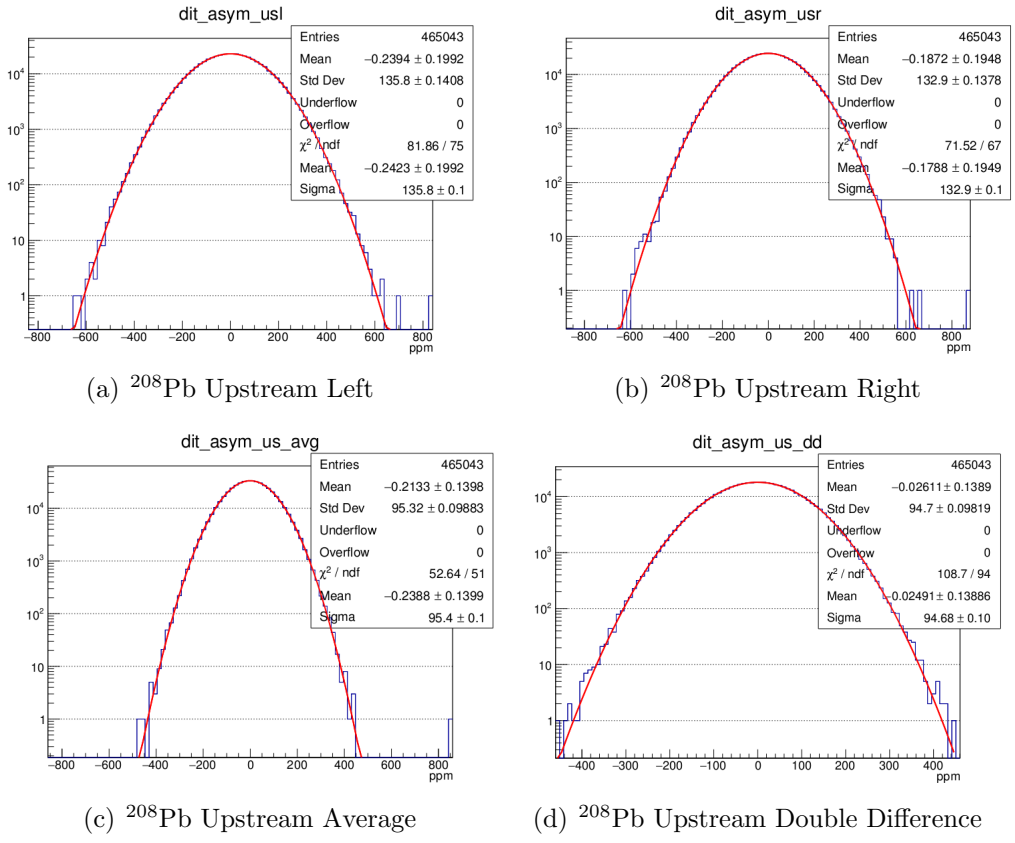

(a) ^{208}Pb Upstream Left

(b) ^{208}Pb Upstream Right

(c) ^{208}Pb Upstream Average

(d) ^{208}Pb Upstream Double Difference

Figure A.22: ^{208}Pb Dithering Corrected Octet Level Asymmetries in ppm

Appendix B

Kinematic Distributions

B.1 $\langle \cos\phi \rangle$ Distributions

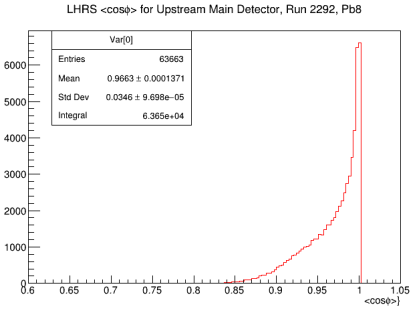

(a) LHRS ^{208}Pb $\langle \cos\phi \rangle$, Target 8

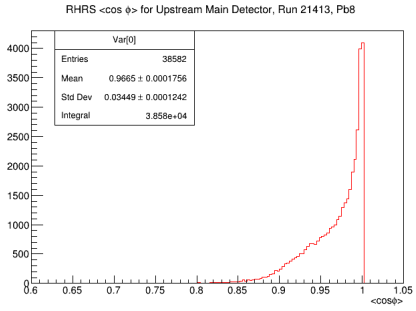

(b) RHRS ^{208}Pb $\langle \cos\phi \rangle$, Target 8

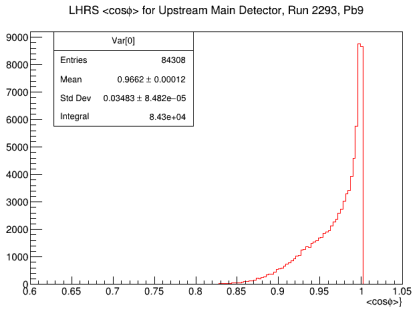

(c) LHRS ^{208}Pb $\langle \cos\phi \rangle$, Target 9

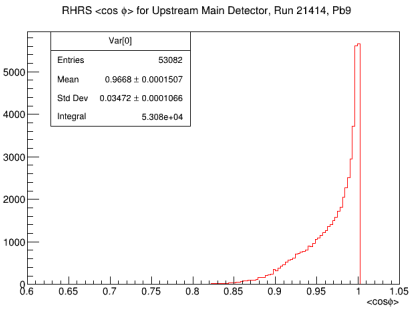

(d) RHRS ^{208}Pb $\langle \cos\phi \rangle$, Target 9

Figure B.1: ^{208}Pb $\langle \cos\phi \rangle$ Distributions. The A_T data was taken on two targets denoted as Pb8 and Pb9

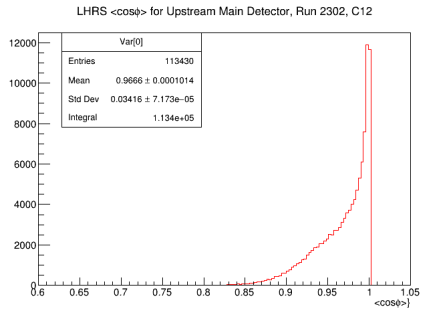

(a) LHRS ^{12}C $\langle \cos\phi \rangle$

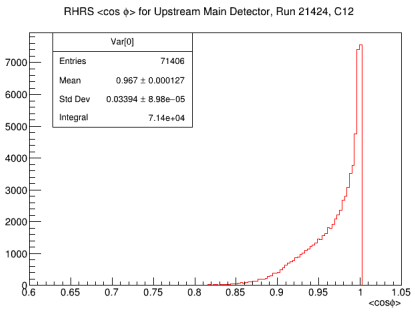

(b) RHRS ^{12}C $\langle \cos\phi \rangle$

Figure B.2: ^{12}C $\langle \cos\phi \rangle$ Distributions

B.2 Q^2 Distributions

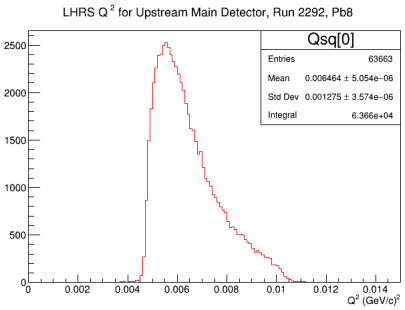

(a) LHRS ^{208}Pb Q^2, Target 8

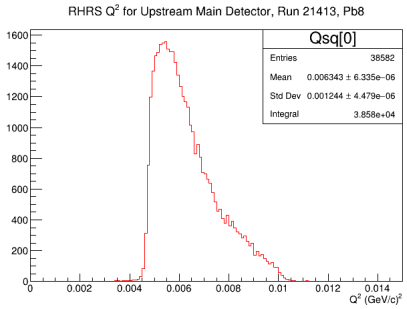

(b) RHRS ^{208}Pb Q^2, Target 8

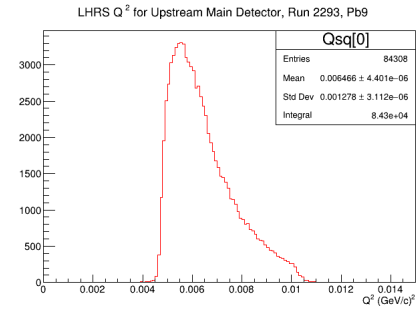

(c) LHRS ^{208}Pb Q^2, Target 9

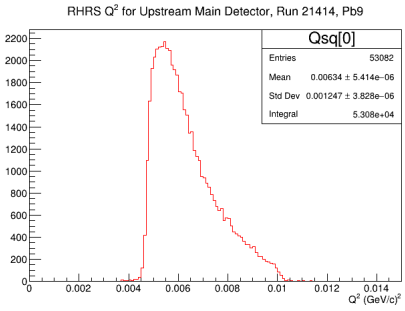

(d) RHRS ^{208}Pb Q^2, Target 9

Figure B.3: ^{208}Pb Q^2 Distributions

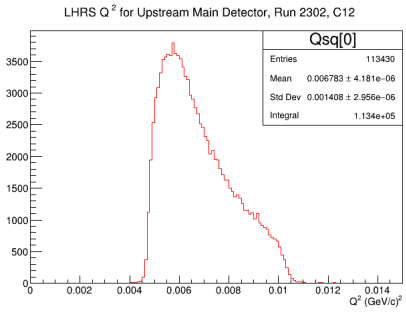

(a) LHRS ^{12}C Q^2

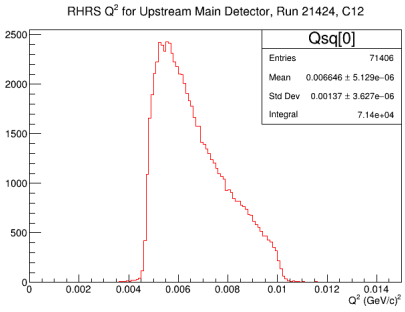

(b) RHRS ^{12}C Q^2

Figure B.4: ^{12}C Q^2 Distributions